KEK Proceedings 94-8
November 1994
R/D

Proceedings of the Fourth EGS4 Users' Meeting in Japan

July 25 - 27, 1994.

KEK, Tsukuba, Japan

Edited by

H. Hirayama, Y. Namito and S. Ban

NATIONAL LABORATORY FOR
HIGH ENERGY PHYSICS

National Laboratory for High Energy Physics, 1994

KEK Reports are available from:

Technical Information & Library
National Laboratory for High Energy Physics
1-1 Oho, Tsukuba-shi
Ibaraki-ken, 305
JAPAN

Phone: 0298-64-1171
Telex: 3652-534 (Domestic)
(0)3652-534 (International)
Fax: 0298-64-4604
Cable: KEK OHO
E-mail: LIBRARY@JPNKEKVX (Bitnet Address)
library@kekvax.kek.jp (Internet Address)

FOREWARD

The Fourth EGS4 Users' Meeting in Japan was held at the National Laboratory for High Energy Physics (KEK) from July 25 to 27. The meeting has been hosted by the Radiation Safety Control Center, KEK. Above 80 participants attended the meeting.

The meeting was divided into two parts. Lectures concerning the EGS4 System, Mortran, User code, HOWFAR, random number generator used in the EGS4 System and the EGS4 shower display system on PC were given at the first half. Practices to install the EGS4 system on the UNIX workstation and to run PEGS4 or user code were also performed. In the later half, 12 talks related EGS4 were presented. The talks covered the wide fields, like the medical application and the calculation of various detector response etc. These talks were very useful to exchange the information between the researchers in the different fields.

Finally, we would like to express our great appreciation to all authors who have prepared manuscript quickly for the publication of this proceedings.

Hideo Hirayama
Yoshihito Namito
Syuichi Ban
Radiation Safety Control Center
KEK, National Laboratory for High Energy Physics

CONTENTS

CALCULATION OF EFFECTIVE DOSE FOR HIGH ENERGY PHOTONS WITH AN ANTHROPOMORPHIC PHANTOM

O. SATO[1], S. IWAI[2], S. TANAKA[3], T. UEHARA[2],
Y. SAKAMOTO[3], and N. YOSHIZAWA[1]

[1] *Mitsubishi Research Institute Inc., 1-8-1 Simo-Meguro, Meguro-ku, Tokyo135,Japan*
[2] *Mitsubishi Atomic Power Industries Inc., 1-297 Kitabukuro-cho, Omiya 330,Japan*
[3] *Japan Atomic Energy Research Institute, Tokai,Naka-gun, Ibaraki 319-11,Japan*

Abstract

The effective doses was calculated for photons from 1MeV to 10GeV by using EGS4 code with an anthropomorphic phantom of MIRD-5 type. The dose equivalent distributions were also calculated in an ICRU sphere and a semi-infinite slab phantom, and were compared to the effective doses. The effective doses are relatively well agreed with the dose equivalents at the depth of 10cm in a semi-infinite slab phantom when the anthropomorphic phantom is irradiated from its back.

1. Introduction

ICRP publication 51[1] tabulated the values of effective dose equivalents for photons upto 10MeV, which were calculated with an anthropomorphic phantom in various irradiation geometries. It is also shown that the ambient dose equivalents at 0.07mm, 3mm, and 10mm depth on the principal axis of ICRU sphere[2]. These effective dose equivalents or ambient dose equivalents were calculated with an approximation neglecting the transports of secondary electrons[3,4], namely, kerma approximation. In this approximation, the secondary electrons immediately deposit their whole kinetic energy, or the charge equilibrium is assumed at everywhere. However, the range of secondary electrons becomes significantly longer than the sizes of organs for high energy photons, thus, the consideration of secondary electron transport will be required for the calculations of effective dose equivalents. For radiation protection and shielding in high energy accelerators and space activities, the fluence to effective dose (defined in ICRP publication 60[5]) conversion coefficients for high energy radiations is the most important and basic data. For these purposes, we calculated the effective doses for the photons upto 10GeV considering secondary electron transport by using EGS4 code[6]. We also calculated the dose equivalent distributions on principal axis of ICRU sphere or in a semi-infinite slab phantom and

compared them to effective doses to investigate the operational quantities for high energy photons.

2. The Anthropmorphic Phantom Geometry and the Calculation of Effective Dose

In Fig.1 is shown the internal structure of anthropomorphic phantom. This phantom was modified for Yamaguchi's data[7] taking into account the Cristy phantom[8] of MIRD-5[9] type as the followings:

A. An oesophagas model was added to the phantom using the mathematical form reported by Lewis et al [10].

B. Stomach location was changed according to the report by Lewis et al.

C. The height of the breast model was changed to about half of the Christy phantom model for making it a hermaphroditic phantom.

Internal organs were considered to be homogeneous in composition and density, while, different densities cited from the MIRD-5 report were assigned for lungs, skeleton and soft tissue, and the composition was represented by 17 elements.

The MARS [6] geometry package developed at ORNL was used to represent an anthropomorphic phantom for the calculation of effective doses with EGS4. MARS (Multiple Array System) is an enhanced geometry package based on CG (Combinatorial Geometry) used in computer codes for radiation shielding, such as MORSE-CG or QAD-CG code.

Two irradiation geometries were compared; the AP (Anterior-Posterior) and the PA (Posterior-Anterior) described in ICRP publication 51. The effective dose equivalents at other irradiation geometries (LAT, ISO, ROT) were also shown in ICRP publication 51, however, the AP or the PA geometry caused higher dose than other geometries.

The incident photon energies were 1, 3, 5, 10, 15, 20, 50, 100, 500MeV, and 1, 10GeV for the calculations of effective doses and dose equivalent distributions. The cutoff energy was set to 100 keV for photons and set to 500keV as kinetic energies of electrons and positrons at which the range of electrons is about 0.2cm. Alternative calculations were performed to compare the results with kerma approximations setting the cutoff energy higher than incident energy.

The calculated effective doses considering and neglecting (equivalent to kerma approximation) electron transports are compared in Fig.2. The significant differences are found at 10MeV, and the effective dose with kerma approximation is two-handled times as higher as the result considering electron transports. The effective doses in the AP geometry is always higher than in the PA geometry when electron transports were neglected, while

the PA geometry shows the higher effective dose above 10MeV when electron transports were considered. In the PA geometry at higher energy, the secondary electrons generated at irradiated side (back of phantom) transports to opposite side, and deposit their energy in the organs at from side of phantom such as testes or breasts.

3. Dose Equivalent Distribution in an ICRU Sphere and a Semi-infinite Slab Phantom

The depth-dose curves on the axis of ICRU sphere and in the semi-infinite slab of ICRU four-element tissue were calculated with the models shown in Fig.3 and Fig.4 to investigate what quantity is suitable as the operational quantity for high energy photons. For ICRU sphere, the dose equivalents on its principle axis were calculated as the deposited energies in 0.4cm- radius small spheres placed on the principle axis. For slab phantom, the pencil photon beam was used to simulate broad parallel beam incident perpendicular to the surface of phantom, and dose equivalents were calculated as the energy depositions in semi-infinite layers of 0.01cm to 0.3cm depth.

Because the number of electrons coming into the small regions (0.4-cm radius) around the principal axis is very small, a lot of computing time is required to calculate the absorbed dose distribution with well statistical accuracy. So, the following variance reduction techniques are applied for the efficient calculations.

(1) Source biasing : The photons incident at the points far from principal axis products smaller number of electrons which reach the region around principal axis. So the source biasing was applied for the radial distribution around a principal axis as the number of entering photons are in inverse proportion to the fifth power of the radii of entering points.

(2) Splitting : In the calculation with source biasing, photons entering near the axis have the greater weights than the photons entering near the axis. These "heavy weight" particles are splitted to a number of "light weight" particles conserving their weights if these particles go toward the region around axis.

(3) Energy cut off of electrons : When the residual range of electrons become smaller than its distance to the region around the axis, these electrons are discarded immediately.

In ICRP publication 51[1], the 1cm depth doses are calculated with kerma approximation assuming the charge equilibrium in the ICRU sphere and the surrounding air. For high energy photons, the thickness of air for charge equilibrium will be very thick, so the air was neglected in this calculation.

4. Comparison of Effective Dose and Dose Equivalents in ICRU Sphere or Semi-Infinite Slab Phantom

Fig.5 shows the comparisons of (a) the dose equivalents at 1-cm depth on the principal axis of ICRU sphere (1cm depth dose equivalent), (b) the maximum dose equivalents on the principal axis of ICRU sphere, (c) the dose equivalents at 1-cm, 10-cm and 20-cm depth in a slab, (d) the maximum dose equivalents in a slab, and (e) effective doses calculated with a mathematical human body phantom in PA or AP geometry at the photon energies from 1MeV to 10GeV. Above 3MeV, the 1cm depth dose equivalents are lower than the effective doses.

The maximum dose equivalents are significantly higher than effective doses above 10MeV, and at 10GeV, they are five to nine times as higher as effective doses. The dose equivalents at 10cm depth in a slab are slight higher than the effective doses calculated in a PA geometry. The difference between 10cm depth dose equivalents and effective doses are about 610GeV.

5. Conclusion

The effective dose for high energy photons are calculated with an anthropomorphic phantom considering secondary electron transports by using EGS4 code. The ambient dose equivalent in a ICRU sphere and a semi-infinite slab phantom are also calculated using EGS4 code. By the comparison of these results, we reach the following two conclusions.

(1) For high energy photons above 10MeV, the formerly used kerma approximations shows the significantly overestimation compared to the calculated effective doses considering secondary electron transports.

(2) The dose equivalents at more deep position than 1-cm depth of a slab phantom can be used as the operational quantity for the effective dose of high energy photons.

References

[1] ICRP, *Data for Use in Protection against External Radiation* , ICRP publication 51, Annals of ICRP **17** No.2-3, Pergamon Press, Oxford (1987).

[2] G. Williams, W. P. Swanson, P. Kragh and G. Dlexler, *Calculation and Analysis of Photon Dose Equivalent Distributions in the ICRU Sphere*, GSF Bericht S-958 (1983).

[3] R.Kramer, M.Zankel, G.Williams and G.Drexler, *The Calculation of Dose from Photon Exposures using Reference Human Phantoms and Monte-Carlo Methods*, GSF Bericht S-885 (1982).

[4] G.Drexler, W.Panzer, L.Widenmann, G.Williams and M.Zankl, *The Calculation od Dose from External Photon Exposures Using Reference Human Phantoms and Monte Carlo Methods Part III: Organ Doses in X-Ray Diagnostis*, GSF-Bericht S-1026 (1984).

[5] ICRP, *1990 Recommendations of the International Commission on Radiological Protection.* ICRP publication 60, Annals of the ICRP21(1-3), Pergamon Press, Oxford (1991).

[6] M.Cristy and K.F.Eckerman, *Specific Absorbed Fractions of Energy at Various Ages from Internal Photon Sources*, ORNL/TM-8381/V1-V7 (1987).

[7] Y.Yamaguchi, *DEEP Code to Calculate Dose Equivalents in Human Phantom for External Photon Exposure by Monte Carlo*, JAERI-M 90-235(1990).

[8] W.S.Snyder, M.R.Ford,and G.G.Warner, *Estimates of specific absorbed fractions for photon sources uniformly distributed in various organs of heterogeneous phantom*, NM/MIRD Pamphlet No.5(revised) J.Nucl. Med. **19** Supplement:5-67 (1987).

[9] C.A.Lewis and R.E.Ellis, *Additions to the Snyder Mathematical Phantom*, Phys. Med. Biol. **24** No.5, 1019-1024 (1979).

[10] J.T.West and M.B.Emmett, *MARS: A Multiple Array System Using Combinatorial Geometry*, NUREG/CR-0200, vol.3, sec.M9, ORNL/NUREG/CSD-2/V3/R2 (1984).

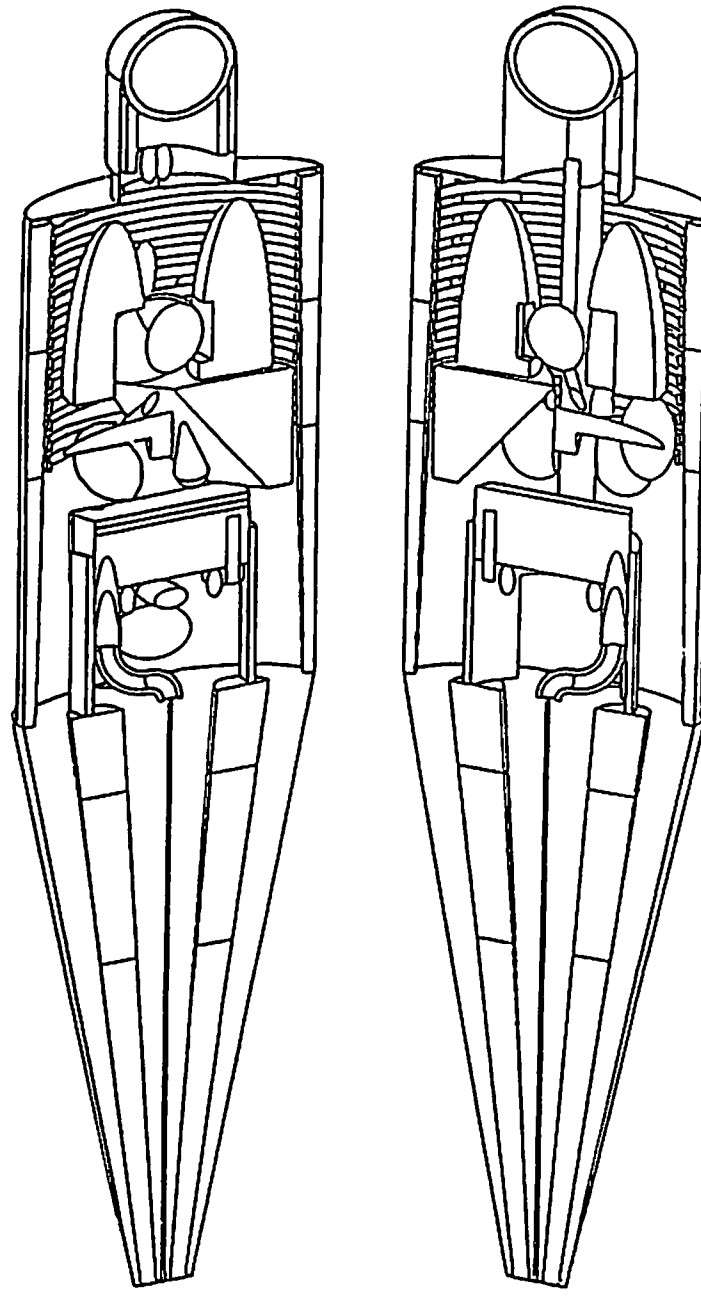

Fig. 1 Internal structure of the anthropomorphic phantom

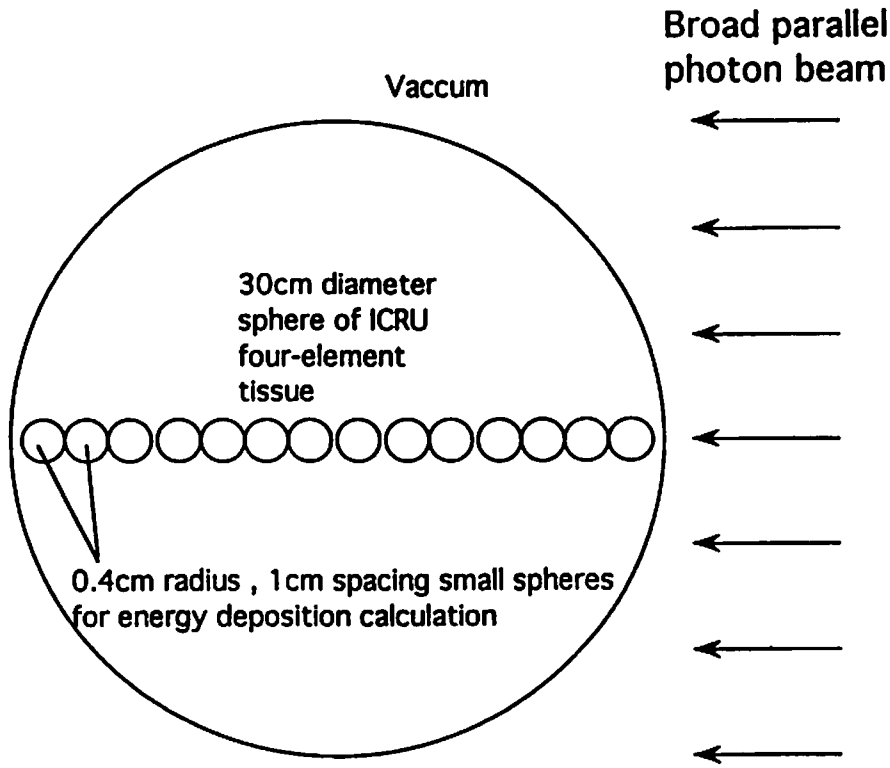

Fig. 2 Model for calculation of dose equivalents on the principal axis of ICRU sphere

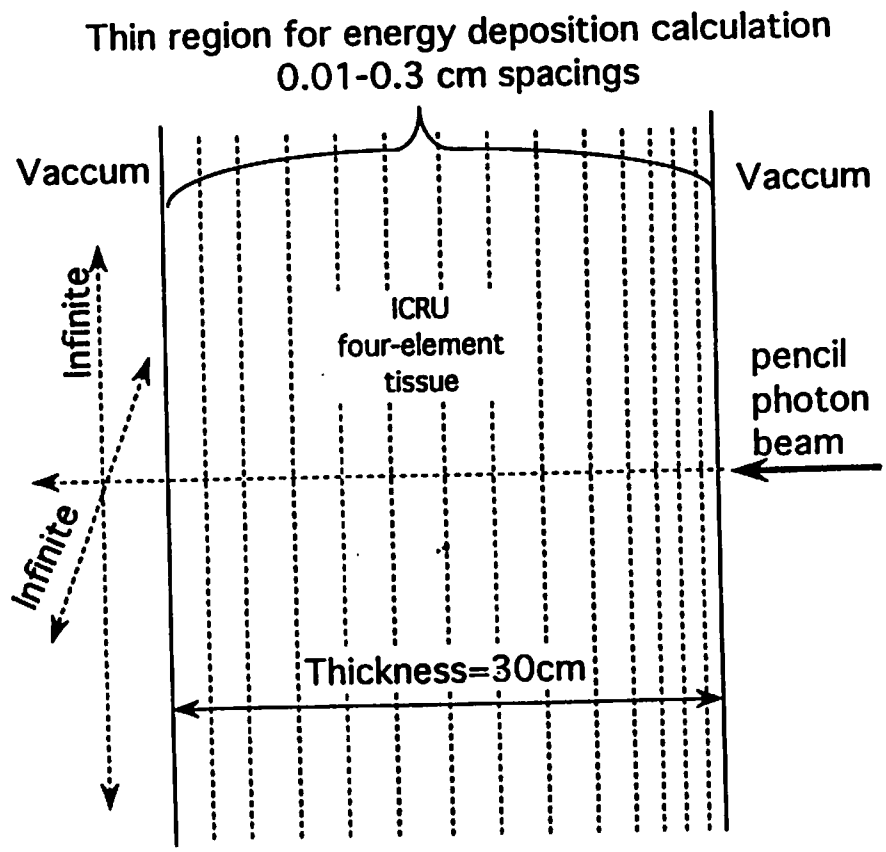

Fig. 3 Model for calculation of dose equivalents in a 30cm-thick slab phantom of ICRU four-element tissue.

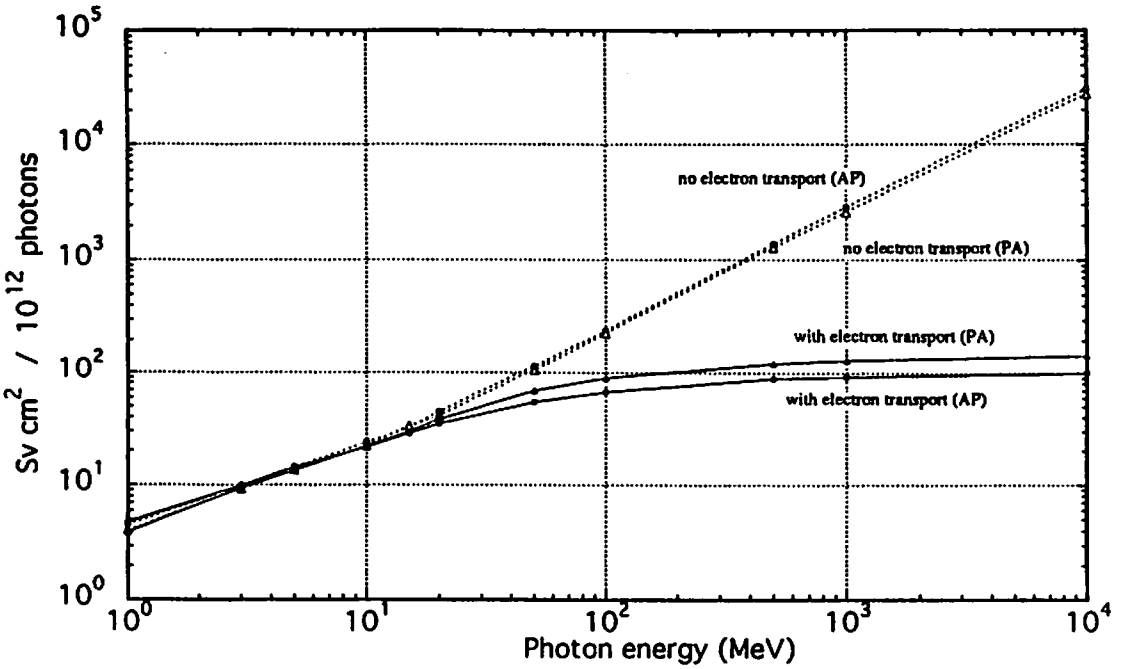

Fig. 4 Effective dose calculated with secondary electron (PA and AP condition, straight lines) and with no secondary electron transport (dashed line).vs. incident photon energy.

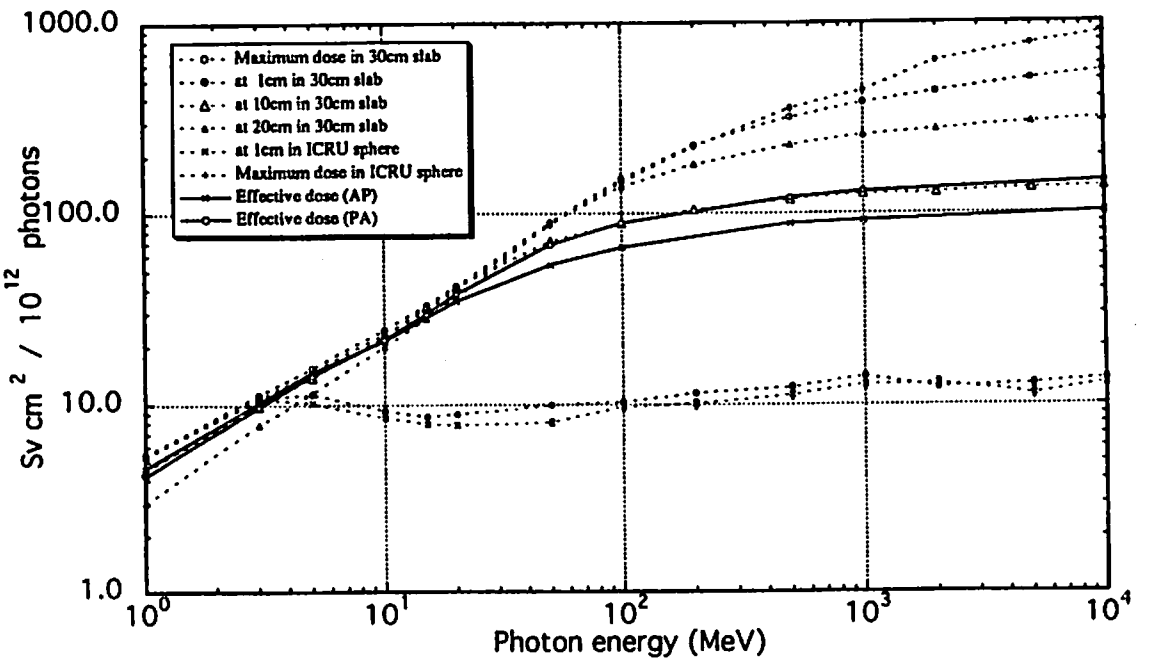

Fig. 5 Effective dose (PA and AP condition, straight lines) and dose equivalents in 30cm-slab (circles and triangles with dashed line) or ICRU sphere (crosses with dashed line).vs. incident photon energy.

DEVELOPMENT OF AN EGS4/PRESTA USER CODE WRITTEN BY THE CG DESCRIPTION

T. SUGITA *Visible Information Center,Inc.*
440 Muramatu,Tokai-mura,Ibaraki-ken,319-11,JAPAN

T. TORII and H. ANDO
O-arai Engineering Center
Power Reactor and Nuclear Fuel Development Corporation
4002 Narita,O-arai-machi,Ibaraki-ken,311-13,JAPAN

Abstract

The geometry description of radiation shielding codes, such as QAD-CG and MORSE-CG, is often written by the combinatorial geometry (CG) method. However any EGS4/PRESTA user code with the CG method is not yet reported. Since the macro, called $CALL-HOWNEAR, is necessary to use the PRESTA algorithm on EGS4, it is difficult to write complicated geometries on EGS4/PRESTA. Then we developed an EGS4/PRESTA user code, which can be written by 3 dimensional CG method and it did the way that can evaluate influence of the step size for low energy electrons and influence of a calculative geometry. This paper described an user code using the CG method, named PRESTA-CG. Furthermore we reported comparison of the response of an ionization chamber with the UCSAMPCG which is employed the CG description for original EGS4.

1. Introduction

For the application of EGS4[1] to simulate electro-magnetic shower for a thin detector and gas detector, EGS4 cannot simulate well. To resolve this problem, the ESTEPE option[2],which reduces the step size of an electron from the default value, was used for examples by Lindstrom et al.. However ESTEPE is still a pragmatic restriction of the step-size and depends on both the material and its size. Also, calculations using the ESTEPE option take more CPU-time than do those with the default EGS4 especially for small ESTEPE value. As a more logical and convenient method to overcome these difficulties,the PRESTA algorithm(Parameter Reduced Electron-Step Transport Algorithm)[3],which was developed by Bielajew and Rogers to improve the electron transport in EGS4 in the low-energy region, was tested for a simulation of a sampling calorimeter. The PRESTA algorithm involves a path-length correction algorithm,a lateral correction algorithm and a boundary crossing algorithm.

algorithm involves a path-length correction algorithm,a lateral correction algorithm and a boundary crossing algorithm.

To use EGS4, the user must write a "User Code". This consists of MAIN program and the subroutines HOWFAR and AUSGAB. A number of geometry subprograms and their macro equivalents are distributed with the EGS4 Code Systems in order to make it easier to write HOWFAR.

However any EGS4/PRESTA user code with the CG method is not yet reported. Since the macro, called $CALL-HOWNEAR, is necessary to use the PRESTA algorithm on EGS4, it is difficult to write complicate geometries on EGS4/PRESTA. Then we developed an EGS4/PRESTA user code, which can be written by 3 dimensional CG method and it did the way that can evaluate influence of step size of low energy electrons and influence of calculative geometry. This paper described an user code using CG method, named PRESTA-CG.

2. How to create user code

Main point of making of the PRESTA-CG user code is definition of the macro $CALL-HOWNEAR and the subroutine HOWFAR[4,5](refer table 1). We show the scheme in the following.

(1) Definition of the macro $CALL-HOWNEAR(#).

We defined the macro $CALL-HOWNEAR(#) with the CG method(refer table 2). The macro $CALL-HOWNEAR(#) gives minimal length, that becomes necessary when we use the PRESTA, from current position of corpuscle to zone boundary. Actually the CG method definition RPP,RCC,SPH is added and made the subroutine HWNEAR dealing with the CALL form.

(2) Definition of a macro that corpuscle seeks for distance to current zone boundary in flight direction.

We made the macro $RPPCG1,$RCCCG1,$SPHCG1 seeking for a zone boundary in the CG method(refer table 3).

(3) Definition of macro that find inclusion relation of corpuscle and zone.

We made the macro $RPPCGSH, $RCCCGSH, $SPHCGSH, $SEARCHZON that find inclusion relation of corpuscle place and zone in CG method(refer table 4).

(4) Definition of the COMIN/GEOM/.

We replaced the COMIN/GEOM/ by COMMON name RPPDAT, RCCDAT, SPHDAT, ZONDTA, TVALCG to define the CG method(refer table 5).

(5) Definition of PRESTA control flag.

We added macro $PRESTA-ON for the control that PRESTA carries out handling.

(6) Definition in MAIN routine.

We added following definition in the MAIN routine.

The $PRESTA-INPUTS, initial setting of PRESTA.

The CG method definition data, such as RCC, RPP and SPH(refer figure 1).

The Variables ECUTMN and EK0 for PRESTA.

The addition of COMIN/ELECIN/.

(7) Preparation of subroutine HOWFAR.

Because we let next place and zone of corpuscle decide in HOWFAR from step size and distance to boundary, we made a subroutine HOWFAR coresponding to the CG method.

(8) Preparation of a CONFIGURATION file.

We carried out definition of effect using NRC4MACP.MORTRAN and NRCCAUXP.MORTRAN to a CONFIGURATION file.

3. Computational Results

We reported comparison of the response of an ionization chamber(Radocon 550-3 type) with the UCSAMPCG which is employed the CG description for original EGS4 (refer Table 6).

The calculated results of the PRESTA-CG code are shown in Figure 1. And the response, that we changed ESTEPE by a ESTEPE option, are shown in figure 2. The response used PRESTA-CG is good agreement with that for UCSAMPCG on ESTEPE of 0.05 or lower. It confirms that the PRESTA-CG is useful for the calculation an complex geometry.

4. Conclusions

We have written EGS4/PRESTA by 3 dimensional CG method. This PRESTA-CG can evaluate influence of the step size for low energy electrons and calculate transport under complex geometry. Since the PRESTA-CG is added the fundamental geometry, such as cone, easily, we are extending this code now.

Acknowledgments

We would like to thank H.Hirayama and Y.Namito of KEK for teaching the EGS4 code system and PRESTA.

References

[1] W.R.Nelson,H.Hirayama and D.W.O.Rogers, *The EGS4 Code System*, SLAC-265 (1985).

[2] D.W.O.Rogers, Nucl. Instr. and Meth. **A227**, 535 (1984).

[3] A.F.Bielajew and D.W.O.Rogers, *The Parameter Reduced Electron-Step Transport Algorithm for Electron Monte Carlo Transport*, Nucl. Instr. and Meth., **B18**, 165 (1987).

[4] H. Hirayama, *Advanced Manual for using EGS4* (in Japanese), Proceeding of the Second EGS4 User's Meeting in Japan KEK, Japan, 20-22 (1992).

[5] H.Hirayama, *MC-Simulations with EGS4/PRESTA for an Electro-Magnetic Sampling Calorimeter*, IEEE Trans. Nucl. Sci., **NS-40**, 503 (1993).

Table 1: PRESTA construction in the EGS4 code

```
%E "EGS4.MOR RECEIVED VIA BITNET JAN 29 AT NRCC +MINOR CHANGES"
"*****************************************************************"
"                                STANFORD LINEAR ACCELERATOR CENTER"
SUBROUTINE ELECTR(IRCODE);
"                                  VERSION 4.00 -- 26 JAN 1986/1900"
"*****************************************************************"
      .
      .
$SET-TUSTEP; "TUSTEP RESTRICTION MACRO TEMPLATE"
      .
      .
RETURN; "I.E., RETURN TO SHOWER"
END; "END OF SUBROUTINE ELECTR"

-----------------------------------------------------------------------

REPLACE {$SET-TUSTEP;} WITH
  {;TUSTEP=AMIN1(TUSTEP,RANGE);$BOUNDARY-CROSSING-ALGORITHM;}

"THIS IS THE PRESTA VERSION THAT SETS TUSTEP. AT THIS STAGE THE BOUNDARY "
"CROSSING ALGORITHM IS INVOKED.                                          "

-----------------------------------------------------------------------

REPLACE {$BOUNDARY-CROSSING-ALGORITHM;} WITH
  {;IF(IBCA.EQ.0)[
      $CALL-HOWNEAR(TPERP);
      DNEAR(NP)=TPERP;
      USTMIN=(OMEGMN/BLCC(MEDIUM))*EKE*(EIE+RM)/EIE**2;
      TUSTEP=MIN(TUSTEP,MAX(TPERP,USTMIN));
      IF(TUSTEP.GT.TPERP)[ISHRTN=0;]ELSE[ISHRTN=1;]]}

"THIS IS THE PRESTA BOUNDARY CROSSING ALGORITHM. IT CALCULATES THE SHORTEST "
"DISTANCE TO THE CLOSEST BOUNDING SURFACE AND EQUATES TUSTEP TO IT UNLESS   "
"LESS THAN THE MINIMUM SPECIFIED BY THE USER.                              "
"NOTE ALSO THAT DNEAR IS CALCULATED FOR CHARGED PARTICLES AT THIS STAGE IF  "
"IBCA IS SET TO 0. THE USER SHOULD BE AWARE OF THIS TO AVOID ANY REDUNDANCY."
```

Table 2: Definition of the macro $CALL-HOWNEAR(#)

```
REPLACE{$CALL-HOWNEAR(#);}
 WITH{$CALL-HOWNEAR-FOR-COMBINATORIAL-GEOMETRY({P1 });}

"THIS IS THE MACRO THAT SHOULD RETURN THE CLOSEST PERPENDICULAR DISTANCE TO "
"ANY SURFACE WHICH FORMS A BOUNDARY FOR THE CURREN IN THIS                  "
"APPLICATION IT IS REPLACED BY THE MACRO FOLLOWING WHICH IS SPECIALIZED FOR "
"THE COMBINATORIAL GEOMETRY.                                               "
"IT IS THE USER'S RESPONSIBILITY TO PROVIDE THIS MACRO FOR HIS OWN GEOMETRY."

PARAMETER $MAXDELL=1.0E+30;      "MAX. OF USTEP CHECK"

REPLACE{$CALL-HOWNEAR-FOR-COMBINATORIAL-GEOMETRY(#);} WITH
   {;XL=X(NP);YL=Y(NP);ZL=Z(NP);IRL=IR(NP);
     CALL HWNEAR({P1},XL,YL,ZL,IRL); }

SUBROUTINE HWNEAR(TPERP,XLS,YLS,ZLS,IRL);
    REAL*4 XLS,YLS,ZLS;
    COMIN/GEOM/;
    REAL*8 XL,YL,ZL;
    REAL*8 P1MIN,CLONG1,CLONG2,CLONG3,CLONG4,CLONG5,CLONG6;
    REAL*8 ACYL,BCYL,CCYL;
    XL=XLS;YL=YLS;ZL=ZLS;
    P1MIN=$MAXDELL;
    DO I=1,NBBODY(IRL) [
         .
         .
      DO J=1,ISPHIN [
       IF(IABS(NBZONE(I,IRL)).EQ.NBSPH(J)) [
         CLONG1=DABS(XL-SPHPNT(1,J));
         CLONG2=DABS(YL-SPHPNT(2,J));
         CLONG3=DABS(ZL-SPHPNT(3,J));
         CLONG4=DABS(SPHPNT(4,J)
              -DSQRT(CLONG1*CLONG1+CLONG2*CLONG2+CLONG3*CLONG3));
         P1MIN=DMIN1(CLONG4,P1MIN);
       ]]
         .
         .
   ]
   TPERP=P1MIN;
   RETURN;
   END; "END OF SUBROUTINE HWNEAR"
```

Table 3: The macro $SPHCG1

```
"-------------------------------------------------------------------"
"        MACRO-ROUTINE FOR SPH GEOMETRY (CG VERSION)                "
"-------------------------------------------------------------------"

PARAMETER $MXSPH=50;       "MAX. NO. OF SPHERES"
PARAMETER $DELSPH=1.0E-04; "CLOSEST ALLOWABLE DISTANCE TO SURFACE"

"SPHCG1------COMMON BLOCK FOR $SPHCG1 MACRO"

REPLACE {;COMIN/SPHDTA/;} WITH
  {;REAL*8 SPHPNT;COMMON/SPHDTA/SPHPNT(4,$MXSPH),NBSPH($MXSPH),ISPHIN;}

REPLACE {$SPHCG1(#);}
WITH{;UDOTAU=U(NP);UDOTAV=V(NP);UDOTAW=W(
NP);
  XL=X(NP);YL=Y(NP);ZL=Z(NP);
  CALL SPHCG1({P1},XL,YL,ZL,UDOTAU,UDOTAV,UDOTAW);}


SUBROUTINE SPHCG1(IZON,XLS,YLS,ZLS,UNP,VNP,WNP);
 COMIN/GEOM/;
 REAL*4 XLS,YLS,ZLS,UNP,VNP,WNP;
 REAL*8 XL,YL,ZL,UDOTAU,UDOTAV,UDOTAW,UDOTR;
 REAL*8 ASPH,BSPH,CSPH,ARGSP,ROOTSP;
 UDOTAU=UNP;UDOTAV=VNP;UDOTAW=WNP;XL=XLS;YL=YLS;ZL=ZLS;ASPH=1.0;
   BSPH=((XL-SPHPNT(1,IZON))*UDOTAU+(YL-SPHPNT(2,IZON))*UDOTAV
       + (ZL-SPHPNT(3,IZON))*UDOTAW)/ASPH;
   CSPH=(XL-SPHPNT(1,IZON))*(XL-SPHPNT(1,IZON))
       +(YL-SPHPNT(2,IZON))*(YL-SPHPNT(2,IZON))
       +(ZL-SPHPNT(3,IZON))*(ZL-SPHPNT(3,IZON))
       -SPHPNT(4,IZON)*SPHPNT(4,IZON);
   ARGSP=BSPH*BSPH-CSPH;
   IF(ARGSP.GE.0.0) [
     ROOTSP=DSQRT(ARGSP);
     IF(CSPH.LE.0.) [              " INSIDE"
       UDOTR=(-BSPH+ROOTSP)/ASPH;
       IF(UDOTR.GE.0.) [ITVALM=ITVALM+1;ATVAL(ITVALM)=UDOTR;]
     ]
     ELSE [
       UDOTR=(-BSPH-ROOTSP)/ASPH;
       IF(UDOTR.GE.0.) [ITVALM=ITVALM+1;ATVAL(ITVALM)=UDOTR;]
       UDOTR=(-BSPH+ROOTSP)/ASPH;
       IF(UDOTR.GE.0.) [ITVALM=ITVALM+1;ATVAL(ITVALM)=UDOTR;]
     ]
   ]
   RETURN;
   END;
```

Table 4: The macro $SPHCGSH

```
"$SPHCGSH---MACRO REPLACEMENT FOR SUBROUTINE SPHCGSH"

REPLACE {$SPHCGSH(#,#,#,#,#,#);}
WITH{;IF(({P3}-SPHPNT(1,{P1}))*({P3}-SPHPNT(1,{P1}))
    +({P4}-SPHPNT(2,{P1}))*({P4}-SPHPNT(2,{P1}))
    +({P5}-SPHPNT(3,{P1}))*({P5}-SPHPNT(3,{P1}))
      .GT.SPHPNT(4,{P1})*SPHPNT(4,{P1}))
      [IF({P2}.GT.0) [{P6}=0;]
  ]
  ELSE [
      IF({P2}.LT.0) [{P6}=0;]
  ]
}
```

Table 5: Definition of the COMIN/GEOM/

```
"GEOMETRICAL INFORMATION"

REPLACE {;COMIN/GEOM/;} WITH
 {;COMIN/RPPDTA,SPHDTA,RCCDTA,ZONDTA,TVALCG/;}
```

Table 6: Example of system definition of PRESTA-CG

```
*  MATERIAL COUNT     DEP.No.
      3                 3
*  MATERIAL NAME
AIR
ACRYLE
AIR1
*GEOMETRY
*        1         2         3         4         5         6         7
*234567890123456789012345678901234567890
12345678901234567890123456789
  RCC     0.00      0.00      0.00      0.00      0.00      17.30
          0.235
  RCC     0.00      0.00      3.11      0.00      0.00      11.98
          2.67
  RCC     0.00      0.00      3.11      0.00      0.00      11.98
          3.11
  SPH     0.00      0.00      3.11      2.67
  SPH     0.00      0.00      3.11      3.11
  SPH     0.00      0.00     15.09      2.67
  SPH     0.00      0.00     15.09      3.11
  SPH     0.00      0.00      9.10     100.0
  SPH     0.00      0.00      9.10     200.0
  END
*        1         2         3         4         5         6         7
*234567890123456789012345678901234567890123456789012345678901234567890
* COLLECTING ELECTRODE
   Z1          +1
* GAS(AIR)
   Z2          +2      -10R   +4      -10R   +6      -1
* ACRYLIC
   Z3          +3      -20R   +5      -4     -20R   +7      -6      -2
* AIR
   Z4          +8      -3     -5      -7
* ESCAPE
   Z5          +9      -8
  END
*MET
   2
   3
   2
   1
   0
```

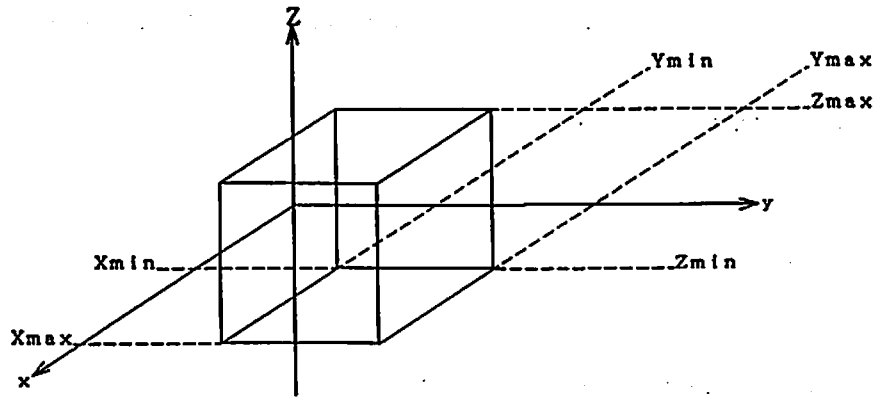

Rectangular Parallelepiped (RPP).

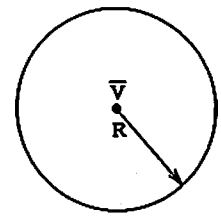

Sphere (SPH).

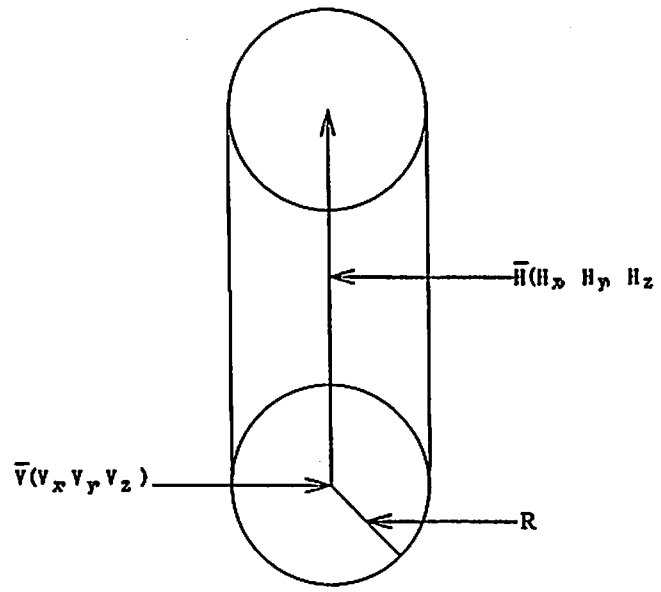

Right Circular Cylinder (RCC).

Fig.1 Body type in PRESTA-CG

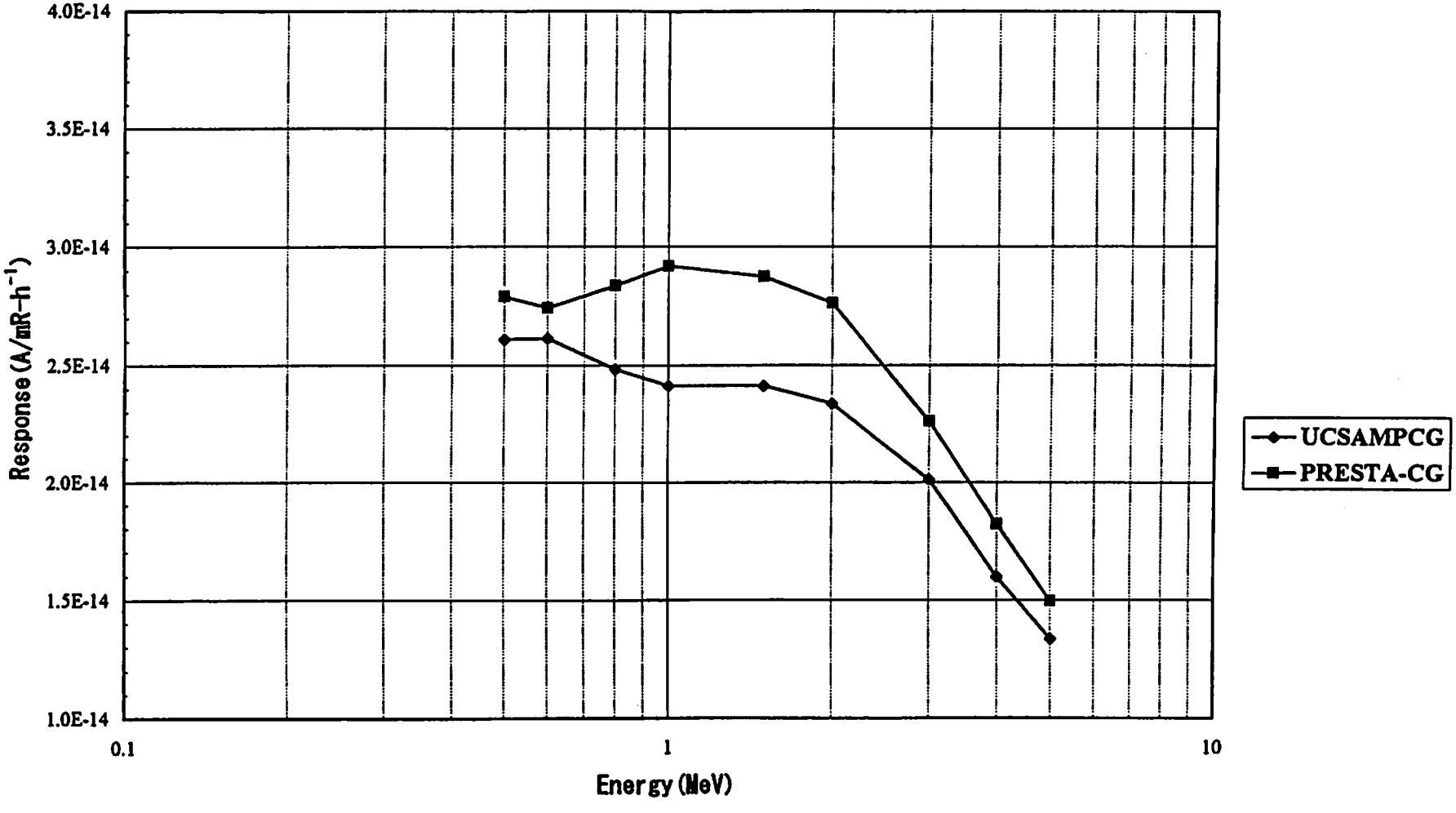

Fig. 2 Comparison of PRESTA-CG and UCSAMPCG

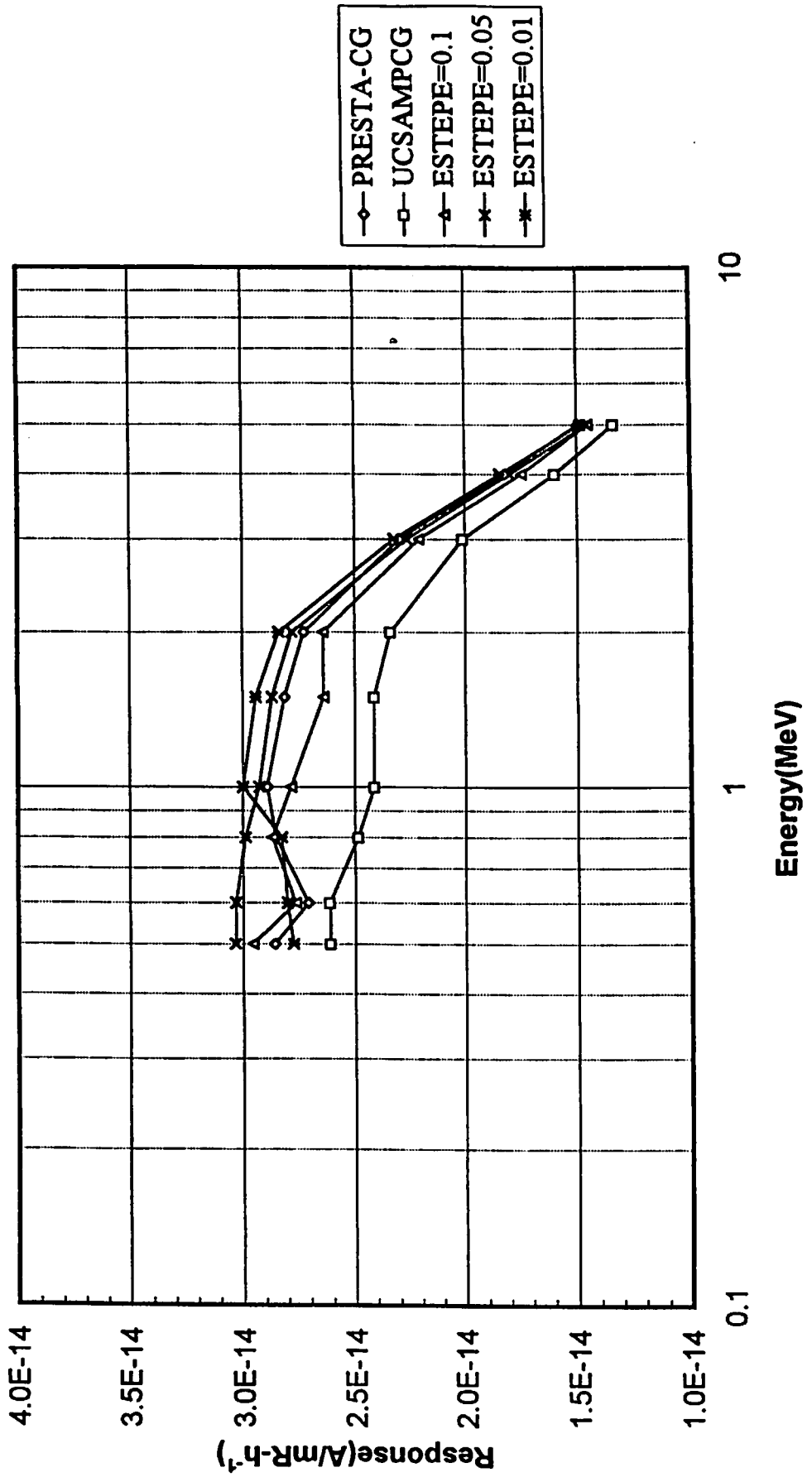

Fig. 3 Comparison of PRESTA-CG and UCSAMPCG with ESTEPE

IMPORTANCE SAMPLING TECHNIQUES AND TREATMENT OF ELECTRON TRANSPORT IN MCNP 4A

K. UEKI

Ship Research Institute

6-38-1 Shinkawa, Mitaka Tokyo 181

1. Abstract of MCNP 4A

The continuous energy Monte Carlo code MCNP[1] was developed by the Radiation Transport Group at Los Alamos National Laboratory and the MCNP 4A version is available, now. The MCNP 4A is able to do the coupled neutron-secondary gamma-ray-electron-bremsstrahlung calculation. The calculated results, such as energy spectra, tally fluctuation chart, and geometrical input data can be displayed by using a work station.

The document of the MCNP 4A code has no description on the subroutines, except few ones of "SOURCE", "TALLYX". However, when we want to improve the MCNP Monte Carlo sampling techniques to get more accuracy or efficiency results for some problems, some subroutines are required or needed to revised.

The following subroutines have been revised and built in the MCNP 4A code.

(a) SOURCE

The SOURCE is revised to treat a complicated or special source conditions of which cannot be described by the input date in the code.

(b) TALLYD

The original TALLYD is for the point detector. We modified the TALLYD for the NESX (Next Event Surface Crossing) Estimator[2]. The NESXE has an excellent quality of the point detector and the surface crossing estimator, so that the FSD (fractional standard deviation) is reduced efficiently as compared with the other estimators[3].

(c) HSTORY

The revised HSTORY was added the functions to calculate and print out the space-energy dependent particle collision density in each cell and energy bin. The Weight Window parameters to do Russian roulette and splitting in the MCNP code can be made from the collision densities with the empirical formula[3].

The Monte Carlo method is essentially a way to solve the Boltzman transport equation as a form of the integral emergent particle density equation[2]. Accordingly, taking the adequate collision densities through the whale shielding system, the FSDs are to reduce at the detector locations.

2. Variance Reduction Techniques

2.1. Weight window

Figure 1 is a more detailed picture of the weight window. Three important weights define the weight window in a space-energy cell

(a) W_L, the lower weight bound,

(b) W_S, the survival weight for particles playing roulette, and

(c) W_U, the upper weight bound.

The user specifies W_L for each space-energy cell on WFN cards. W_S and W_U are calculated using two problem-wide constants, C_S and C_U (entries on the WDWN card), as $W_S=C_S W_L$ and $W_U=C_U W_L$. Thus all cells have an upper weight bound $C_U$times the lower weight bound and a survival weight C_S times the lower weight bound.

2.2 Weight window compared to geometry splitting

Although both techniques use splitting and Russian roulette, there are some important differences.

(a) The weight window is space-energy dependent. Geometry splitting is only space dependent.

(b) The weight window discriminates on particle weight before deciding appropriate action. Geometry splitting is done regardless of particle weight.

(c) The weight window works with absolute weight bounds. Geometry splitting is done on the ratio of the importance across a surface.

(d) The weight window can be applied at surfaces, collision sites, or both.
Geometry splitting is applied only at surfaces.

(e) The weight window can control weight fluctuations introduced by other biasing techniques by requiring all particles in a cell to have weight $W_L < W < W_U$. The geometry splitting will preserve any weight fluctuations because it is weight independent.

(f) In the rare case where no other weight modification schemes are present, importances will cause all particles in a given cell to have the same weight.
Weight windows will merely bound the weight.

(g) The weight windows can be turned off for a given cell or energy regime by specifying a zero lower bound. This is useful in long or large regions where no single importance function applies. Care should be used because when the weight window is turned off at collisions, the weight cut of game is turned on, sometimes causing too many particles to be killed.

3. Treatment of Electrons in MCNP 4A

Electrons

```
Form:  PHYS : E  EMAX  IDES  IPHOT  IBAD  ISTRG  BNUM  XNUM  RNOK  ENUM
```

EMAX	=		upper limit for electron energy in MeV.
IDES	=	0	photons will produce electrons.
	=	1	photons will not produce electrons.
IPHOT	=	0	electrons will produce photons.
	=	1	electrons will not produce photons.
IBAD	=	0	full bremsstrahlung tabular angular distribution.
	=	1	simple bremsstrahlung angular distribution approximation.
ISTRG	=	0	sampled straggling for electron energy loss.
	=	1	expected-value straggling for electron energy loss.
BNUM	>	0	produce BNUM times the analog number of bremsstrahlung photons.
	=	0	bremsstrahlung photons will not be produced.
XNUM	>	0	produce XNUM times the analog number of electron-induced x-rays.
	=	0	x-ray photons will not be produced by electrons.
RNOK	>	0	produce RNOK times the analog number of knock-on electrons.
	=	0	knock-on electrons will not be produced.
ENUM	>	0	produce ENUM times the analog number of photon-induced secondary electrons.
	=	0	photon-induced secondary electrons will not be produced.

```
Defaults : EMAX = 100 MeV;    IDES,  IPHOT,  IBAD,  ISTRG =0;
           BNUM,  XNUM,  RNOK,  ENUM = 1.
```

(a) EMAX is the upper electron energy limit in MeV. Electron cross sections and related data are generated on a logarithmic energy grid from EMAX down to an energy at least as low as the global energy cutoff for electrons.

(b) IDES is a switch to turn off electron production by photons. The default (IDES=0) is for photons to create electrons in all photon-electron problems and for photons to produce bremsstrahlung photons using the thick-target bremsstrahlung approximation in photon problems run without electrons. In either case the electron default cross section library will be read, which requires considerable processing time. Electron transport is also very slow. However, the neglect of electron transport and bremsstrahlung production will cause erroneously low photon results when these effects are important.

(c) IPHOT is a switch to turn off photon production by electrons. Because photon transport is fast relative to electron transport and is usually required for an accurate physical model, the default (IPHOT=0, which leaves photon production on) is recommended.

(d) IBAD is a switch to turn on the simple approximate bremsstrahlung angular distribution treatment and turn off the full, more detailed model. The electron transport random walk can be done with either the simple or full treatment, but photon contributions to detectors and DXTRAN can use only the simple treatment. The full detailed physics model is more accurate and just as fast as the simple approximate treatment for the electron transport random walk, and is therefore the default (IBAD=0) even though it is inconsistent with the way bremsstrahlung photons contribute to detectors and DXTRAN spheres. Setting IBAD=1 causes the simple treatment to be used for detectors and DXTRAN and the electron random walk, which is self-consistent.

(e) ISTRG is a switch to control the electron continuos-energy slowing down treatment. If ISTRG=1, the expected value for each collision is used; if ISTRG=0 (default), the more realistic sampled value is used. The option of using the expected value is useful for some comparisons to deterministic electron transport calculations.

(f) BNUM is used to control the sampling of bremsstrahlung photons produced along electron substeps. The default value (BNUM=1) results in the analog number of bremsstrahlung tracks being sampled. If BNUM>0, the number of bremsstrahlung photons produced is BNUM times the number that would be produced in the analog case. If the number of tracks is increased, an appropriate weight reduction is made;

if the biasing reduces the number of tracks, the weight is increased. If BNUM=0, the production of bremsstrahlung photons is turned off.

(g) XNUM is used to control the sampling of x-ray photons produced along electron substeps. The default value (XNUM=1) results in the analog number of tracks being sampled. If XNUM>0, the number of photons produced is XNUM times the number that would be produced in the analog case, and an appropriate weight adjustment is made. If XNUM=0, the production of x-ray photons by electrons is turned off.

(h) RNOK is used to control the number of knock-on electrons produced in electron interactions. The default value (RNOK=1) results in the analog number of tracks being sampled. If RNOK>0, the number of knock-on electrons produced is RNOK times the analog number, and an appropriate weight adjustment is made. If RNOK=0, the production of knock-on electrons is turned off.

(i) ENUM is used to control the generation of photon-induced secondary electrons. The default value (ENUM=1) results in an analog treatment. If ENUM>0, ENUM times the analog number of secondaries will be produced, and an appropriate weight adjustment is made. If ENUM=0, the generation of secondary electrons by photons will be turned off.

In any of these biasing schemes, increasing the population of photons also increases the population of electrons because the additional photon tracks create photoelectrons, Compton recoil electrons, pair production electrons, etc. Similarly, increasing the number of electrons will propagate an increase in the population of subsequent generations of the cascade. Because electron transport is slow, a judicious use of ENUM<1 may often be appropriate.

4. Treatment of Bremsstrahlung

BBREM Bremsstrahlung Biasing Card

Form: BBREM b_1 b_2 b_3 ..... b_{49} m_1 m_2 ..... m_n

b_1	=	any positive value (currently unused).
b_2 ..... b_{49}	=	bias factors for the bremsstrahlung energy spectrum.
m_1 ..... m_n	=	list of materials for which the biasing is invoked.
Default	:	None

The bremsstrahlung process generates many low-energy photons, but the higher-energy photons are often of more interest. One way to generate more high-energy photon tracks is to bias each sampling of a bremsstrahlung photon toward a larger fraction of the available electron energy. For example, a bias such as

```
BBREM    1.    1.    46I    10.    888    999
```

would create a gradually increasing enhancement (from the lowest to the highest fraction of the electron energy available to a given event) of the probability that the sampled bremsstrahlung photon will carry a particular fraction of the electron energy. This biasing would apply to each instance of the sampling of a bremsstrahlung photon in materials 888 and 999. The sampling in other materials would remain unbiased. The bias factors are normalized by the code in a manner that depends both on material and on electron energy, so that although the ratios of the photon weight adjustments among the different groups are known, the actual number of photons produced in any group is not easily predictable.

In most problems the above prescription will increase the total number of bremsstrahlung photons produced because there will be more photon tracks generated at higher energies. The secondary electrons created by these photons will tend to have higher energies as well, and will therefore be able to create more bremsstrahlung tracks than they would at lower energies. This increase in the population of the electron-photon cascade will make the problem run more slowly. The benefits of better sampling of the high-energy domain must be balanced against this increase in run time.

5. The Ten Statistical Checks

Version 4A of MCNP makes 10 statistical checks that are designed to assist the user in determining if the result in the TFC bin appears to be based on large N so that a valid confidence interval can be formed. These checks make use of expected reasonably well-behaved tally statistical behavior based on statistical studies of relevant analytic f(x)s. In particular, the estimated mean from long-tailed f(x) distributions tends to be dominated by the largest sampled values. Until the effect of individual extreme values in negligible, confidence intervals may not be valid (MCNP 4A also prints the TFC bin result assuming that the largest sampled x occurs on the next history to aid in this assessment). The TFCs usually have from 10 to 20 values of the mean, RE, VOV, FOM, and slope as a function of N. Both quantity magnitude and N-dependent behaviors are examined. The 10 statistical checks look for the following desirable behaviors:

- Estimated Mean

(a) a non-monotonic behavior in the estimated mean as function of N;

- Estimated Relative Error (RE)

(b) an acceptable magnitude of the estimated RE of the estimated mean (< 0.05 for a point detector tally or < 0.10 for a non-point detector tally);

(c) a nearly monotonically decreasing RE with increasing N;

(d) a nearly $1/\sqrt{N}$RE decrease with increasing N;

- Estimated Variance of the Variance (VOV)

(e) the estimated VOV should be less than 0.10 for all types of tallies;

(f) a nearly monotonically decreasing VOV with increasing N;

(g) a nearly $1/\sqrt{N}$VOV decrease with increasing N;

- Figure of Merit (FOM)

(h) a statistically constant FOM as a function of N;

(i) a non monotonic FOM with increasing N; and

- Empirical History Score PDF f(x)

(j) the estimated slope of the 25 to 200 largest history scores x should be greater than 3 so that the second moment $\int_{-\infty}^{\infty} x^2 f(x)dx$ will exist if f(x) is extrapolated to infinity. (As examples of unacceptable empirical f(x)s, see the Cauchy $f_2(x)$ and point detector $f_4(x)$ in Fig.3 where the slope is 2 and the mean and higher moments do not exist when extrapolated to infinity.)

6. Analysis of 8 MeV Gamma-Ray Lead Penetration Experiment

The gamma-ray lead penetration benchmark experiment of Johnson was analyzed by the MCNP 4A code. The source is neutron capture gamma-ray of Ni. Accordingly, approximately 8 MeV gamma-rays of which the bremsstrahlung must be considered were emitted from the source. Configuration of the experiment is shown in Fig.2. Table 1 is a log plat of the tally probability density function to check the slope in Table 2, Table 2 indicates the results of 10 statistical checks for the tally fluctuation chart bin, in this case the statistical checks are passed all and Table 3 shows the calculation results as the function of source histories.

Comparison of dose equivalent rate attenuation with lead shields between the experiment and the MCNP 4A is summarized in Fig. 3 in which the calculations with and without the bremsstrahlung are included. The calculations with the bremsstrahlung agree well with the experiments within the experimental error up to the maximum thickness

of 15.33 cm. However, the results without the bremsstrahlung underestimate the experiments and the magnitude of the underestimation is 35 (fractional standard deviation) are less than 0.03 for all the calculations.

References

[1] J.F. Briesmeister, Ed., *MCNP-A General Monte Carlo N-Particle Transport Code, Version 4A*, Los Alamos National Laboratory report LA-12625 (1993).

[2] M.B. Emmett, Ed., *The MORSE Monte Carlo Radiation Transport Code System*, ORNL-4972, Oak Ridge National Laboratory (1975).

[3] K. Ueki and A. Ohashi, *Taking Space-Energy-Dependent Importance Function for Russian Roulette and Splitting in Continuous Energy Monte Carlo Calculation*, Proc. of 8th Int. Conf. on Radiation Shielding, PP 1140, Arlington Texas, USA (1994).

[4] W.R. Johnson, et al., *Gamma-ray Attenuation at Energies of Approximately 6 and 8 MeV*, Nucl. Sci. Eng., **43**, 32 (1971).

Table 1 Log plot of tally probability density function for tally 75

unnormed tally density for tally 75 nonzero tally mean(m) = 4.134E-13 nps = 15340 print table 161

abscissa tally	number	num den	log den	ordinate log plot of tally probability density function in tally fluctuation chart bin(d=decade,slope=10.0)
1.00-13	4539	1.44+13	13.158	d----------d----------d----------d----------d----------
1.26-13	2027	5.10+12	12.708	********** ********** ********** ********** **********
1.58-13	2556	5.11+12	12.709	********** ********** ********** ********** *********
2.00-13	620	9.85+11	11.993	********** ********** ********** ********** *********
2.51-13	693	8.74+11	11.942	********** ********** ********** **********
3.16-13	628	6.29+11	11.799	********** ********** ********** **********
3.98-13	485	3.86+11	11.587	********** ********** ********** **********
5.01-13	429	2.71+11	11.433	********** ********** ********** *******
6.31-13	439	2.21+11	11.343	********** ********** ********** *****
7.94-13	462	1.84+11	11.266	********** ********** ********** **
1.00-12	488	1.55+11	11.189	********** ********** **********
1.26-12	521	1.31+11	11.118	********** ********** **********
1.58-12	448	8.96+10	10.952	********** ********** **********
2.00-12	398	6.32+10	10.801	********** ********** **********
2.51-12	299	3.77+10	10.577	********** ********** ******
3.16-12	207	2.07+10	10.317	********** ********** *
3.98-12	74	5.89+09	9.770	********** **********
5.01-12	23	1.45+09	9.163	**********
6.31-12	4	2.01+08	8.303	*
total	15340	1.00+00		d----------d----------d----------d----------d----------

Table 2 Results of 10 statistical checks for the tally fluctuation chart bin for tally 75

results of 10 statistical checks for the estimated answer for the tally fluctuation chart (tfc) bin of tally 75

tfc bin behavior	--mean-- behavior	---------relative error--------- value	decrease	decrease rate	----variance of the variance---- value	decrease	decrease rate	--figure of merit-- value	behavior	-PDF- slope
desired	random	< .05	yes	1/sqrt(nps)	<0.10	yes	1/nps	constant	random	>3.00
observed	random	.01	yes	yes	.00	yes	yes	constant	random	10.00
passed?	yes	yes	yes	yes	yes	yes	yes	yes	yes	yes

Table 3 MCNP 4A results of the Johnson experiment in Fig. 2

		tally	65				tally	75		
nps	mean	error	vov	slope	fom	mean	error	vov	slope	fom
1000	3.8009E-13	.0482	.0135	10.0	58	3.8006E-13	.0482	.0135	10.0	58
2000	3.9454E-13	.0345	.0060	10.0	56	3.9458E-13	.0344	.0060	10.0	57
3000	3.9820E-13	.0275	.0038	10.0	58	3.9822E-13	.0274	.0038	10.0	58
4000	4.0685E-13	.0237	.0026	10.0	58	4.0678E-13	.0237	.0026	10.0	58
5000	4.0426E-13	.0215	.0039	10.0	57	4.0245E-13	.0211	.0021	10.0	59
6000	4.0327E-13	.0196	.0030	10.0	57	4.0179E-13	.0193	.0017	10.0	59
7000	4.0140E-13	.0181	.0024	10.0	58	4.0012E-13	.0179	.0015	10.0	59
8000	4.0658E-13	.0170	.0021	10.0	56	4.0546E-13	.0169	.0014	10.0	57
9000	4.0721E-13	.0160	.0018	10.0	56	4.0622E-13	.0158	.0012	10.0	58
10000	4.0953E-13	.0151	.0015	10.0	56	4.0863E-13	.0150	.0011	10.0	57
11000	4.1180E-13	.0144	.0013	10.0	56	4.1098E-13	.0143	.0010	10.0	57
12000	4.1389E-13	.0138	.0012	10.0	56	4.1294E-13	.0136	.0009	10.0	57
13000	4.1344E-13	.0132	.0011	10.0	56	4.1262E-13	.0131	.0008	10.0	57
14000	4.1512E-13	.0127	.0010	10.0	56	4.1435E-13	.0127	.0008	10.0	57
15000	4.1496E-13	.0123	.0009	10.0	56	4.1424E-13	.0122	.0007	10.0	57
15340	4.1408E-13	.0122	.0009	10.0	56	4.1339E-13	.0121	.0007	10.0	57

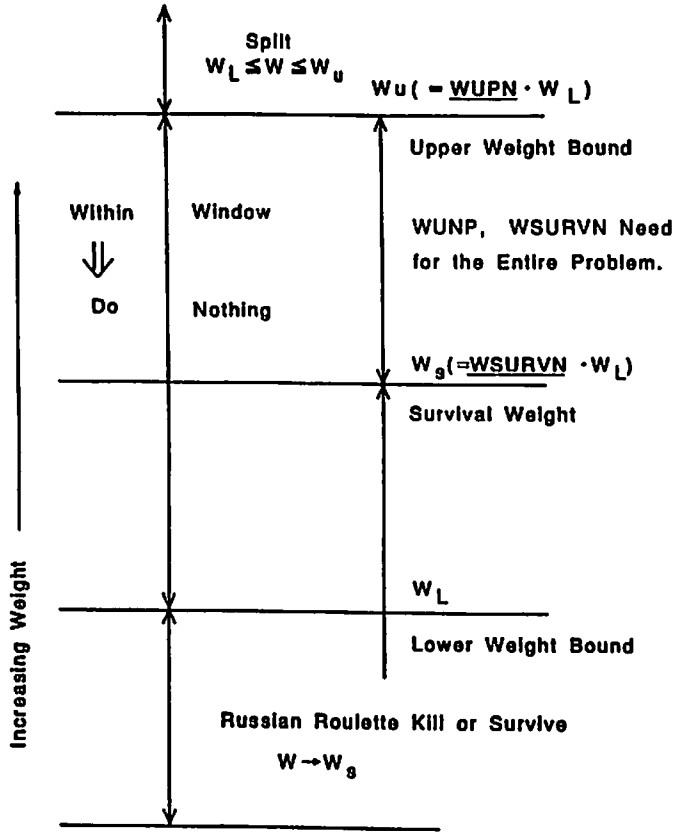

Fig.1 Concept of Weight Window

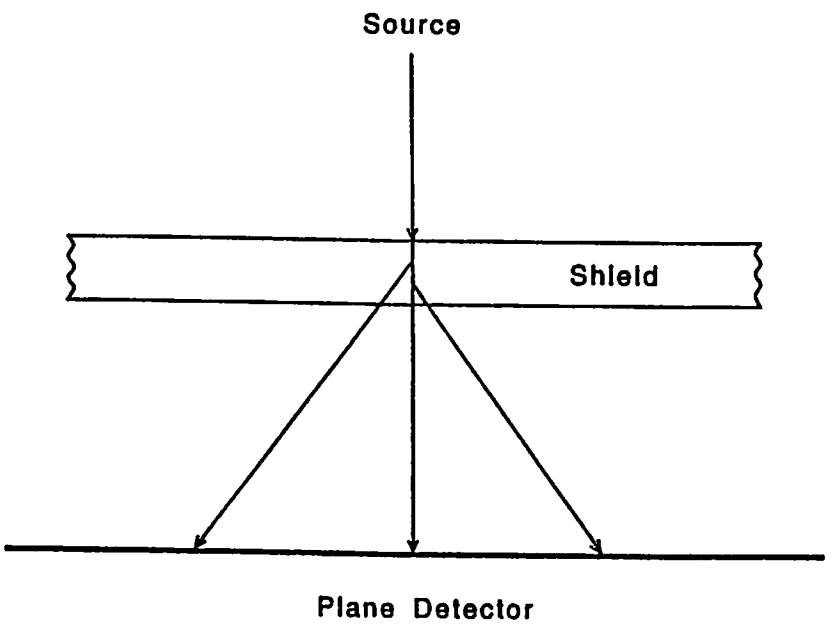

Fig.2 Calculation model of the Johnson experiment. Pencil beam, monodirectional, on a slab shield with an infinite plane detector.

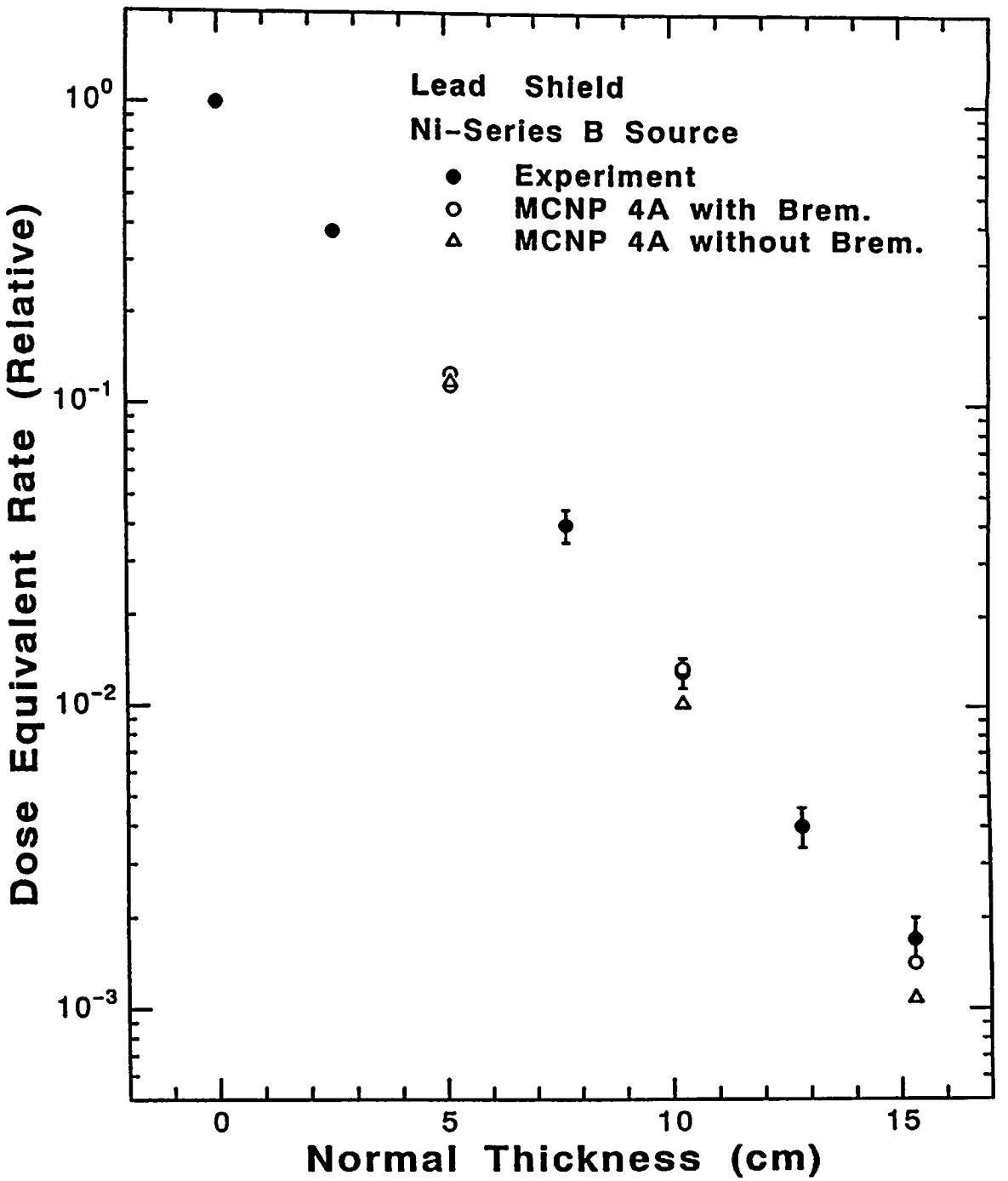

Fig.3 Comparison of dose equivalent rate attenuation with lead shields for Ni-series B gamma-ray source between the experiment[4] and the MCNP analysis.

CALCULATION OF DOSE POINT KERNELS FOR FIVE RADIONUCLIDES USED IN RADIO-IMMUNOTHERAPY

S. OKIGAKI, A. ITO, I. UCHIDA, and T. TOMARU

Department of Physics,
The Cancer Institute, Tokyo
Japanese Foundation for Cancer Research
Kami-Ikebukuro 1-37-1, Toshima-ku, Tokyo 170, JAPAN

Abstract

With the recent interest in radioimmunotherapy, attention has been given to calculation of dose distribution from beta rays and monoenergetic elec-trons in tissue. Dose distribution around a point source of a beta ray emitting radioisotope is referred to as a beta dose point kernel. Beta dose point kernels for five radionuclides such as ^{131}I, ^{186}Re, ^{32}P, ^{188}Re, and ^{90}Y appropriate for radioimmunotherapy are calculated by Monte Carlo method using the EGS4 code system. Present results were compared with the published data of experiments and other calculations. Accuracy and precisions of beta dose point kernels are discussed.

1. Introduction

Calculations of dose distribution based on the measured distribution of radioactivity is required in treatment planning of radioimmunotherapy. Beta dose distribution around a point source of a radioisotope of interestis referred to as a beta dose point kernel. The systematic data of dose point kernels are important as the basis of the calculation of three-dimensional absorbed dose distribution.

Generally, direct measurement of the absorbed dose around beta rays is difficult because of the short ranges of electrons in tissue and absence of appropriate detectors. In spite of these difficulties, some investigators have attempted measurement of the beta dose point kernel.

Loevinger[1] made transmission measurements of planar sources of beta rays from radionuclides through polystyrene sheets, and compared these results with those expected from point sources. Clark et al.[2] measured dose distribution of beta rays from point sources in air. Cross[3] measured dose distribution of beta rays in air and styrofoam with ionization chambers. The obtained results for air were extended to those expected in low Z

media. Cross[4] further made transmission measurements of planar beta sources through aluminium and polyvinyl toluene with an extrapolation ionization chamber. Cole[5] measured transmission, absorption, and reflection of electron beams having broad energy range from 20 eV to 50 keV through thin sheets of cellulose nitrate and Mylar.

Theoretical investigations in beta dose point kernels have been made by radiation physicists. Spencer[6] published a numerical solution to the transport equation of primary electrons in a uniform unbounded medium. He used the moment method with the continuous slowing down approximation (CSDA). As his results agreed well with previous experimental results, this formed the basis of beta dosimetry in both MIRD Pamphlet No.77 and tables of dose distributions by Cross et al.[8]. However, the Monte Carlo simulation made a progress recently in solving this problem. Berger[9] calculated dose point kernels for monoenergetic electrons in water, using the Monte Carlo simulation code(ETRAN). This approach has the advantage of being able to avoid the use of inaccurate CSDA. Rogers and Bielajew[10] calculated absorbed doses from the broad parallel electron beams on slab phantoms using other Monte Carlo code named EGS4. It has been shown that the sampling of electron energy-loss straggling distribution used in ETRAN was incorrect. However, it should be noted that the present version of ETRAN code[11] uses the correct electron energy-loss sampling. To estimate dose point kernels of radionuclides of interest for radioimmunotherapy, Prestwich et al.[12] have calculated the weighted results of monoenergetic electrons by Berger[9]. Simpkin and Mackie[13] have given beta dose point kernels in water for monoenergetic electrons and beta rays emitting radio-nuclides with the EGS4. Cross et al.[14] calculated radial dose distributions around isotropic point sources of monoenergetic electrons and 147 beta emitters in an infinite water medium with the Monte Carlo code named ACCEPT. Their calculated dose distributions for beta emitters are in good agreement with not only experimental results but also other calculations by ETRAN and EGS4, except at very short distance.

The purpose of this paper is to report Monte Carlo calculations of beta dose point kernels in water. EGS4 code was used to calculate beta dose point kernels in water for ^{131}I, ^{186}Re, ^{32}P, ^{188}Re, and ^{90}Y. These radionuclides are of interest in radioimmunotherapy because of their favorable energy of beta rays, half lives, and chemical binding properties to suitable monoclonal antibodies. These dose point kernels for five radionuclidesare compared to those by other investigators described above. The present precision of dose point kernel is discussed.

2. Method

The Monte Carlo code used to calculate the beta dose point kernels in an infinite homogenious water phantom is the PRESTA version[15] of EGS4 code.[16] The electron

transport is governed by the Moliere multiple scattering theory. Generally, the transport step size is restricted to the value that corresponds to the energy-loss for a preset fraction of ESTEPE. Default ESTEPE is set to 0.02 and AP(a cutoff energy for photons) is set to 10 keV. However, PRESTA calculates the variable and optimal step size for the current electron energy, so that electron transport calculation is faster than fixed fraction ESTEPE algorithm. The geometry for calculation is a sphere and spherical shells. The shell thickness is taken one hundredth ofthe maximum electron range for each radionuclide. Electron histories of 1.0×10^4 were generated and 10 independent runs were averaged to evaluate the precision of calculation. The beta energy spectra for ^{131}I, ^{32}P, and ^{90}Y are taken from data by Hogan et al.[17] and for ^{186}Re and ^{188}Re data from MIRD Pamphlet No.1018. The conversion and Auger electrons were not taken into account in each beta energy spectrum of ^{131}I, ^{186}Re, and ^{188}Re.Beta dose point kernel F(r) is given by the following equation

$$F(r) = (\delta E(r)/T_0)/\delta r \tag{1}$$

where $\delta E(r)$ is the energy absorbed in a spherical shell of radius r and thickness δr, and T_0 is initial energy of beta rays. The integral of $F(r)$ is the fraction of electron energy deposited inthe medium. If Y is the radiation(Bremsstrahlung) yield,

$$\int_0^\infty F(r)dr = 1 - Y. \tag{2}$$

3. Results and Discussions

Calculated beta dose point kernels for five radionuclides, *i.e.*, ^{131}I, ^{186}Re, ^{32}P, ^{188}Re, and ^{90}Y, are shown in fig.1. Error bars indicate one standard deviation in the dose point kernel from 10 independent runs, thatis a few percent. Figs.2 through 9 show beta dose point kernels for each radionuclide by present calculation and compare those with other investigators. It is clear that the present calculations of beta dose point kernels provide proper F(r) values.

It is found that all the dose point kernel values near the origin in MIRD Pamphlet No.77 are larger than present ones, as shown in figs.2(^{131}I), 5(^{32}P), and 8(^{90}Y). For example, the F(r) value in MIRD for ^{131}I is 15% larger than present one at r=8.3×10^{-4}g/cm^2. The calculation of kernel values in MIRD does not take conversion and Auger electrons into account. This is the same treatment as our calculation. Thus, the discrepancies areattributed to the use of CSDA in the calculation of kernels in MIRD.

Figs.2(^{131}I), 4(^{186}Re), 5(^{32}P), 7(^{188}Re), and 8(^{90}Y) show discrepancies between the present F(r) functions by EGS4 code and the F(r) functions by the calculations of Prestwich et al.[12] who used the old version of the ETRAN code[9]. The F(r) value by Prestwich et al. for ^{131}I is 10% smaller than present one at r=1.4×10^{-2}g/cm^2 and, for ^{90}Y, their

F(r) value is 32% larger than present one at r=0.64g/cm^2. These large discrepancies are ascribed to the method of the calculation of Prestwich et al., where the in-correct sampling of electron energy-loss straggling distribution was used in the old ETRAN.

Figs.3(^{131}I), 4(^{186}Re), 6(^{32}P), 7(^{188}Re), and 9(^{90}Y) show comparisons between the values of present EGS4 dose kernels and those of the EGS4 dose kernels by Simpkin and Mackie[13] for each radionuclide. The calculation conditions of Simpkin and Mackie[13] differ from the present ones.[13] But, the present F(r) values are in good agreement with F(r) values of Simpkin and Mackie in most coverage of radial distance, except for very short distances for ^{32}P and ^{90}Y as shown in figs.6 and 9. F(r) value of Simpkin and Mackie for ^{32}P (see fig.6) is 5% smaller than present one at r=4.1x10^{-3}g/cm^2. The small discrepancies near the origin are ascribed to a difference in sampling size of a spherical shell. It is confirmed that the present F(r) values for ^{32}P and ^{90}Y agree well with the F(r) values by Simpkinand Mackie within error, if we use the same shell size as Simpkin and Mackie. For ^{131}I (see fig.3), the F(r) values by Simpkin and Mackie is smaller than present ones in the region where a radial distance r is smaller than 4x10^{-2}g/cm^2. For example, the F(r) value by Simpkin and Mackie is 5.8% smaller than the present one at r=1.2x10^{-2}g/cm^2. In the region where r is larger than 6x10^{-2}g/cm^2, F(r) values of Simpkin and Mackie are larger than present F(r) values, *e.g.*, their F(r) value is 9.8% larger than present one at r=6.9x10^{-2}g/cm^2. These discrepancies are ascribed both to a difference in sampling size of a spherical shell and to the neglect of conversion and Auger electrons in energy spectra of incident electrons in our calculation. As shown in figs.4 and 7, the F(r) values by Simpkin and Mackie for ^{186}Re and ^{188}Re are larger than the present F(r) values in a region near the origin, *e.g.*, the F(r) value by Simpkin and Mackie for ^{186}Re is 23% larger than the present one at r=5.4x10^{-3}g/cm^2, and, for ^{188}Re, 22% larger at r=1.3x10^{-2}g/cm^2. These large differences between the values of kernels of Simpkin and Mackie and those of present kernels disappear at deeper region. The reasons for these discrepancies are the neglect of conversion and Auger electrons in beta energy spectra of ^{186}Re and ^{188}Re used in present calculations. The consideration of con-version and Auger electrons in energy spectra of incident electrons is our next subject.

Fig.5 shows a comparison of the values of present dose kernels for ^{32}P and those of dose kernels calculated by Cross et al.[14] using the ACCEPT code. The ACCEPT F(r) values are in agreement with the present F(r) values, except for the region where r<0.15g/cm^2. For ^{131}I and ^{90}Y (see figs.2 and 8), the ACCEPT F(r) values are smaller than the present F(r) values in a region near the origin. For example, the ACCEPT F(r) value for ^{131}I is 10.9% smaller than present one at r=5.8x10^{-3}g/cm^2. The ACCEPT F(r) values are in agreement with the present ones within error in a region far from the origin. We do not

understand these discrepancies at short distances.

4. Conclusions

Beta dose point kernels for five radionuclides, *i.e.*, ^{131}I, ^{186}Re, ^{32}P, ^{188}Re, and ^{90}Y, were calculated by EGS4 Monte Carlo code with PRESTA. The present calculation provides proper F(r) values from the comparison with the F(r) values obtained by other investigators. The readers should pay attention to the F(r) values in MIRD Pamphlet No.77 that have been based on inaccurate CSDA calculation, and those published by Prestwich et al.[12] that use the calculated results by the old version of ETRAN code9,10 with incorrect sampling of electron energy-loss. The present F(r) values are in good agreement with the F(r) values of Simpkin and Mackie[13] for ^{32}P and ^{90}Y. However, for ^{131}I, ^{186}Re, and ^{188}Re, the present F(r) values do not agree with the F(r) values of Simpkin and Mackie, because present calculations do not take conversion and Auger electrons into account. We will in-clude those in near future.

References

[1] R.Loevinger, *The dosimetry of beta radiations*, Radiology, **62**, 74 (1954).

[2] R.K.Clark, S.S.Brar, and L.D.Marinelli, *Ionization of air by beta rays from point sources*, Radiology, **64**, 94 (1955).

[3] W.G.Cross, *The distribution of absorbed energy from a point beta source*, Can. J. Phys., **45**, 2021 (1967).

[4] W.G.Cross, *Variation of beta dose attenuation in different media* Phys. Med. Biol., **13**, 611 (1968).

[5] A.Cole, *Absorption of 20 eV to 50000 eV electron beams in air and plastic*, Radiat. Res., **38**, 7 (1969).

[6] L.V.Spencer, *Theory of electron penetration*, Phys. Rev., **98**, 1597 (1955).

[7] M.J.Berger, *Distribution of absorbed dose around point sources of electrons and beta particles in water and other media*, MIRD Pamphlet No.7, J. Nucl. Med., **12:Suppl. No.5**, 5 (1971).

[8] W.G.Cross, H.Ing, N.O.Freedman, and J.Mainville, *Tables of beta-ray dose distributions in water, air, and other media* , AECL-7617 (1982).

[9] M.J.Berger, *Improved point kernels for electron and beta-ray dosimetry*, NBSIR 73-107 (1973).

[10] D.W.O.Rogers and A.F.Bielajew, *Differences in electron depth-dose curves calculated with EGS and ETRAN and improved energy-range relationships*, Med. Phys., **13**, 687 (1986).

[11] S.M.Seltzer, *An overview of ETRAN Monte Carlo Methods*, in eds. T.M.Jenkins, W.R.Nelson, and A.Rindi, Monte Carlo transport of electrons and photons, Plenum Press (1988).

[12] W.V.Prestwich, J.Nunes, and C.S.Kwok, *Beta dose point kernels for radionuclides of potential use in radioimmunotherapy*, J. Nucl. Med., **30**, 1036 (1989).

[13] D.J.Simpkin and T.R.Mackie, *EGS4 Monte Carlo determination of the beta dose kernel in water*, Med. Phys., **17**, 179 (1990).

[14] W.G.Cross, N.O.Freedman, and P.Y.Wong, *Beta-ray dose distributions from point sources in an infinite water medium*, Health Phys., **63**, 160 (1992).

[15] A.F.Bielajew and D.W.O.Rogers, *PRESTA:The Parameter Reduced Electron-Step Transport Algorithm for electron Monte Carlo transport*, Nucl. Instr. and Meth., **B18**, 165 (1987).

[16] W.R.Nelson, H.Hirayama, and D.W.O.Rogers, *The EGS4 code system*, Stanford Linear Accelerator Center Report SLAC-265 (1985).

[17] O.H.Hogan, P.E.Zigman, and J.L.Mackin, *Beta Spectra II. Spectra of Individual Negatron Emitters*, in eds. A.B.Brodsky, CRC Handbook of Radiation Measurement and Protection, Section A, Volume I:Physical Science and Engineering Data, CRC Press (1978).

[18] L.T.Dillman and F.C.Von der Lage, *Radionuclide decay schemes and nuclear parameters for use in radiation-dose estimation*, MIRD Pamphlet No.10, Society of Nuclear Medicine (1975).

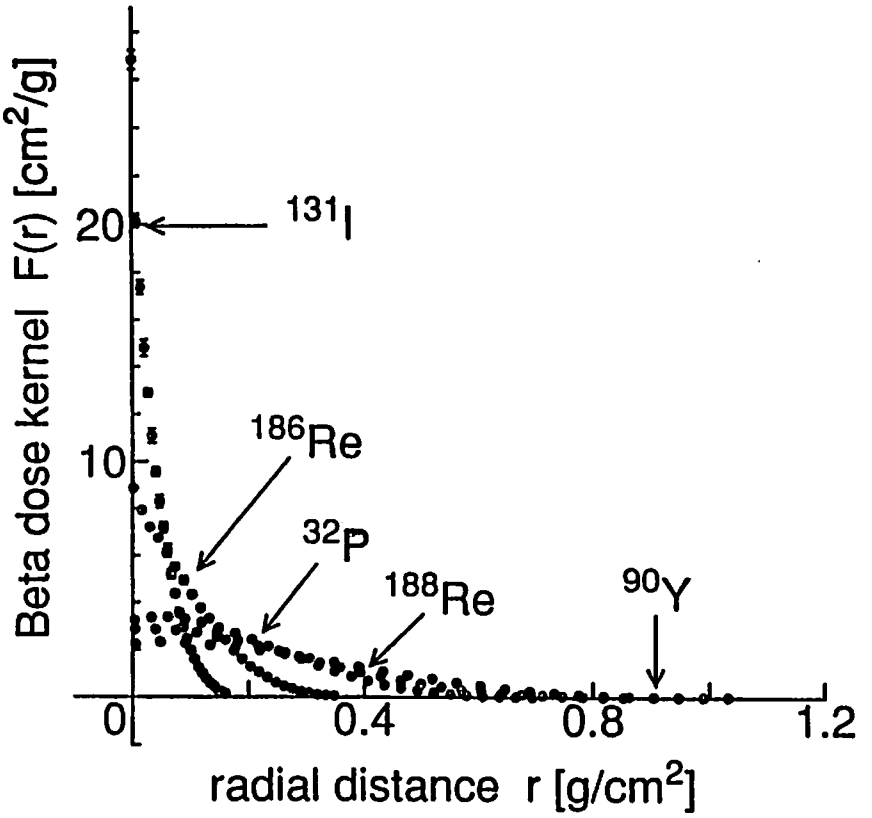

Fig. 1. Beta dose point kernels F(r) for ^{131}I, ^{186}Re, ^{32}P, ^{188}Re, and ^{90}Y

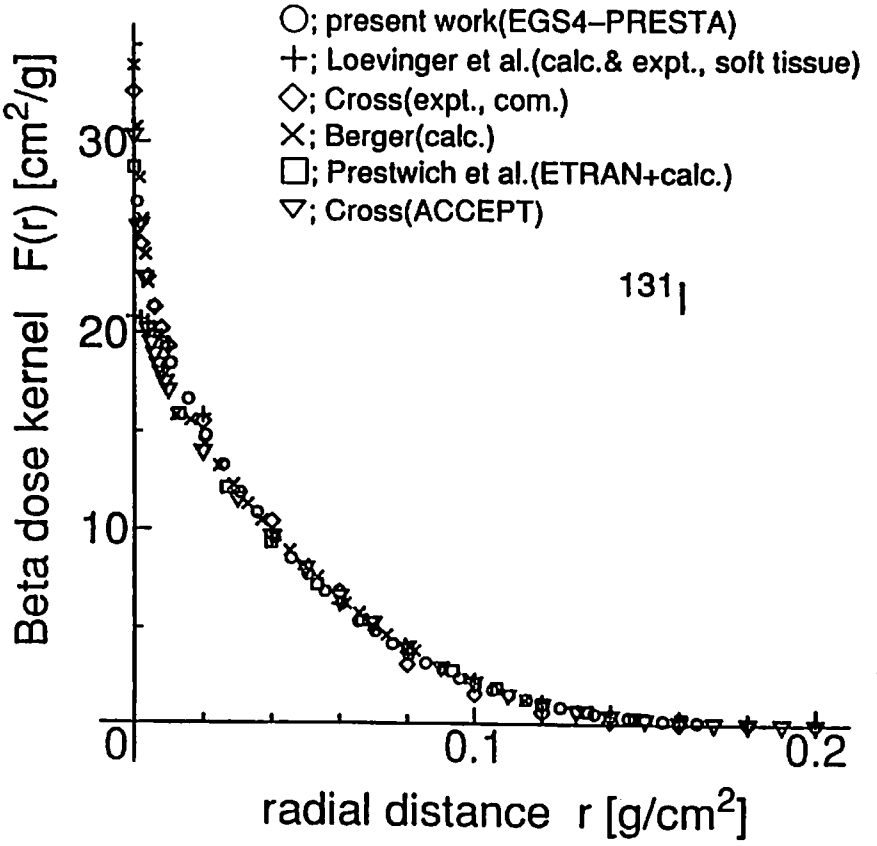

Fig. 2. Beta dose point kernel F(r) for ^{131}I. Results of Loevinger et al. (ref. 1), Berger(ref. 7), Cross et al. (ref. 8), Prestwich et al. (ref. 12), and Cross et al. (ref. 14) shown for comparison.

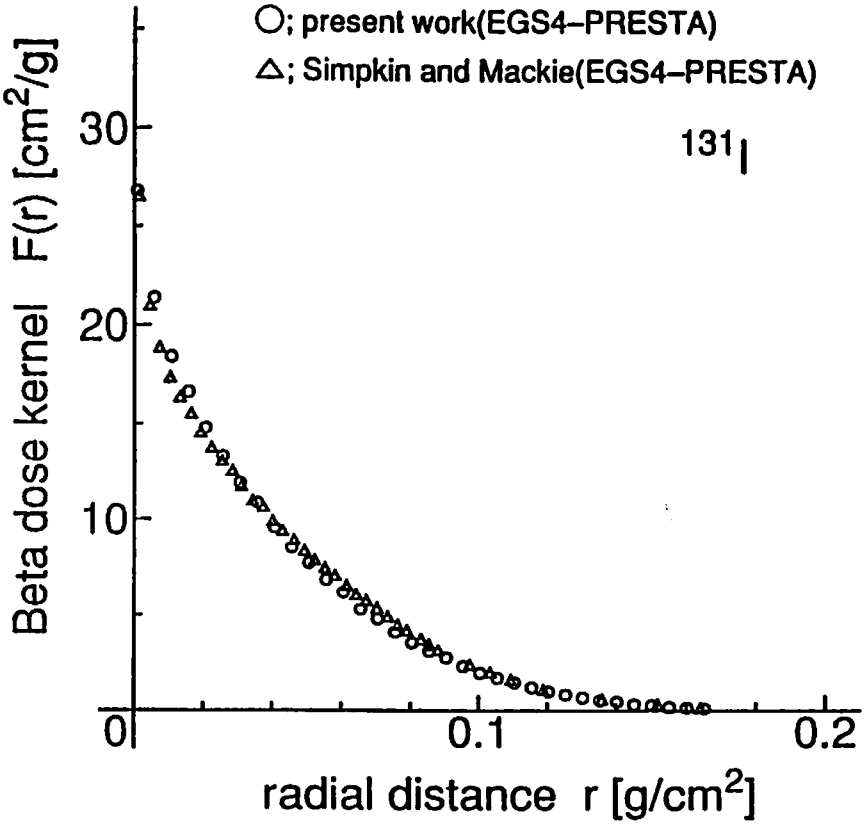

Fig. 3. Comparison of F(r) for ^{131}I and results of Simpkin and Mackie(ref. 13)

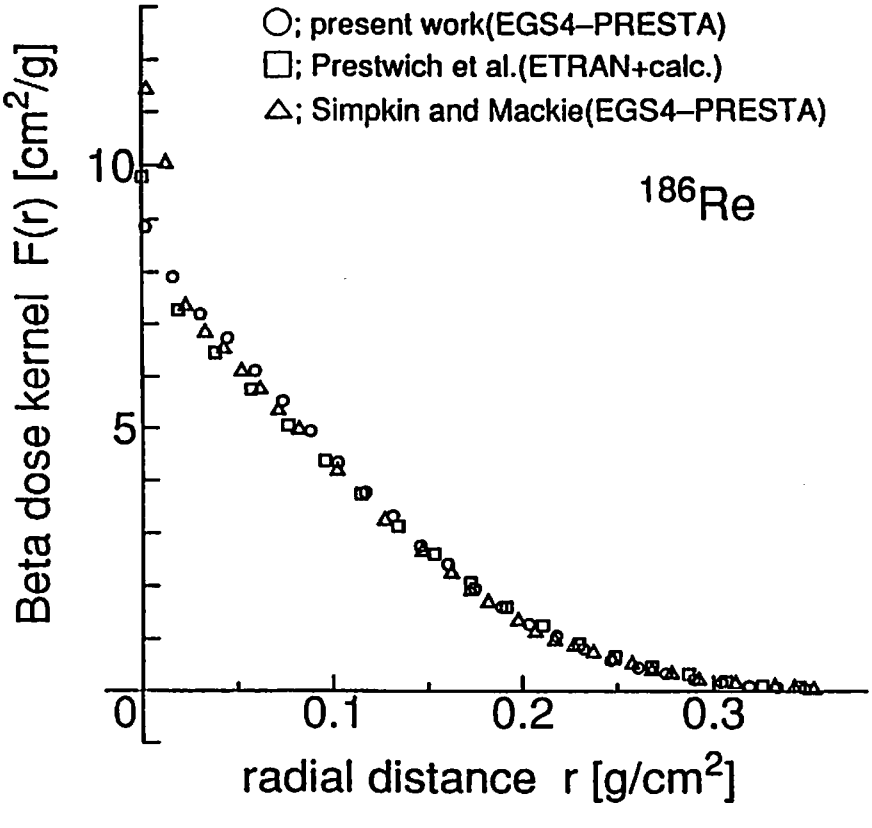

Fig. 4. Beta dose point kernel F(r) for ^{186}Re. Results of Prestwich et al. (ref. 12), and Simpkin and Mackie(ref. 13) shown for comparison.

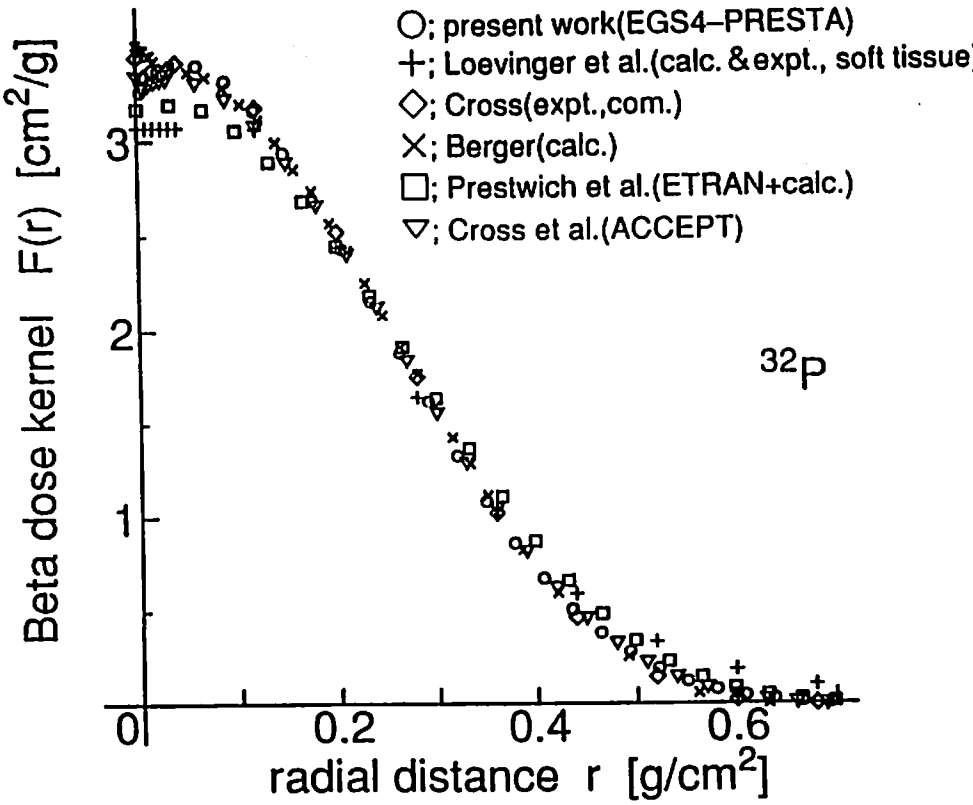

Fig.5. Beta dose point kernel F(r) for ^{32}P. Results of Loevinger et al. (ref. 1), Berger(ref. 7), Cross et al. (ref. 8), Prestwich et al. (ref. 12), and Cross et al. (ref. 14) shown for comparison.

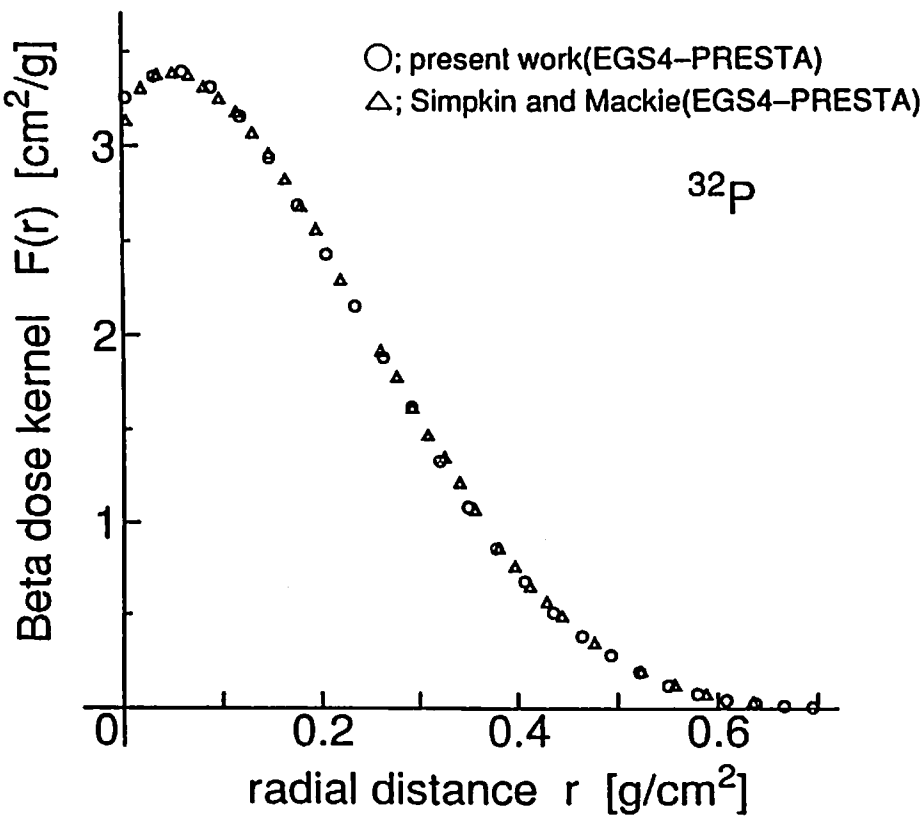

Fig.6. Comparison of F(r) for ^{32}P and results of Simpkin and Mackie(ref. 13)

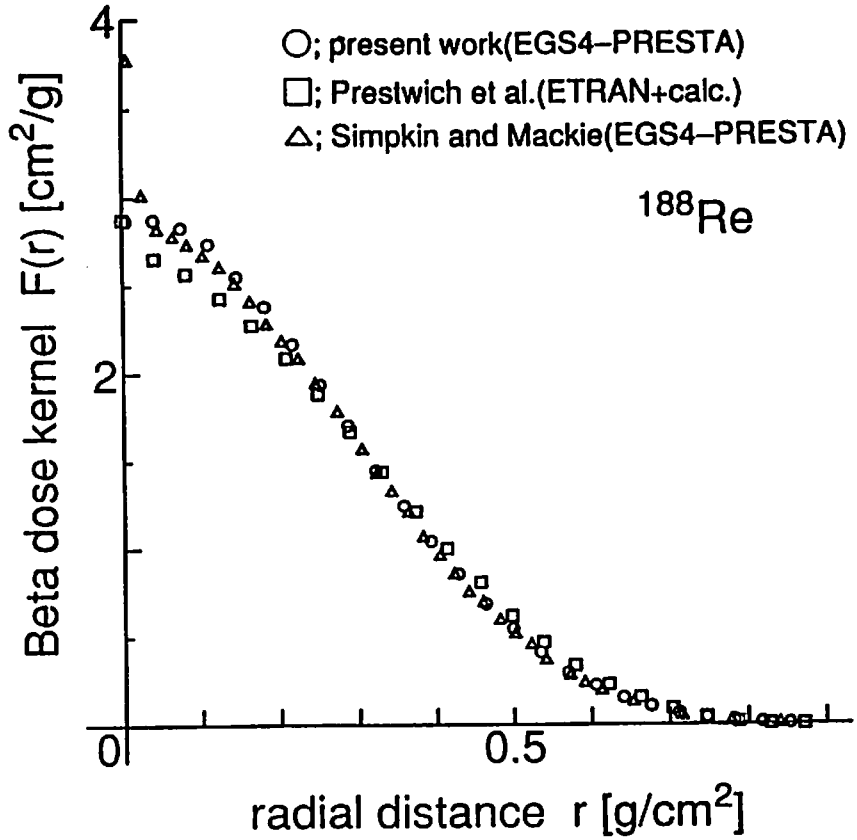

Fig.7. Beta dose point kernel F(r) for ^{188}Re. Results of Prestwich et al. (ref.12), and Simpkin and Mackie(ref.13) shown for comparison.

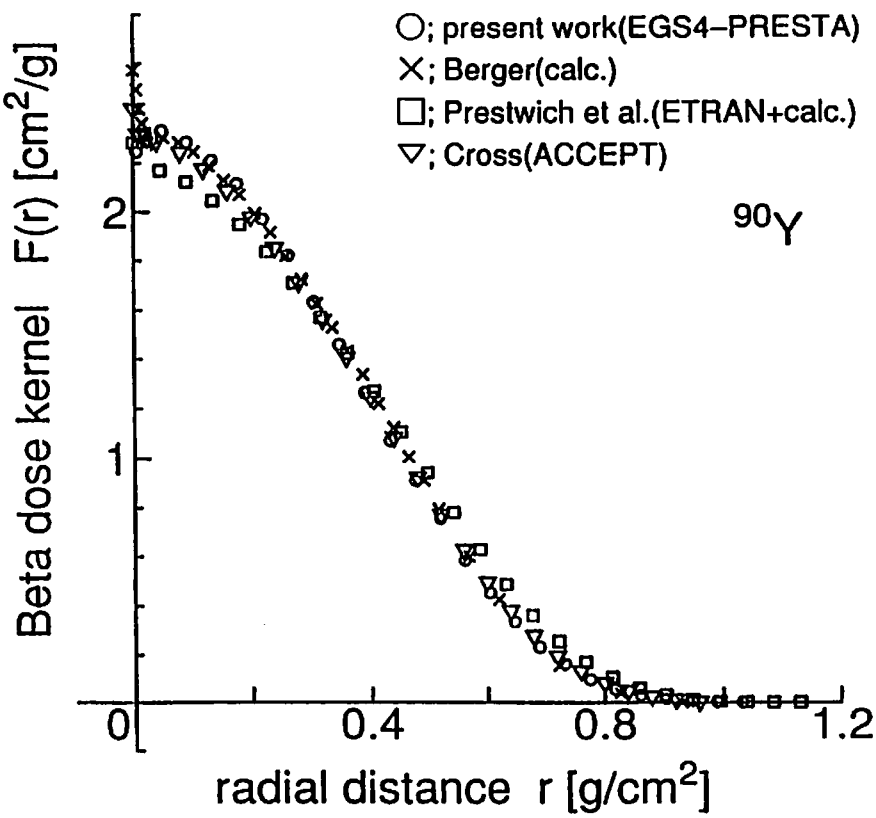

Fig.8. Beta dose point kernel F(r) for ^{90}Y. Results of Berger(ref.7), Prestwich et al. (ref.12), and Cross et al. (ref.14) shown for comparison.

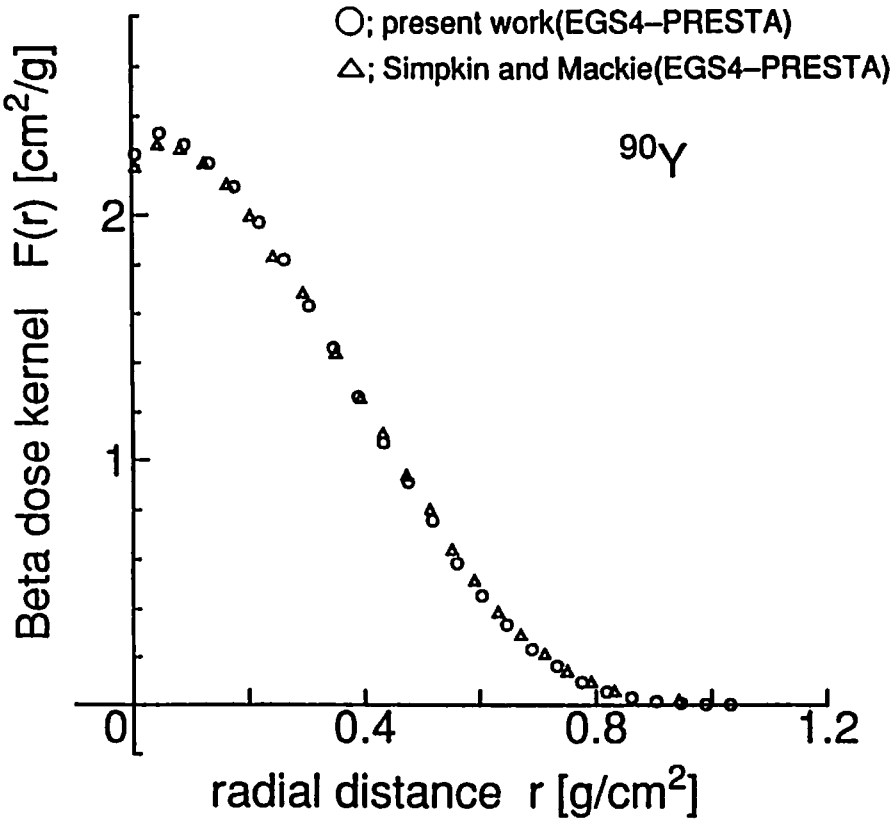

Fig. 9. Comparison of F(r) for ^{90}Y and results of Simpkin and Mackie(ref. 13)

FUNDAMENTAL STUDY OF COMPTON SCATTERING TOMOGRAPHY

R. XIAO, S. SATO, C. UYAMA†, and T. NAKAMURA‡

Department of Biophysical Engineering, Faculty of Engineering Science, Osaka University

†Department of Investigative Radiology, National Cardiovascular Center Research Institute

‡Cyclotron and Radioisotope Center, Tohoku University

1. Introduction

Compton scattering tomography is an imaging technique that forms tomographic images corresponding to distribution of electron densities in an X-rays or γ-rays' irradiating object by measuring Compton scattered photons emitted out of it. Because of its advantage of free choice of measurement geometry, Compton scattering tomography is useful for inspection of defects inside huge objects in industry where X-rays or γ-rays can hardly penetrate the objects[1]. For medical usage, Compton scattered rays are used for densitometry of bone or other tissues. Compton scattering tomographic images, in which densities of body other than attenuation coefficients of body can be shown, are meaningful for medical diagnoses.

Before building a real Compton scattering tomography system for medical applications, we made some fundamental observations upon Compton scattering imaging process through Monte Carlo simulation in order to testify feasibility of the imaging and to seek for an available scheme of system design. EGS4 code system[2] is used for simulation of transport processes of photons in an imaged object. Multiple scattering, one of factors that influence quantity of Compton scattering images, is evaluated here. Some methods to overcome multiple scattering are proposed and their effects are discussed below.

2. Principle of Compton scattering tomography

A beam of X-rays or γ-rays attenuates in its intensity by interactions of photoelectric absorption, Compton scattering, Rayleigh scattering and electron-positron pair production while it is passing through an object. Compton scattering predominates in medical imaging processes where photon energy is about 0.1keV $\sim$ 1MeV and elements of body are of low

atomic numbers. Principle of Compton scattering tomography is illustrated in figure 1. A beam of X-rays radiates into an object and Compton scattering occurs along its path. Scattered photons coming from a point D and emmitting in scattering angle θ can pass through the collimator shown in the figure and enter in detector S. Photon count in detector S can be expressed as:

$$N_s = N_0 A_{AD} \frac{d\sigma_{c,e}}{d\Omega} \Delta\Omega n_e \Delta V A_{DB} + N_n \tag{3}$$

where, N_0 is photon count of incident X-rays; $d\sigma_{c,e}/d\Omega$ is differential Compton scatter cross-section given by Klein-Nishina formula[3]; $\Delta\Omega$ is solid angle of detector S to point D; n_e is electron density at point D; ΔV is volume of point D; A_{AD} is attenuation factor of incident X-rays from A to D; A_{DB} is attenuation factor of scattered X-rays from D to B; N_n is photon count of multiple scattering and others. It is seen from equation (1) that photon count N_0 of scattered X-rays in detector S is dependent on electron density n_e at point D. Compton scattering tomographic image is formed by measuring scattered photons in such a way for every point on a cross section inside an object.

It should be noted that distribution of electron densities inside an object can be derived by Compton scattering tomography only if materials dependent parameters besides n_e in equation (1), which are N_n, A_{AD} and A_{DB}, are evaluated correctly. N_n is mainly counted from multiple scattering. It appears as a background noise in Compton scattering tomography and may make images blurred. We discuss only multiple scattering together with some techniques to eliminate it here, leaving study of A_{AD} and A_{DB} to be done later.

3. Design of detecting system

As Compton scattering may occur at any point along path of incident beam, a collimator shown in figure 1 and figure 2 is needed to select only those scattered photons that are emitted in scattering angle θ from a special point, say focal point D, to be detected by detector S. This collimator is named as θ-collimator. In consideration of efficiency of detecting scattered photons, both detector S and θ-collimator are designed in an annular shape such that all scattered photons emmitting along the cone shown in figure 2 from vertex point D can pass through θ-collimator and access the detector.

Although single Compton scattering must occur on path of incident beam, multiple scattering may originates from anywhere inside an object. This fact makes another type of collimator, which is shown in figure 3, to be used to shield multiple scattering. The collimator consists of a number of lamellas positioned radially to path of incident beam. All singly scattered photons coming from path of incident beam can pass freely through the collimator but part of multiply scattered photons would be shielded by the lamellas. This collimator is named as ϕ-collimator.

Incident beam is assumed as a beam of monoenergetic X-rays. Energy of a photon scattered along the cone shown in figure 2 is calculated by[3]:

$$E = \frac{E_0}{1 + \frac{E_0}{m_e c^2}(1 - \cos\theta)} \qquad m_e c^2 = 0.511 MeV \tag{4}$$

where, E_0 is energy of incident photon; θ is scattering angle. Because of energy loss in every scattering, multiply scattered photons possess a broad energy distribution. Therefore, singly scattered photons can be picked out by recording energy spectrum of scattered photons and using an energy window to cut off multiply scattered photons.

4. Method of simulation

Phantom for simulation is assumed as a sphere of radius R=5cm that is filled with water. The center of the sphere is positioned at origin O of coordinate system OXYZ (figure 4). A small sphere of radius r=0.5cm at O is supposed as focal point to be discussed. This implies that all singly Compton scattered photons from this small sphere is treated as signal while other scattered photons as noise. A beam of X-rays of 100keV radiates the phantom from its bottom along Z-axis. For convenience of observation, surface of the phantom is divided into 36 band-shaped area and 36 detectors are attached to each of the areas. Scattered photons reached detectors are counted with respect to signal and noise. Ratio of signal count to noise count is calculated to provide a quantitative evaluation of influence of noise in Compton scattering tomography. The noise defined above includes not only multiply scattered photons but also singly scattered photons from non-focal points. We will distinguish these two kinds of noises and put emphasis on noise of multiple scattering. SNR is used to express ratio of signal count to total noise count and SNR_m for ratio of signal count to noise count of multiple scattering.

5. Results of simulation

5.1 SNR and SNR_m of photon count on each surface area

First, we observe components of scattered photons reaching every area on surface of the phantom with respect to signal and noise. SNR and SNR_m are calculated from photon count on each area and are plotted in figure 5, where θ is medium polar angle to Z-axis of each band-shaped area. Maximum values of SNR and SNR_m are about 0.068 and 0.12 respectively, which means that only 7% of the photon count is signal. This implies that Compton scattering tomography is impossible if no technique is adapted to improve SNR. It can be seen from the figure that SNR and SNR_m on areas between $\theta \simeq 35° \sim 60°$ appear greater values than those on other areas. Similar tendencies are shown by simulations with different values of radius of the phantom and energy of

the incident beam, also with different materials filling the phantom. This indicates that benefit of low noise detection can be achieved by placing detectors at these positions.

5.2 SNR_m of using θ-collimator

36 θ-collimators are attached to each area on surface of the phantom. 36 detectors are put behind the collimators. Scattered photons passing through the collimators are counted by the detectors. SNR_m of photon count for every detector is shown in figure 6, where $\Delta\theta$ is a parameter that characterizes θ-collimator as in figure 2. Four types of θ-collimators of different $\Delta\theta$ values are used in simulation. Improvements of SNR_m by use of θ-collimators are obvious in figure 6, e.g., maximum value of SNR_m becomes 0.95 when collimator of $\Delta\theta = 5°$ is used. In this case, SNR_m for detectors at $\theta \simeq 15° \sim 165°$ are greater than 0.45, which shows $6/7 \sim 9/10$ reductions of multiple scattering noise by use of the θ-collimators.

5.3 SNR_m of using ϕ-collimator

Lamellas of ϕ-collimator are attached to surface of the phantom and 36 detectors same as above are placed outside the collimator. ϕ-collimator is also characterized by an angle, called $\Delta\phi$, shown in figure 3. Results of SNR_m of using four different $\Delta\phi$ values' ϕ−collimators are shown in figure 7. It is seen from the figure that ϕ−collimator is also effective to eliminating multiple scattering noise. For detectors at $\theta \simeq 15° \sim 165°$, multiple scattering counts decrease to $1/6 \sim 1/9$ by θ-collimators of $\Delta\phi = 5°$ and maximum SNR_m is 1.

5.4 SNR_m of using energy window

Energies of scattered photons reaching each area on surface of the phantom are recorded and are filtered by an energy window. The central value of energy window for area at θ angle is calculated by equation (2). Width of energy window is expressed as ΔE. Effectiveness of energy window for eliminating multiple scattering noise is tested by three kinds of energy windows of different widths. Figure 8 shows the results of SNR_m. By using an energy window of $\Delta E = 5$keV, multiply scattered photon counts are reduced by $1/3 \sim 1/9$ for detectors at $\theta \simeq 15° \sim 165°$ and maximum SNR_m is 1.

5.5 SNR of using θ-collimator, ϕ-collimator and energy window

Although θ-collimator or ϕ-collimator or energy window is effective to overcome multiple scattering noise, maximum values of SNR_m achieved above are not bigger than 1. It needs to combine the three techniques to get a more satisfying improvement. We use

θ-collimator, ϕ-collimator and energy window together in scattering measurement and evaluate their effects by simulation. Both θ-collimator and ϕ-collimator are attached to surface of the phantom. 36 detectors as above are placed behind the two kinds of collimators. Two combinations with parameters as $\Delta\theta = 10°$, $\Delta\phi = 10°$, $\Delta E = 5$keV and $\Delta\theta = 5°$, $\Delta\phi = 5°$, $\Delta E = 5$keV are used in simulation. SNR are calculated from photon counts and are shown in figure 9. For detectors at $\theta \simeq 60° \sim 120°$, SNR are more than 5 by use of the former and become over 40 by use of the latter. These results suggest that it is possible to use such a detecting scheme in a Compton scattering tomography system.

5.6 Compton scattering tomographic image and transmission CT image

Finally, we give some examples of Compton scatterring tomographic images taken by the system proposed above and reconstructed images of the same cross section by transmission CT. All the images are produced from simulating data. Two phantoms are used. One is a water sphere of radius R=10cm with an aluminum sphere of radius r=0.5cm at (0.5cm, 0, -8.0cm) inside it. The other one is almost the same as above but an additional aluminum sphere of radius r=0.5cm is inserted at (-0.5cm, 0, -8.0cm). Imaged plane is z=-8.0cm. Images of the cross section are shown in figure. The aluminium spheres inside the water sphere can be seen in both of Compton scattering images. Outer bound of the water sphere appears brighter than inner region because scattered photons from the inner suffer more attenuation before they are emmitted out off the water sphere.

6. Conclusion

Imaging process of Compton scattering tomography for a water sphere is simulated with use of EGS4 code system. Multiple scattering in the imaging process is observed. Two kinds of collimators and energy window are suggested to be used in scattering measurement and their effectiveness to eliminating multiple scattering noise is tested by simulation. The results show that some combination of these techniques can suppress the noise at very low level and thus is an available scheme for Compton scattering tomography system.

Acknowledgements

We wish to thank Professor Hirayama in High Energy Physics Institute of Japan and Dr. Takagi in Tohoku University of Japan for their kind help and advises.

References

[1] J. Kosanetzky, G. Harding, K. H. Fischer and A. Meyer, *Compton Back-scatter Tomography of Low Atomic Number Materials with the COMSCAN system*, Technical Information, Phillips

[2] W. R. Nelson, H. Hirayama and D. W. O. Rogers, *The EGS4 Code System, SLAC-Report-265*, 1985.

[3] N. A. Dyson, *X-rays in atomic and nuclear physics*, Cambridge University Press, 1990.

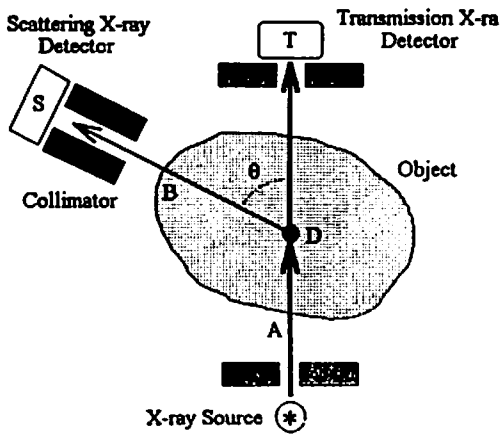

fig.1 Compton scatter Imaging system

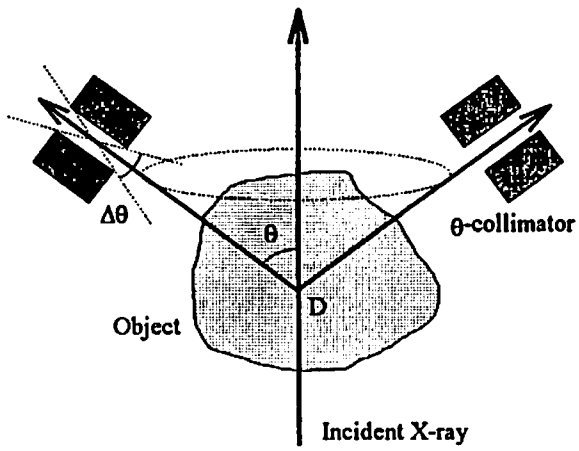

fig.2a θ-collimator

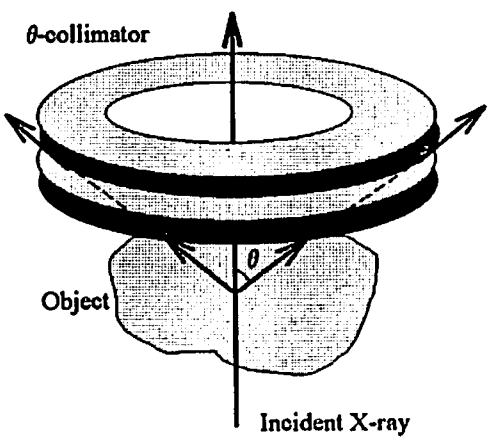

fig.2b θ-collimator

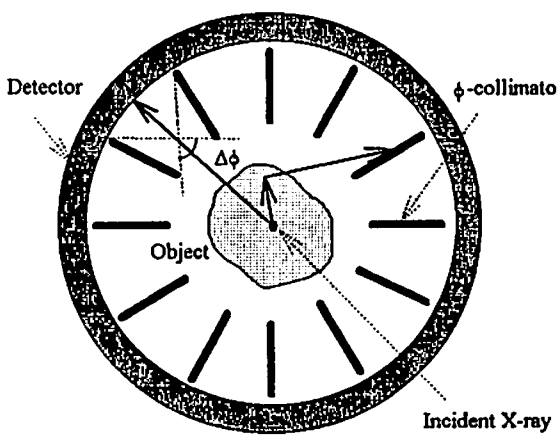

fig.3a ϕ-collimator

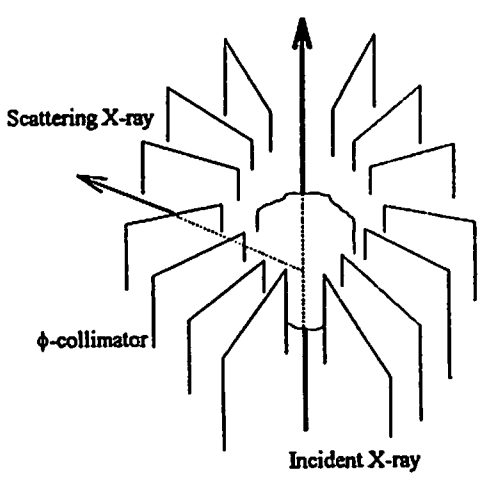

fig.3b ϕ-collimator

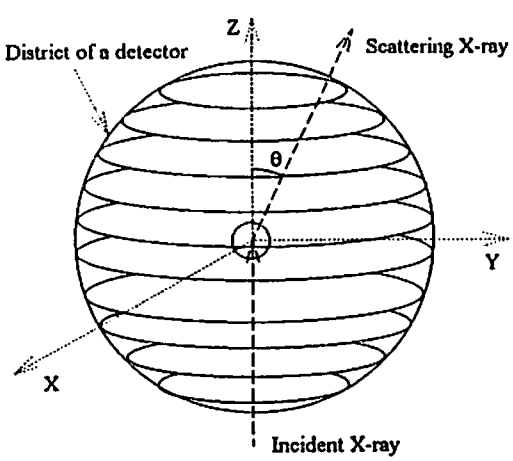

fig.4 Phantom of simulation

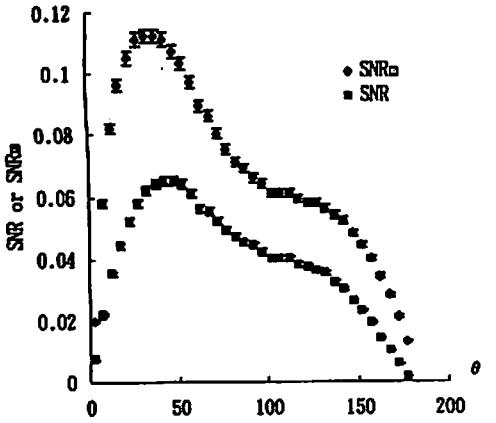

fig.5 SNR and SNRm with neither collimator nor energy window

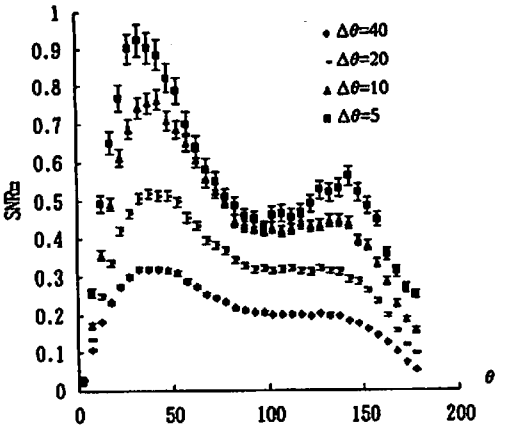

fig.6 SNRm with θ-collimator

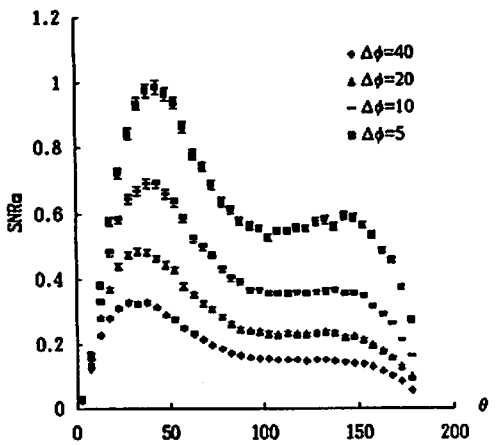

fig.7 SNRm with ϕ-collimator

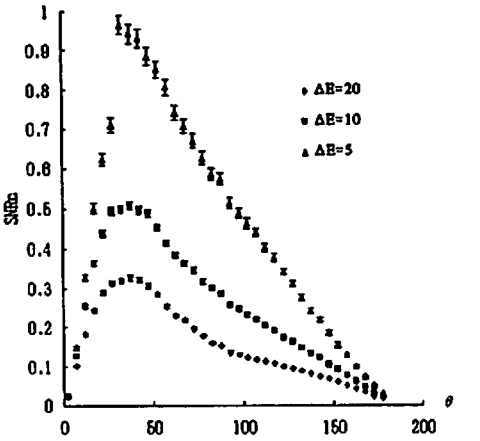

fig.8 SNRm with energy window

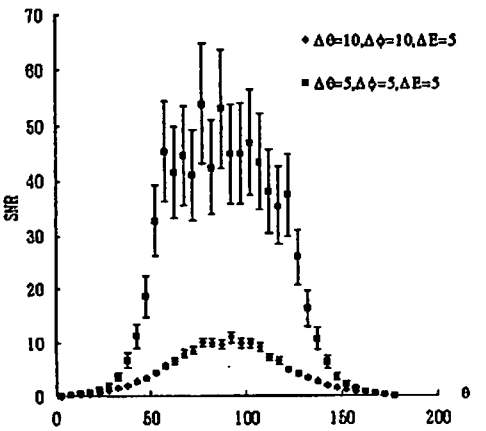

fig.9 SNR with θ-collimator,ϕ-collimator and energy window

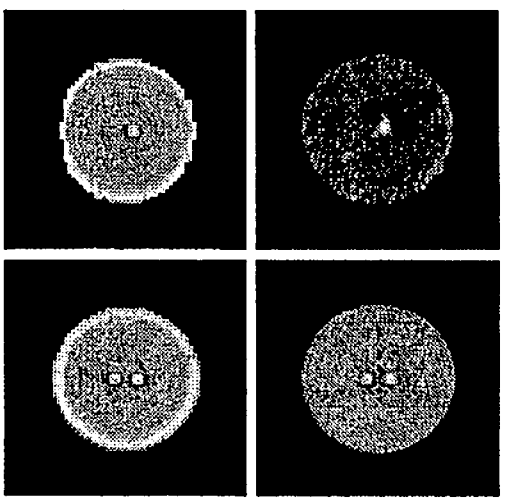

fig.10 Images of Compton scatter tomography (left) and transmission X-ray CT (right)

CALCULATION OF TLD RESPONSE USING EGS4 CODE

A.NUNOKO, K.ODA, H.MIYAKE

Department of Nuclear Engineering, Kobe University of Mercantile Marine

5-1-1 Fukaeminamimachi, Higasinada-ku, Kobe 658, Japan

and

S.Baba

Production Engineering Laboratory, Matsushita Electric Industrial Co., Ltd.

Inazu-cho, Toyonaka, Osaka 560, Japan

1. Introduction

Five years have passed since the present dosimetric system was put in force for radiation protection, where unique operational quantities such as "1-cm dose-equivalent" were introduced in spite of ambiguous definitions. Not only the unit conversion but also the adjustment of the energy dependence were then imposed on prevailing personal radiation monitors.

A design of personal dosimeters with a proper energy dependence, in general, has been carried out mainly by a filtering technique, and their responses are checked experimentally at discrete energiesy using several radiation sources. However, a theoretical approach is indispensable to evaluate the response in a wide energy range. It is more important to develop some technique for controlling the sensitivity in order to deal with any future change of the rem-response curve following 1990 ICRP recommendation.[1]

In this report the energy dependence of a thermoluminescence dosimeter (TLD) response has been calculated using EGS4 Monte Carlo code.[2] Our interest is directed to a control of TLD response by a choice of surrounding materials and their thickness.

2. Calculation of TLD Response

It is the purpose in this section to determine an appropriate geometry and other parameters for TLD response calculations using EGS4 code. As an example of comparison was selected a TLD badge system commercially obtainable (Matsushita, an element VD-808P with a hanger VD-807P), because its response was already examined experimentally. Figure 1 shows a cross-sectional view of this TL badge. We simplified the geometry in

EGS4 calculation as shown in Fig.2, where it consists of ABS resin (a hanger and a holder : total 11.4 mm), polyimide (a substrate for TL device : 11 mg/cm^2), $Li_2Bi_4O_7$ (TL : 15 mg/cm^2), air (a gap : 0.89 mm), Teflon (a cover : 28 mg/cm^2) and ABS resin (a holder : 3 mm). these layers are assumed as cylinders of 10 mm in diameter except 5 mm for TLD layer. The fluence of normally incident photons is 10^8(cm^{-2})

In the next step, the absorbed energy in TL layer was calculated for various radii of the field of incident photon beam in order to determine a suitable radius for saving the computing time. The results are summarized in Fig.3, where the ordinate is the energy deposited in TL layer per unit absorbed dose in air (J/Gy). It is shown in Fig.3 that the absorbed energy increases with the photon beam radius due to contribution of scattered photons for respective incident energies. We concluded from its saturation characteristics that the beam radius should be fixed to be 4.5 mm in further calculations.

The dependence of the energy deposition in TL layer upon the incident photon energy was calculated under the above-mentioned conditions. the result is shown in Fig.4 as dots and a line, together with the experimental values as circles, where the ordinate is normalized by the response at an energy of 662 keV. A good agreement of both results implies that it is possible to evaluate correctly a TLD response using Monte Carlo calculation on the model described above.

3. Control of Response Curve

Several types of TL materials are in practical applications such as $CaSO_4$, $Li_2B_4O_7$ and LiF and so on. When an air kerma or 1-cm dose-equivalent is evaluated with them, the energy dependence of the response is importantly influenced by a characteristic of themselves or of surrounding materials, for instance, a holder and a filter. The material surrounding TLD layer, in general, has two different roles of an attenuater for photons and a supplier of secondary electrons. Hence it is indispensable for response control to select suitable material and its thickness with reference to the cavity chamber theory. As an example, we tried to control the response of $CaSO_4$-TLD especially in a relatively high energy region.

It is well known that $CaSO_4$-type TLD is one of most sensitive elements and shows an extremely high sensitivity for low-energy photons because of high effective atomic number. Therefore, this type of TLD is always used with inserting a lead filter into a holder in order to attenuate low-energy photons. However, it is also confirmed from the experiment with a geometry shown in Fig.3 that the response at 1250 keV is approximately 80 % of that at 662 keV. It is the purpose in this section to clarify the reason of the response drop and to propose an improvement technique.

According to the cavity chamber theory, the ratio of the absorbed dose in an element

to that in air is the ratio of the mass energy-absorption coefficients if the thickness of the element is sufficiently large compared to the range of secondary electrons. On the contrary, if the element is sufficiently thin, the absorbed dose can be decided by the ratio of average mass stopping power of secondary electron. In the case of 662- and 1250-keV photons, the response difference should be within only 1 %; which implies there exists another reason.

In the present geometry shown in Fig.5 was inserted a Pb filter with a thickness of 0.7 mm on ABS resin of about 80 mg/cm^2 in order to attenuate low-energy photons. The thickness of ABS resin layer corresponds to the range of electrons with an energy of 300 keV. Hence, it is considered that the Pb filter may influence largely on characteristics of electron-supply to TLD layer for such higher energy photons.

It was confirmed from calculations with a simplified geometry that the relative contribution of the secondary electrons emitted in the Pb layer to the absorbed energy in $CaSO_4$ amounts to about 20 % and 50 % for 662 and 1250 keV, respectively. The fact shows that the Pb layer, attenuater for lower-energy photons, would modify the secondary electron spectrum for higher-energy photons, and it should be replaced by any other air-equivalent material.

Figure 6 shows the absorbed energy in $CaSO_4$ layer for various thickness of ABS resin surrounding $CaSO_4$ TLD which plays an important role as a secondary-electron supplier. It is found that about 300 mg/cm^2 layer of ABS resin should be required for achieving the response ratio near the unity, and that the Pb filter should be put in outer position.

Finally in Fig.7 is shown the result of rsemodeling of the TLD system, which consists of $CaSO_4$ TLD, ABS resin of 300 mg/cm^2 as an electron supplier and Sn layer for filtering of lower-energy photons. Four curves represent tshe energy dependencies of TLD response for different thicknesses of the Sn filter. The thickness of 0.5 mm is the best choice in this case, where an error is within 15 % between 75 and 1250 keV.

4. Summary

In this report, we applied EGS4 Monte Carlo simulation code to evaluation of the response of personal dosimeter system. It was confirmed that the results obtained with suitable geometry would agree satisfactorily with the experimental ones for a TLD commercially available.

In the next step, we tried to improve the response of $CaSO_4$ TLD for higher energy photons. It was found that Pb layer for attenuation of lower-energy photons would influence a secondary electron spectrum in the present geometry. We pointed out that the Pb layer should be replaced by a sufficiently thick air-equivalent material which would play a role of a electron supplier.

Further applications to other types of personal dosimeters are now in progress.

References

[1] ICRP Publication 60. *1990 Recommendations of the International Commission on Radiological Protection*, Annals of the ICRP21(1-3) (1991).

[2] W.R.Nelson, Hirayama and D.W.O.rogers, *EGS4 Code System*, SLAC-265 (1985).

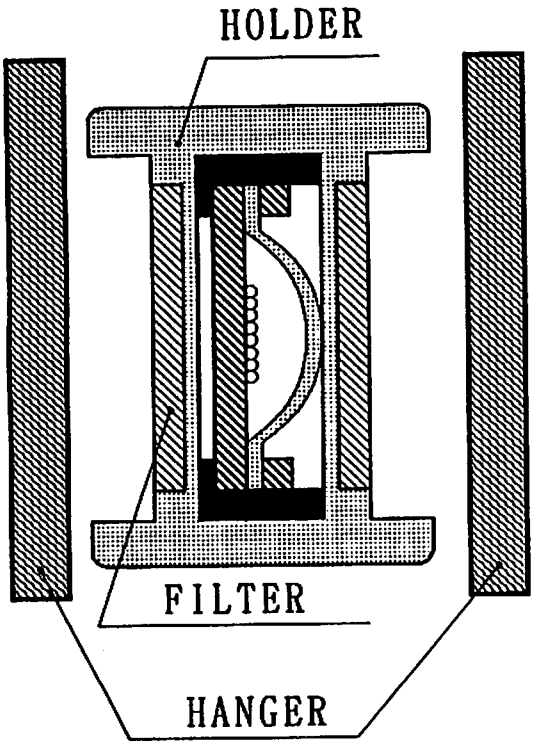

Fig.1 Cross–sectional view of TLD badge system.

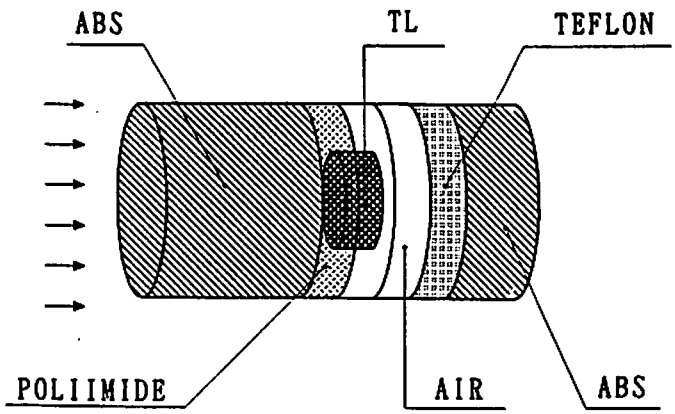

Fig.2 Simplified geometry of TLD used in EGS4 calculation.

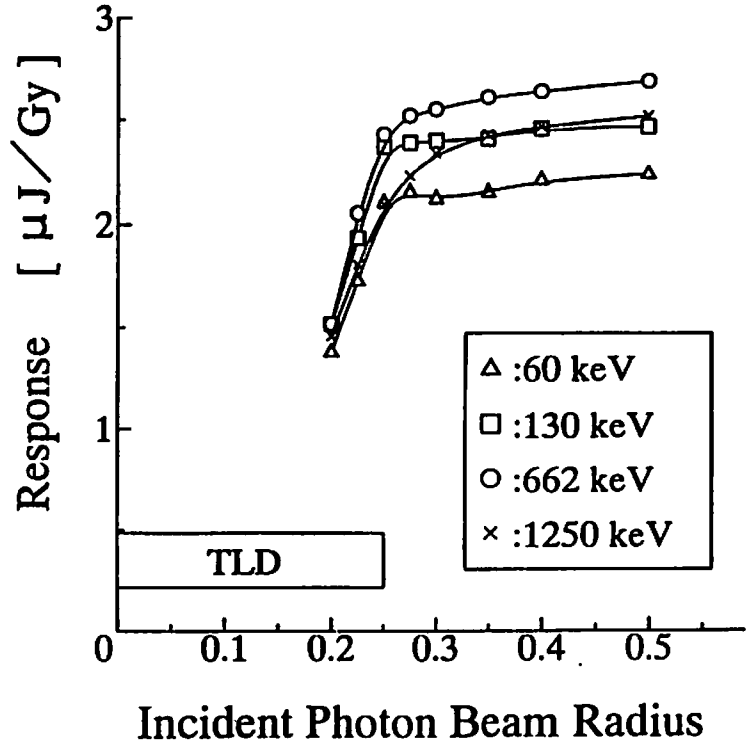

Fig.3 Variation of the energy deposited in TLD with the photon beam radius.

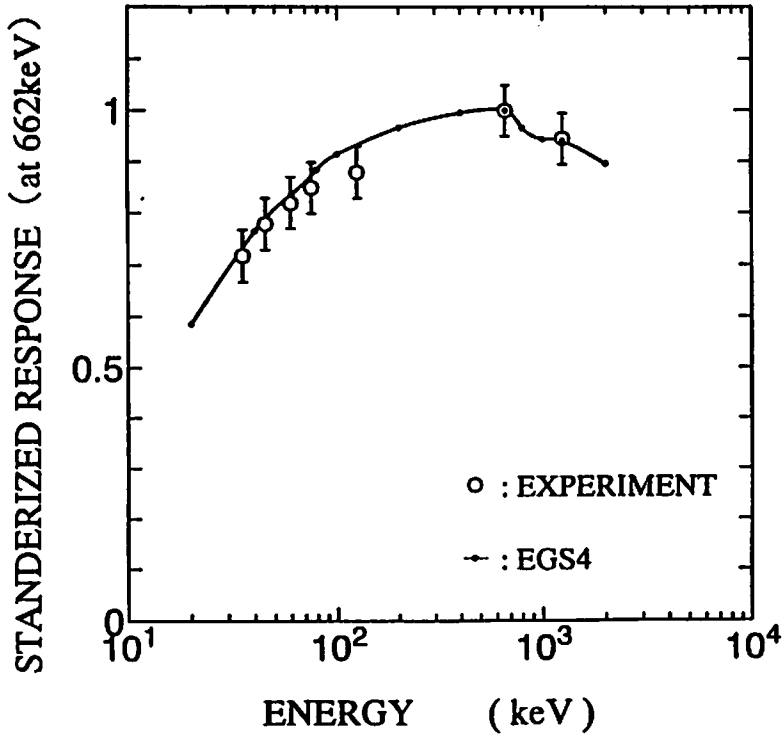

Fig.4 Dependence of TLD response on the photon energy.

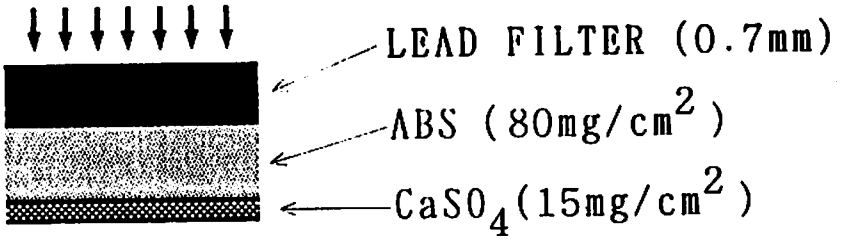

Fig.5 Geometry of CaSO4 TLD system.

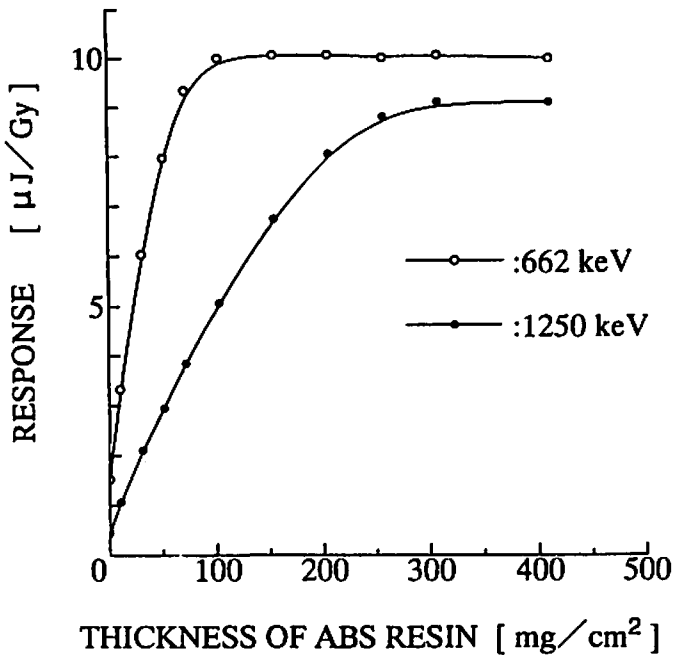

Fig.6 Dependence of TLD response on the thicknees of ABS filter.

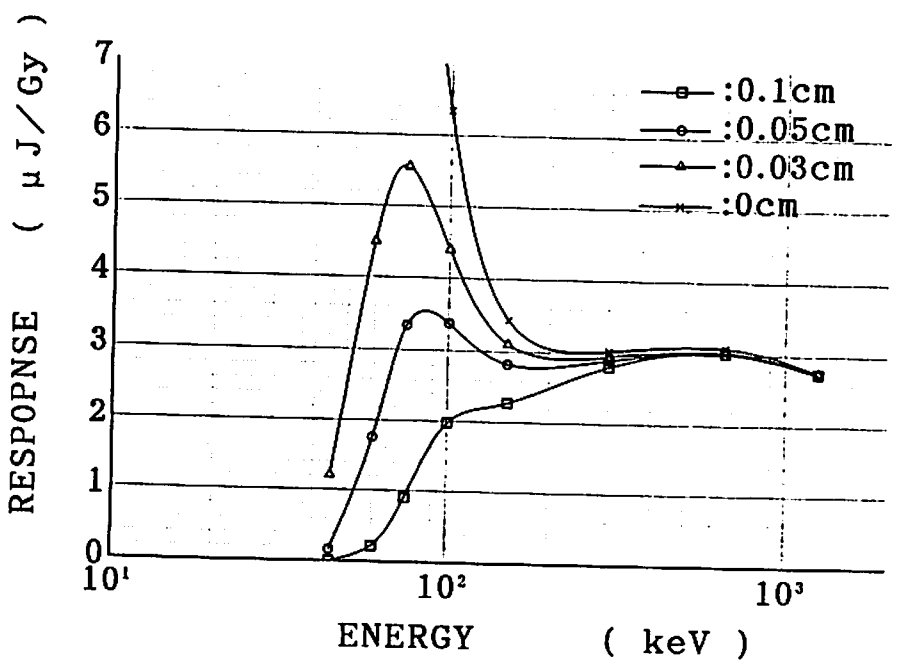

Fig.7 Response curve for improved TLD system.

APPLICATION OF A GENERAL PURPOSE USER'S VERSION OF THE EGS4 CODE SYSTEM TO A PHOTON SKYSHINE BENCHMARKING CALCULATION

I. NOJIRI, Y. FUKASAKU, O. NARITA

Power Reactor and Nuclear Fuel Development Corporation
Tokai-mura, Naka-gun, Ibaraki 319-11, Japan

Abstract

A general purpose user's version of the EGS4 code system has been developed to make EGS4 easily applicable to the safety analysis of nuclear fuel cycle facilities. One such application involves the determination of skyshine dose for a variety of photon sources. To verify the accuracy of the code, it was benchmarked with Kansas State University (KSU) photon skyshine experiment of 1977. The results of the simulation showed that this version of EGS4 would be appicable to the skyshine calculation.

1. Introduction

A general purpose user's version of the EGS4 code system has been developed to make EGS4 [1] easily applicable to the safety analysis of nuclear fuel cycle facilities. By using this version, without requiring user-written subroutines for geometrical modeling, sources, detectors, and variance reduction, electron - photon transport could be simulated [2] . One such application involves the determination of skyshine dose for a variety of photon sources.

To validate this version of the EGS4 for photon skyshine applications, the code was benchmarked with the Kansas State University (KSU) photon skyshine experiment [3] of 1977. A synopsis of the KSU skyshine experiment is given in sec. 2, followed by a description of the numerical simulation. Finally, the results of the simulation are compared with the benchmark experimental data.

2. The Kansas State University Skyshine Experiment

The KSU experiment , sponsored by the Japanese Nuclear Safety Research Association, was designed and carried out jointly by reseachers from Radiation Research Associates and KSU and was performed at the KSU Nuclear Engineering Shielding Facility from May through November 1977.

To obtain a sufficiently intense skyshine radiation field over large distances, three ^{60}Co sources (essentially point sources) with nominal activities of 10.3, 229, and 3800 Ci were

used. The sources were placed at 1.98m above grade on the axis of an annular concrete silo with sufficiently thick walls so that radiation penetrating horizontally outward was negligible. Photon emmision form the sources was collimated into a 150.0 deg upwardly directed conical beam. a cross-sectional view of the silo walls parallel to the silo axis is shown in Fig. 1.

Both energy spectra and exposure rate measurements were made of the skyshine radiation field over a 700-m baseline, radially outward from the source. Measurements were made for three distinct source configuration; first, without a roof shield, and then with 21.0- and 42.8-cm-thick concrete roof shield. All of the exposure rate measurements were made at 1.0 m above grade using a spherical high-pressure ionization chamber . The net skyshine measurements were reported in μR/h and were then normalized to the source activity in curies.

3. Analytical Method

The silo and the air volume were modeled as a cylindrical shell sitting on a ground plane. Shown in Fig. 2 is a cross sectional view of the whole geometry used in the simulation.

Material Composition used the same data of MCNP benchmarking of this experiment by Los Alamos National Laboratory [4] , shown in Table 1.

The conical source option was applied to simulate the collimated photon emmision. The source spectrum was used simplified ^{60}Co line spectrum. To compare some detectors of this code, several simulations were performed for each detector. Point detectors, surface crossing detectors, and next event surface crossing detectors were located at a number of distances from the source. Shown in Fig. 3 is a cross-sectional view of the detector location.

The photon flux was calculated and then multiplied by the dose conversion factor [5] to determine the normalized exposure rate, which allowed direct comparison with the experimental data.

4. Results and Discussion

The number of history is 500,000 in every calculation. The results of the EGS4 skyshine exposure calculations are shown in Fig. 4, Fig. 5, and Fig. 6, where they also compared with experimental data. There are almost no differences between detectors. However, the EGS4 calculation is shown to overestimate the actual skyshine exposure rate. As indicated in the MCNP benchmarking, It is considered that use of the line spectrum and simplified silo model lead to this result. Hence, the good agreement would be obtained when the actual source spectrum and the detailed modeling of the silo are used.

References

[1] W. R. Nelson et al., *The EGS4 Code System*, SLAC-report 265 (1985).

[2] T. Momose et al., *The Development of a General Purpose User's Version of the EGS4 Code System*, KEK Proceedings 91-14, p.48-73 (1991).

[3] R. R. Nelson et al., *A Benchmark Gamma-Ray Skyshine Experiment*, Nucl. Sci. Eng., **79**, 404 (1981).

[4] R. H. Olsher et al., *Benchmarking the MCNP Monte Carlo Code with a Photon Skyshine Experiment*, Nucl. Sci. Eng., **114**, 219 (1993).

[5] ICRP Pub. 51 *Data for Use in Protection against External Radiation.*

Table.1. EGS4 Calculation used mixture composition

Mixture	ρ (g/cc)	Element	wt%
Air	1.2900E-03	N	78.18
		O	20.97
		Ar	0.85
Soil	1.71	H	0.36
		C	1.47
		O	49.59
		Na	0.84
		Mg	1.60
		Al	7.08
		Si	27.09
		P	0.06
		S	0.22
		K	2.37
		Ca	4.21
		Ti	0.34
		Fe	4.04
Concrete	2.17	H	0.56
		O	49.83
		Na	1.71
		Mg	0.24
		Si	31.58
		S	0.12
		K	1.92
		Ca	8.26
		Fe	5.78

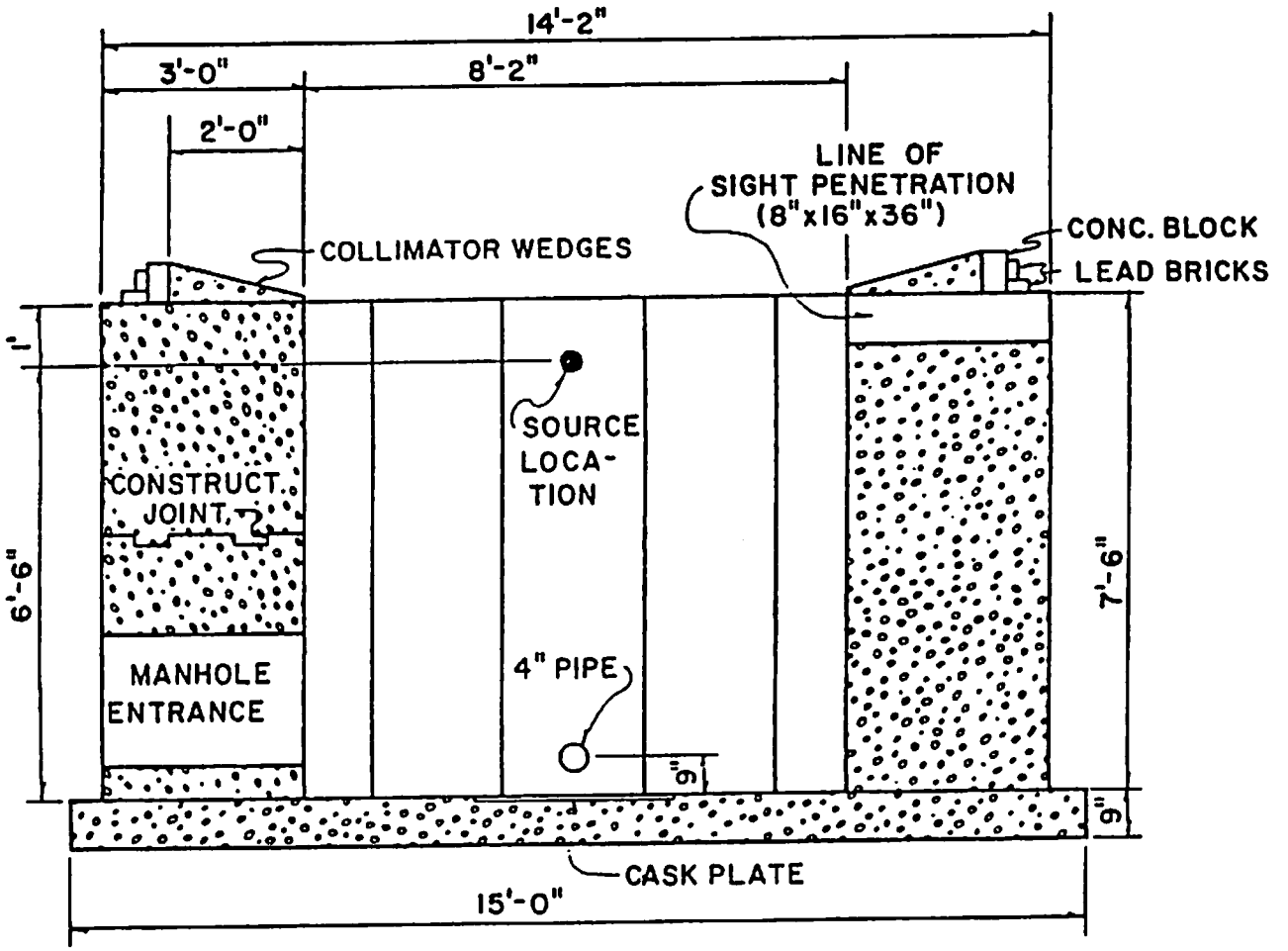

Fig. 1. Cross-sectional view of the silo walls parallel to the silo axis.

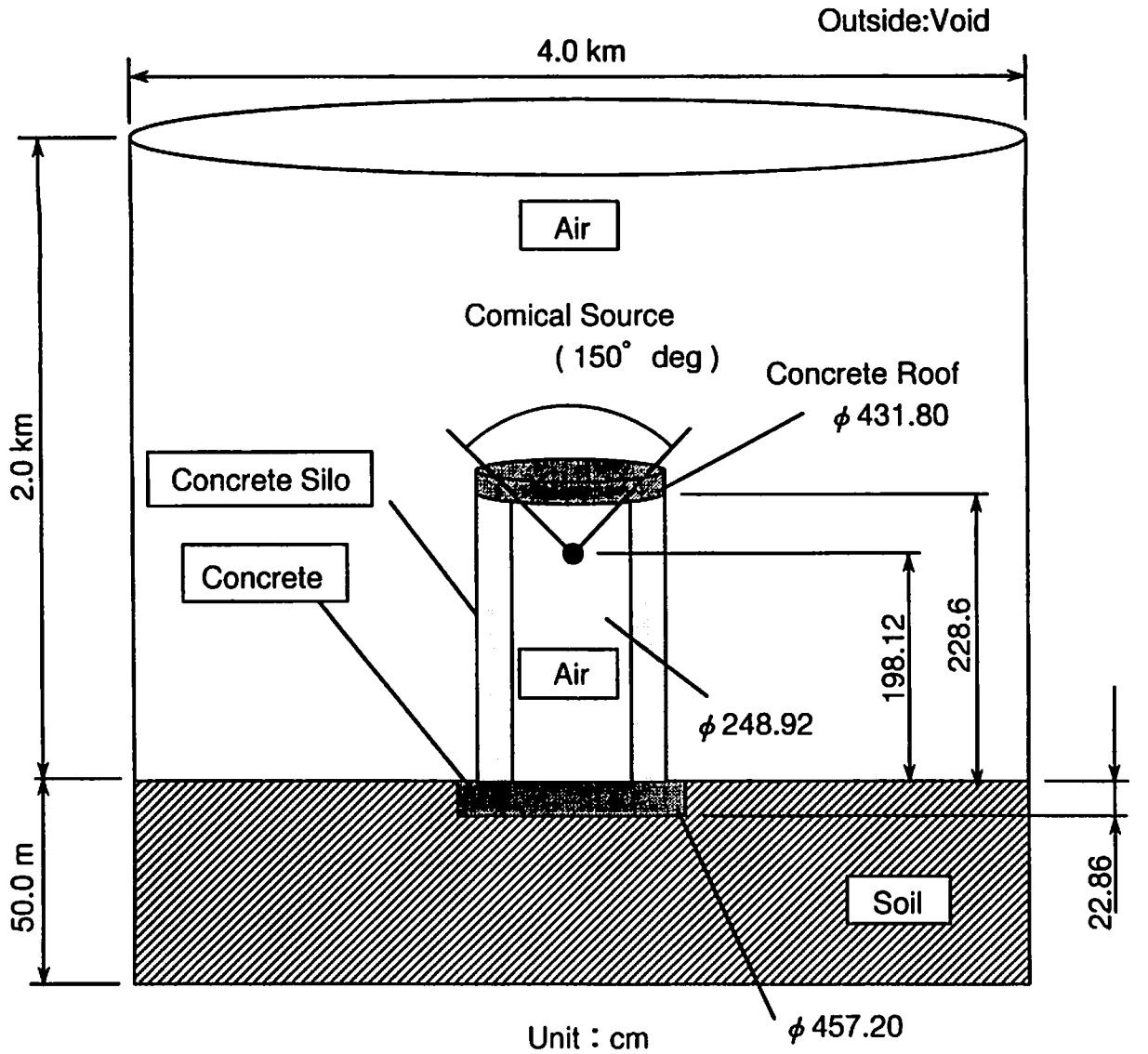

Fig.2. Skyshine Exposure Rates Calclated Model

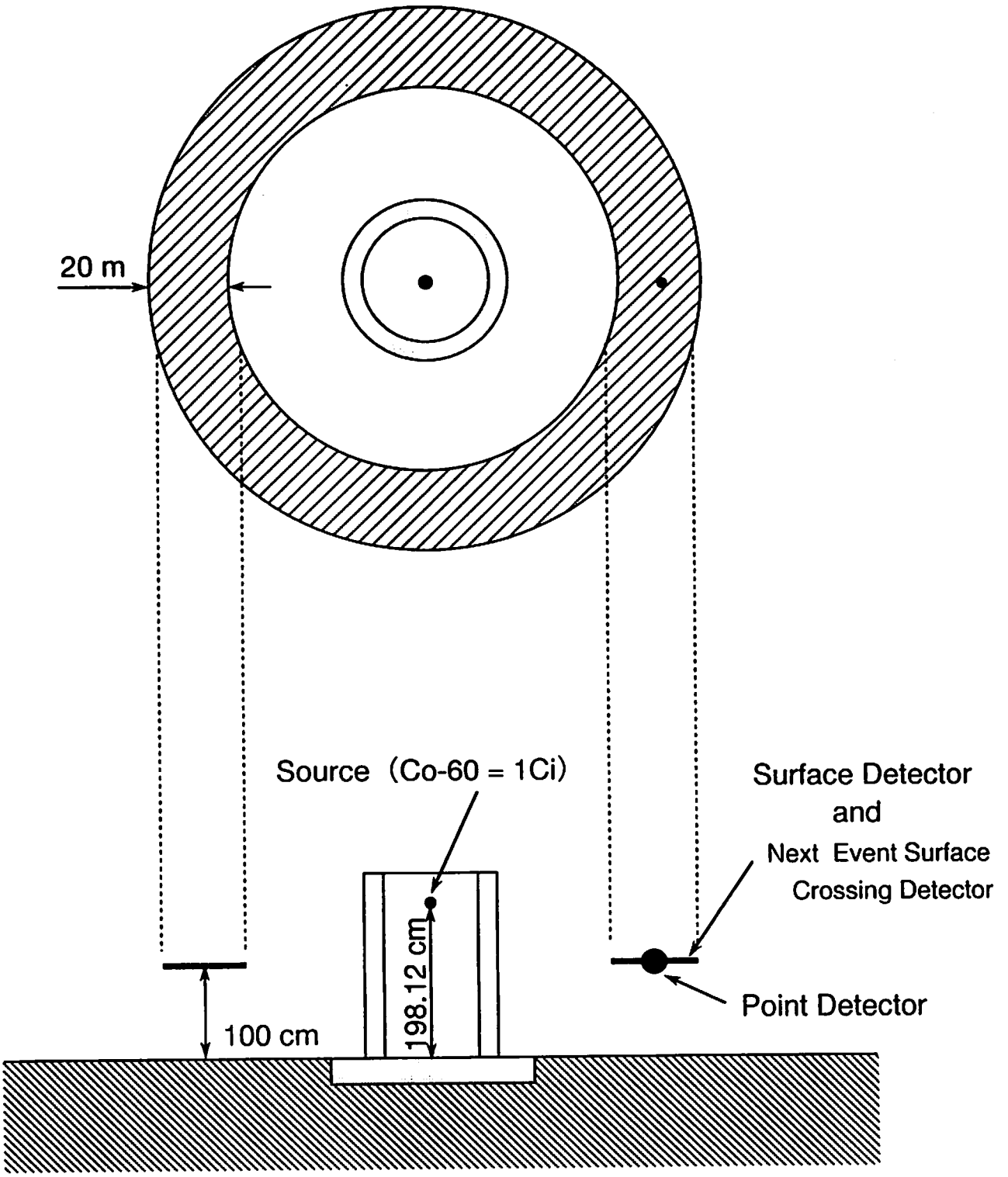

Fig.3. Skyshine Exposure Rates Caluculated Detector Model

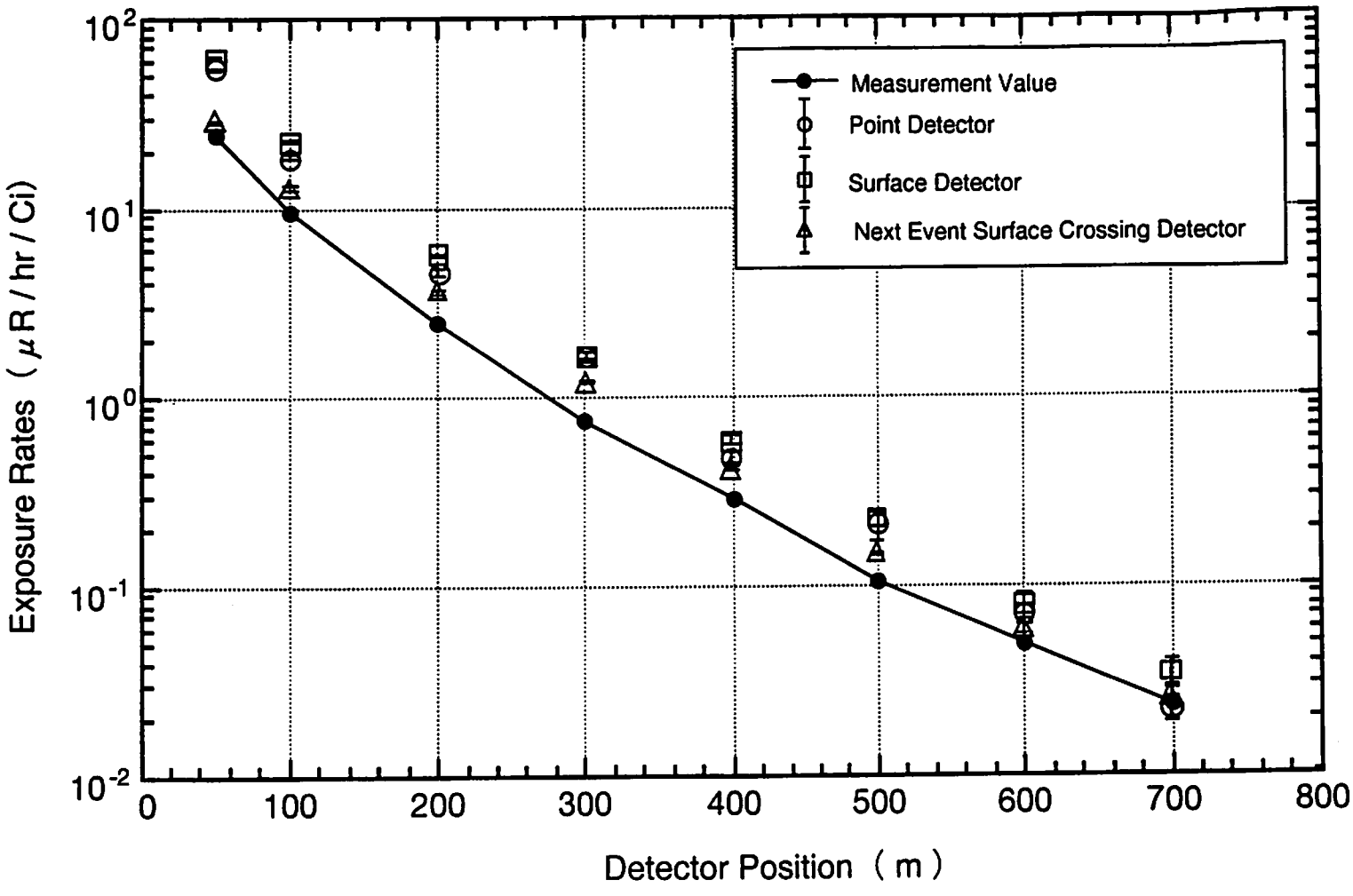

Fig.4. Comparison Measured and Calculated Skyshine Exposure Rates for the UNSHIELDED Case

Number of History : 500,000

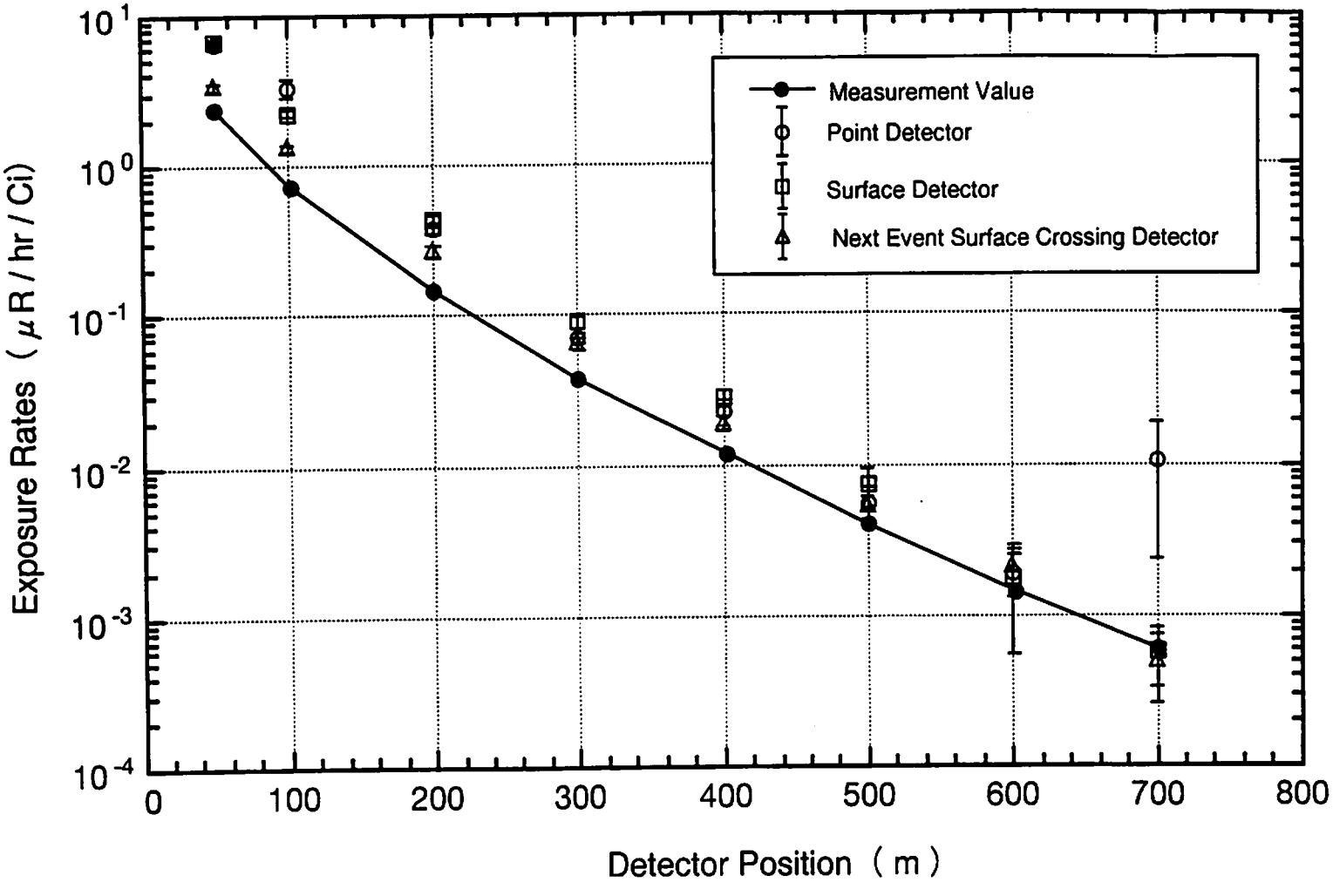

Fig.5. Comparison Measured and Calculated Skyshine Exposure Rates for the 21.0cm SHIELDED Case

Number of History : 500,000

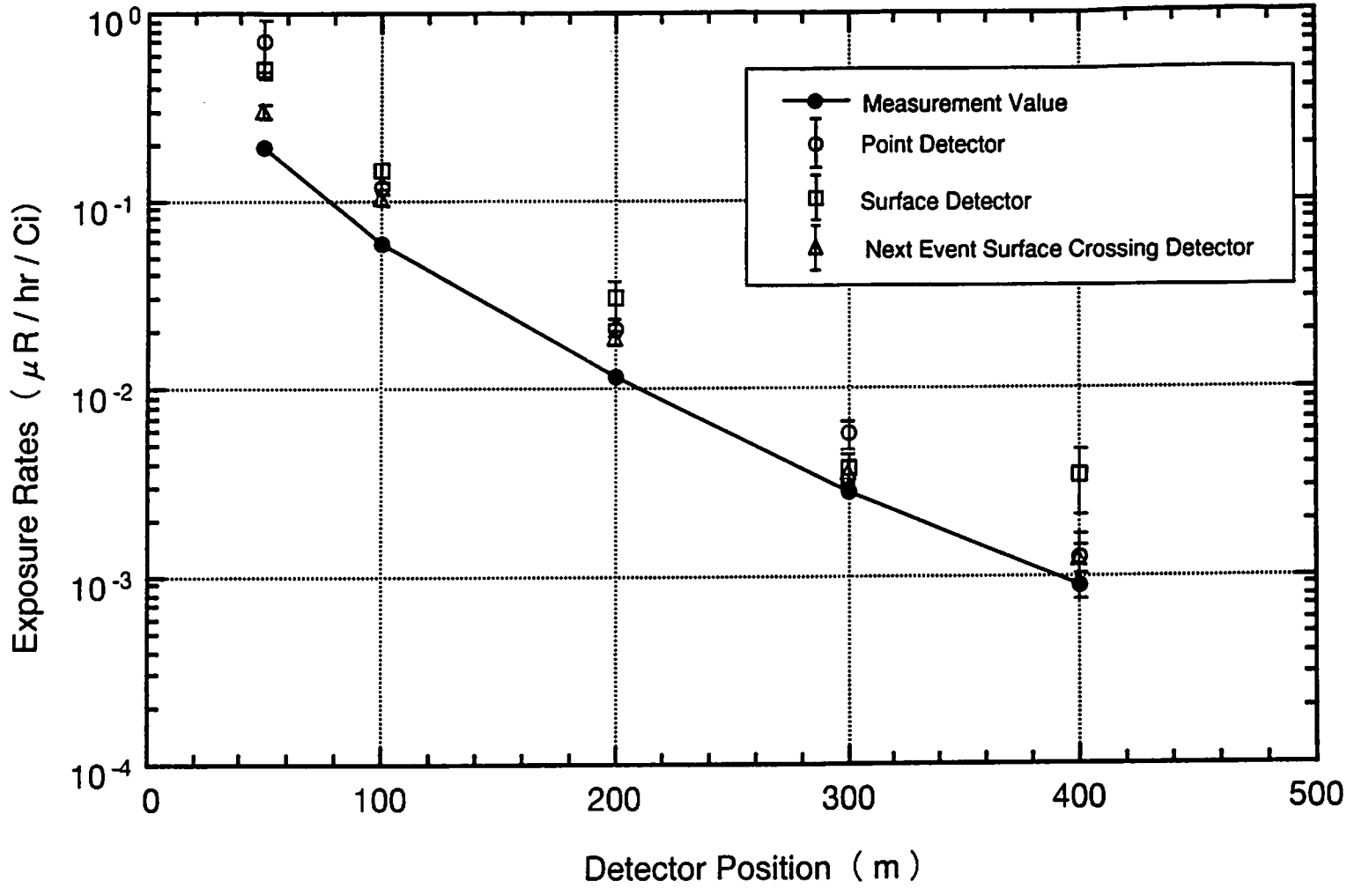

Fig.6. Comparison Measured and Calculated Skyshine Exposure Rates for the 42.8cm SHIELDED Case

Number of History : 500,000

CALCULATION OF RESPONSES OF A NaI(Tl) DETECTOR TO THE ENVIRONMENTAL GAMMA-RADIATIONS

H. FUKUDA , S. IWASAKI and M. KITAMURA

Department of Nuclear Engineering

Tohoku University

Aramaki-Aza-Aoba, Aobaku, Sendai 980-77, Japan

Abstract

Spectrum responses of a 3"ϕ×3"long NaI(Tl) detector to the environmental gamma-rays were simulated by EGS4 code for the purpose of the environmental gamma monitoring using the neural network technique. To obtain the responses within a reasonable calculation time we have adopted a simplified configuration model in the geometry and source distribution in the preliminary stage of the study; whereas the effects of the scattering and attenuation of gamma radiations were approximately simulated in this geometry. Some discrepancies were found in the simulated spectra. This implies that more detailed modeling should be made in the geometry and source distribution.

1. Introduction

In the monitoring for the environmental gamma-radiations for nuclear facilities, the gamma dose rate is usually watched[1]. The exposure-dose rate is obtained from signals of a NaI(Tl) detector of monitoring system with the correction for the energy dependency of the gamma-dose by the DBM method[1,2]. In a few cases, the spectrum data are used to quantify natural radiation sources by a simple unfolding method, whereby the artificial components can be identified in the off-line process base[2]. Such conventional type analysis takes a certain time, and, therefore, the development of a quick but detailed analysis technique is required for the public safety management.

A new spectrum monitoring technique based on an extended version of the linear associative neural network[3,4,5], 'orthogonal projection neural network', has been proposed by the present authors[6,7,8]. The fundamental characteristics of the network proved to be feasible for the sensitive and quick detection of the anomaly in the environmental radiations.

The technique relies on the assumption that in the normal condition the objective pulse height spectra should be linear combinations of the referense pulse height spectra,

called responses, of each component nuclide. The preparation of the responses is, therefore, of prime importance in the neural network analysis. The responses should primarily be obtained by performing the measurements in the same source-detector configuration, geometry and electronics conditions with the actual monitoring. In the case of the environmental radiation monitoring, however, it is impossible to obtain the responses of naturally occurring radiation sources one by one by the measurements as described later. Thus, we have tried to obtain them by the simulation calculation using EGS4 code[9].

Environmental gamma-ray sources which we deal with are outlined in section 2. Assumptions in the actual Monte-Carlo calculation are described in section 3. The results of the calculations are discussed in section 4. Lastly the summary is given.

2. Environmental Gamma-rays

The environmental gamma-ray sources consists mainly of naturally occurring long-lived products, e.g., ^{40}K, the daughter nuclides of the thorium and uranium decay-chain series, and the components due to the cosmic rays. Besides these, artificial components may be added. The artificial ones are due to nuclear bomb tests, and release from nuclear facilities in normal operation or in abnormal one, i.e., accident. Among the daughter nuclides of the two decay chain series, ^{222}Rn (radon) and ^{220}Rn (thoron) are noble gases, and have high solubility in water. These elements diffuse easily from the underground into the atmosphere. The concentrations of these gases fluctuate regularly or irregularly due to the change of the weather conditions, such as temperature, pressure, precipitation and other factors. Such large fluctuations sometime obscure the weak artificial components. In the present simulation calculations, we have taken into account the seven gamma-emitters: ^{214}Pb and ^{214}Bi in the uranium series; ^{228}Ac, ^{212}Bi, ^{212}Pb and ^{208}Tl in the thorium series; and ^{40}K. Totally 40 gamma-rays emitted from these nuclides were considered as listed in Table 1. The data of the emission probabilities of the gamma-rays were taken from the reference[10]. The cosmic-ray component was neglected in the preliminary stage of the calculation.

Table 1. List of gamma-rays considered in the calculation with their emission probabilities.[10]

	Energy(MeV)	Emission Prob.
^{228}Ac	0.1291	0.0293
	0.2093	0.0455
	0.2702	0.0377
	0.3276	0.0336
	0.3383	0.1201
	0.4095	0.0223
	0.4630	0.0464
	0.7947	0.0484
	0.9111	0.2900
	0.9646	0.0545
	0.9691	0.1746
	1.5880	0.0312
	1.6304	0.0195
^{214}Bi	0.6093	0.4609
	0.7684	0.0489
	0.9341	0.0317
	1.1203	0.1504
	1.2381	0.0592
	1.3777	0.0402
	1.4080	0.0248
	1.5093	0.0219
	1.7296	0.0305
	1.7645	0.1592
	2.2042	0.0499

	Energy(MeV)	Emission Prob.
^{212}Bi	0.7272	0.1180
	0.7854	0.0200
	1.6206	0.0275
^{214}Pb	0.2419	0.0747
	0.2952	0.1920
	0.3519	0.3710
	0.7859	0.0109
^{212}Pb	0.2386	0.4310
	0.3001	0.0330
^{208}Tl	0.2774	0.0650
	0.5108	0.2250
	0.5831	0.8600
	0.7631	0.0170
	0.8604	0.1200
	2.6147	1.0000
^{40}K	1.4608	1.0000

3. Calculational Geometry

In the environmental radiation monitoring, the gamma detection system (a temperature controlled NaI(Tl) scintillation detector in its housing) is usually located in the area outside of nuclear facility on the ground or the facility building.

The source nuclides distribute almost everywhere in the environment of the detector: the ground, atmosphere, floor, wall and ceiling of building, surrounding materials and detector itself, etc. The gamma-rays emitted from the source nuclides enter the detector directly after surviving from absorptions or after energy degrading due to scattering in these materials. These scattered radiations appreciably build up mainly in the lower energy region of the pulse height spectra and worsen the sharpness of the photopeaks of the direct components. The shape of the responses is highly sensitive to the geometry and environmental conditions. In this situation, it is inherently impossible to measure the responses to each source distributed in a given environment by the measurement. The calculational method of the responses should be validated by comparing the results to the observed data. In the present study, we measured the spectra with a 3"$\phi\times$ 3"long NaI(Tl) detector system in a room of the Radioisotope Laboratory at Department of Nuclear Engineering, Tohoku University.

The geometrical modeling in the calculation is very important from the above mentioned reason. It is, however, very difficult to simulate the actual room detector geometry in detail, because the quite low efficiency of the Monte-Carlo calculation. In the primary stage of the present study, we tested a simple geometry, whereas the scattering and attenuation effects of gamma-rays would be taken into account.

We adopted the following geometry with the three assumptions on the sources: a NaI(Tl) detector of cylindrical shape enclosed by concrete wall of cylindrical shape, which locates in relatively near position to the detector as shown in Fig. 1. The gap between the detector and wall is filled with dry air of 1 atom at room temperature. The assumptions are,

(1) the emission probability of each gamma source is isotropic;

(2) the nuclides ^{40}K are in the detector and wall uniformly with the same concentration;

(3) the other nuclides also distribute uniformly in the atmosphere and wall with the same concentration.

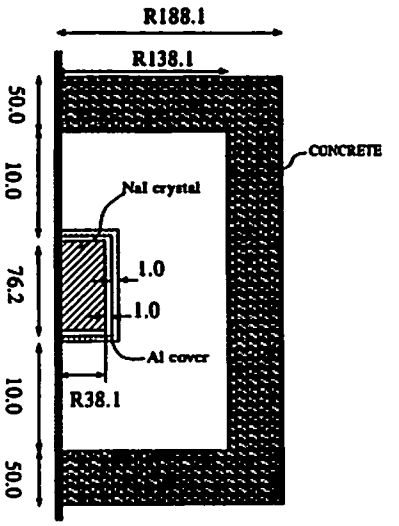

Fig. 1. Geometry of the Monte-Carlo calculation.

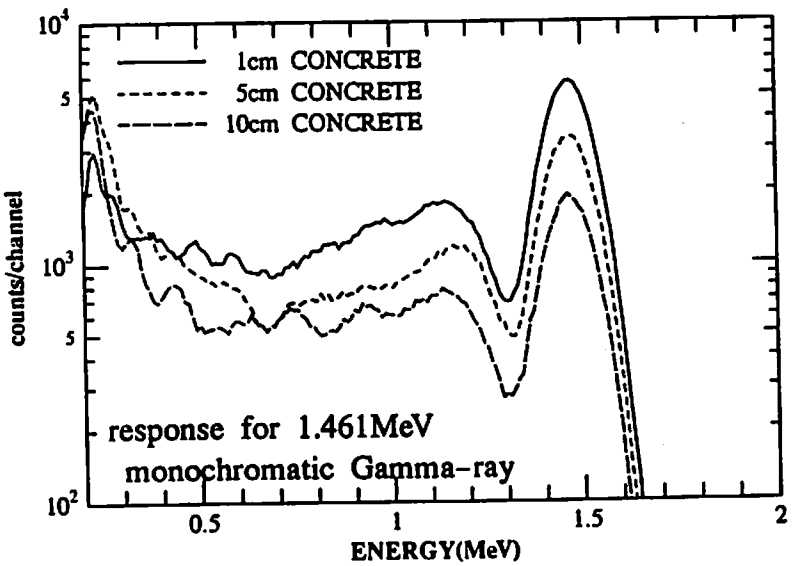

Fig. 2. Responses of the ^{40}K gamma-rays for the wall of the thicknesses of 1cm, 5cm and 10cm, respectively.

4. Results and Discussion

The elemental composition of the concrete wall is H(0.169 w%), C(0.001 w%), O(0.564 w%), Na(0.0117 w%), Al(0.0226 w%), Si(0.204 w%), Ca(0.0240 w%) and Fe(0.004 w%). The thickness of the concrete wall is the important parameter in the calculation. Fig. 2 shows the variation of the shape of the spectrum for the ^{40}Ks' gamma (1.461-MeV

monochromatic gamma-source) in the test calculations for the wall of three thicknesses of 1cm, 5cm and 10cm, respectively. The spectrum shape in the latter two cases are clearly affected by the scattering and attenuation processes. Tentatively we took the wall thickness as 5cm by compromise between the amount of scattering/absorption effects and CPU time. We employed no variance reduction technique.

Representative response spectra for each element are shown in Fig. 3. We validated the calculation method by testing how the responses reproduce the measured total spectrum well using the linear associative neural network. Figure 4 shows an example of the composed spectrum (i.e., a projected spectrum from the network parallel to the subspace spanned by the above calculated response vectors, see ref. 8) compared to the measured one. We can see some significant discrepancies between them. There are several reasons of the disagreement mainly due to the incomplete modeling of the calculation, as follows:
(1) insufficient thickness of the wall; the thinner wall is responsible to the sharpness of the peaks in the spectra.
(2) the same concentration assumption of the daughters of radon and thoron in the wall and atmosphere; the components in the atmosphere are also responsible to the more sharpness of the peaks in the spectra than the observed one.
(3) neglecting the cosmic-ray contributions; the cosmic-rays can also degrade the spectrum shape, particularly, in the lower energy region.
(4) disregarding the contribution of the beta-rays from ^{214}Bi which could affect the spectrum by the Bremsstrahlung process.
(5) insufficient modeling of the geometry; the other small surrounding materials, such as lead bricks, desk, etc. were not included.

In spite of the above mentioned discrepancies we can conclude that the present calculation generally reproduced the trend of the measured data as the simple modeling, and is acceptable.

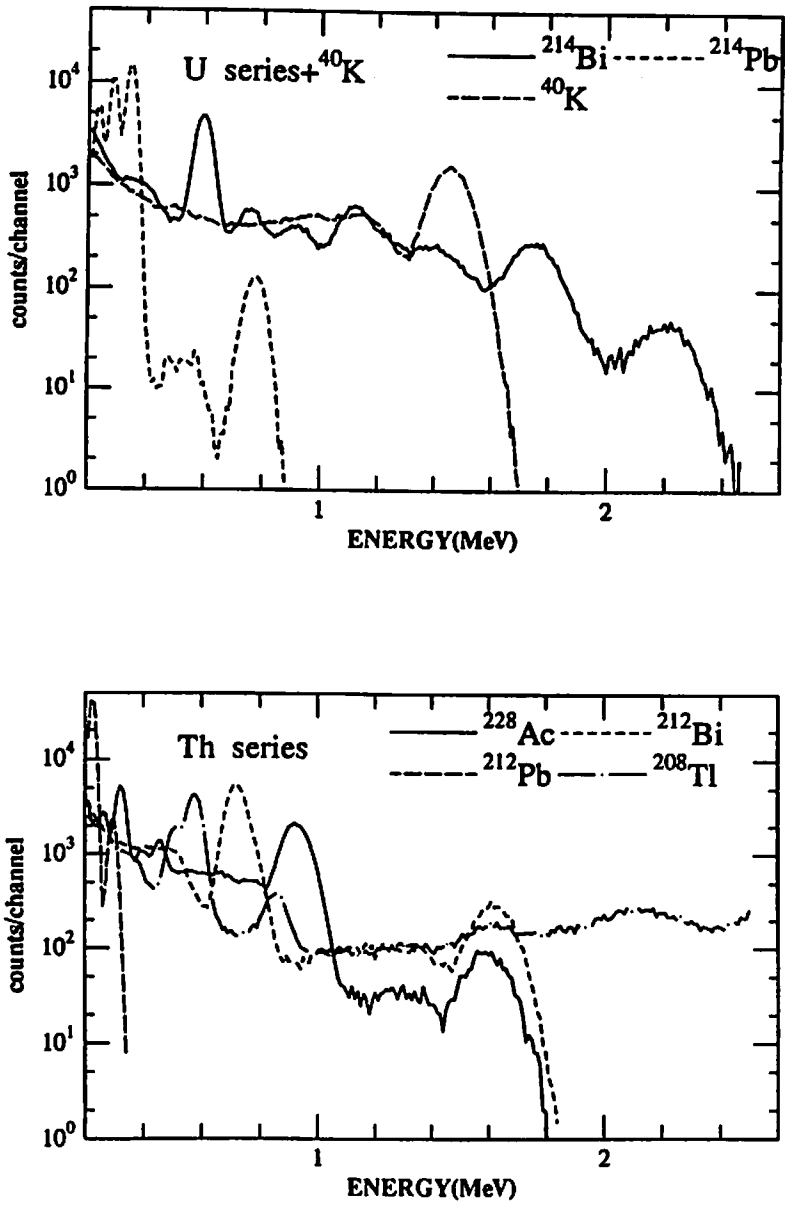

Fig. 3. Responses of the ^{40}K, ^{214}Bi, ^{214}Pb (upper); ^{228}Ac, ^{212}Bi, ^{212}Pb, and ^{208}Tl gamma-rays (lower), respectively.

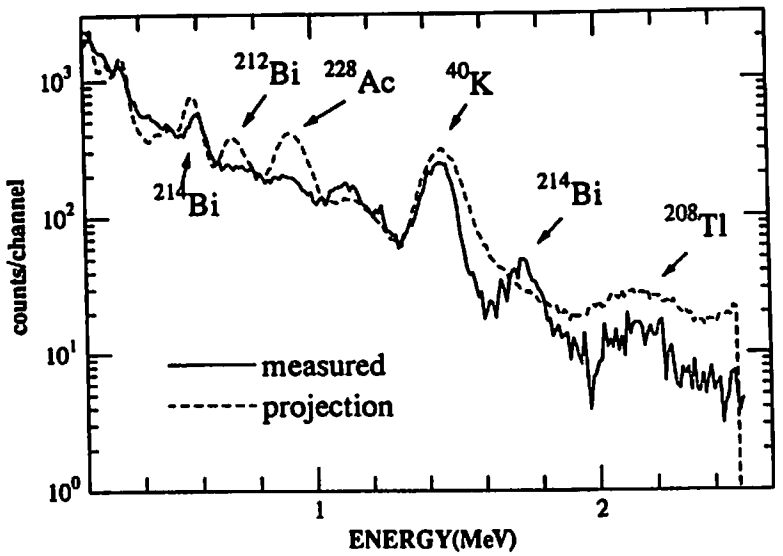

Fig. 4. An example of the composed environmental gamma-ray spectrum compared to the measured one.

5. Summary

We have calculated the spectrum responses of a NaI(Tl) detector to the environmental gamma-radiations as the referense spectra for the neural network using the EGS4 code. The comparison between the measured spectrum and composed spectrum from the responses showed appreciable disagreement. This may due to the too simplified geometry and source model in the calculation as pointed out above. Present results, however, showed a promise to obtain enough reliable data for the purpose of the neural network analysis of the environmental radiation spectra by improving the calculational model.

Acknowledgements

The authors express deep appreciation to Dr. HIRAYAMA Hideo, KEK, and people of Laboratory of Radiation Control, CYRIC Tohoku University, for use of the EGS4 code.

References

[1] N. Yamagata (Ed.), *Kankyou Houshasen Handbook* (Handbook of Environmental Radiation), Informatin Center Press (1985) (in Jap.).

[2] E. Nakamura, *Telemeter Systems for Monitoring External Radiation around Onagawa Nuclear Power Plant*, J. At. Energy Soc. Japan, **25**, 179 (1983) (in Jap.).

[3] S. Iwasaki, H. Fukuda, and M. Kitamura, *Application of Linear Associative Neural Network to NaI(Tl) Gamma-Ray Spectrum Analysis*, Proc. of 7th Workshop on Radiation Detectors and Their Uses, Jan. 26-27, 1993, KEK, Tsukuba KEK Proceedings 93-9 June 1993 H/R.

[4] H. Fukuda, S. Iwasaki, and M. Kitamura, *Application of Neural Network to Gamma-Spectrum Analysis I NaI(Tl) Spectrum Analysis by Linear Associative Network*, Proc. 1993 Ann. Meet. AESJ (in Jap.).

[5] S. Iwasaki, H. Fukuda,and M. Kitamura, *Training Strategy of Linear Associative Network as a Basic Tool for Gamma-ray Spectroscopy*, Proc. Artificial Neural Networks in Eng. (ANNIE '93), Nov, 14-17, 1993. St.Louis, Missouri, USA, pp. 199-207. ASME, New York (1993).

[6] H. Fukuda, S. Iwasaki, and M. Kitamura, *Application of Neural Network to Gamma-Spectrum Analysis II Abnormal Detection by Projection Network*, Proc. 1993 Fall Meet. AESJ, p360 (in Jap.).

[7] H. Fukuda, S. Iwasaki, and M. Kitamura, *Application of Neural Network to Gamma-Spectrum Analysis IV Environmental Gamma-Ray Monitoring*, Proc. 1994 Ann. Meet. AESJ, p585 (in Jap.).

[8] H. Fukuda, S. Iwasaki, and M. Kitamura, *Application of Projection Neural Network to Monitoring for Environmental-Gamma-Radiation -A Simulation Study-*, Proc. of 8th Workshop on Radiation Detectors and Their Uses, Jan. 25-27, 1994, KEK, Tsukuba KEK Proceedings 94-7, August 1994 H/R.

[9] W.R. Nelson, H. Hirayama, and D.W.O. Rogers, *The EGS4 Code System*, SLAC-Report-265 (1985).

[10] G. Erdtman, and W. Soyka, *The Gamma Rays of the Radionuclides*, Verlag Chemie, Weinheim, New York (1979).

HIGH ENERGY GAMMA RAY RESPONSE OF LIQUID SCINTILLATOR

N. SHIGYO, K. ISHIBASHI, N. MATSUFUJI and T. NAKAMOTO
Department of Nuclear Engineering, Kyushu University
Hakozaki, Fukuoka-shii, 812, Japan

M. NUMAJIRI
National Laboratory for High Energy Physics
Oho, Tsukuba-shi, Ibaraki-ken, 305, Japan

Abstract

We made the experiment on the spallation reaction. NE213 organic liquid scintillators were used for measuring neutrons and g rays. To produce the γ ray emission cross section, we used the response functions by EGS4 code. The response functions look like uniform above γ ray energies of 60 MeV. The experimental data of the γ ray emission cross section are different from the data of High Energy Transport Code.

1. Introduction

The NE213 scintillator which is used in the measurement of high energy neutrons is sensitive to the γ ray. When a flight path is short in the time-of-flight (TOF) measurement of neutrons, it is important to discriminate between neutrons and γ rays. If the two types of particles can be separated clearly, the cross section of the γ ray emission will be obtained. In this work, we obtain the response function of γ rays by EGS4 code, to produce the cross section of the γ ray creation [1].

High Energy Transport Code (HETC) [2] is used to calculate the high energy transport phenomena. The emission of the γ ray is considered in the some version of HETC. However, such code considers only γ rays from the residual nuclei after the spallation reaction. If γ rays from the spallation reaction are obtained, information on the other processes may be found.

2. Experiment on Spallation Reaction

We made the experiment on the spallation reaction at p2 beam line of 12 GeV proton synchrotron accelerator at National Laboratory for High Energy Physics (KEK). The incident proton energies were 0.8, 1.5, 3.0 GeV. The target nuclei were C, Al, Fe, In and

Pb. The emission angles in the measurement were 15, 30, 60, 90, 120 and 150 degrees. Fig. 1 shows the layout of the detectors and the target.

Since this measurement was carried out for a main purpose of obtaining the neutron emission double differential cross section, NE213 liquid organic scintillators were used for measuring neutrons and γ rays. The two types of scintillators were utilized in the experiment. The large ones have a diameter of 5 inch and a length of 5 inch for the priority of the detection efficiency. The others are the small size detectors which have a diameter of 2 inch and a length of 2 inch for the priority of the neutron-γ discrimination in a low energy range. To remove the charged particles from the data, the plastic scintillator NE102A were set as veto detectors in front of individual detectors. To separate pions from the incident beam by TOF, two plastic scintillators, S0 and P0, were placed on the upper stream. Two plastic scintillators, P1 and P2 were put for verifying the incident beam to the target.

3. Data Analysis

3.1 Discrimination between neutrons and γ rays

The gate integration method [3] was adopted to make pulse-shape discrimination between neutrons and γ rays. This method uses the direct monopole output signal from the detector. The ratio of integral quantities between the rise part and the decay one for γ ray events is different from that for neutrons. Gamma rays are thus distinguished from neutrons. We recorded both the rise part and the decay part of the each ADC signal, and discriminated between γ rays and neutrons. Fig. 2 shows neutron-γ discrimination.

3.2 Energy calibration of detector

The ADC spectra obtained by the experiment were calibrated by the γ ray checking source (^{137}Cs, ^{60}Co and Am-Be). Through the calibration, it was confirmed that the ADC linearity was kept in the range of 0.5 - 4.4 MeV. We attempted to calibrate by the use of the TOF neutron energy scale above 4.4 MeV.

3.3 Determination of response function

With regard to γ ray energy below 10 MeV, detector response functions were calculated by EGS4. Since the energy resolution of the detector is not considered by EGS4, we calculated the resolution by the following equation to obtain the actual response functions.

$$G(X) = \frac{C_X}{\sigma\sqrt{2\pi}} \exp\left[-\frac{(X - X_0)^2}{2\sigma^2}\right], \tag{5}$$

where σ^2 is the deviation,X_0 is the peak channel, C_x is the counts of the peak channel,

and $G(X)$ is the counts of the channel X.

On the basis of the energy resolution, we got the actual response functions considering the energy resolution of the detectors by $G(X)$ and the response functions calculated by EGS4.

$$R_{ri} = \sum G_{ij} R_j. \tag{6}$$

Figure 3 shows the response functions on the condition that the γ ray energy is 1.25 MeV and the energy resolutions range from 0 % to 30 %. Fig. 4 indicates the comparison of the spectra of a ^{60}Co standard checking source and the response function in the case that the energy resolution is 25 %.

In addition, we also calculated the detector response functions for high energy g rays by EGS4. In order to fit the condition of the experiment, the detector geometry for EGS4 was determined as shown Fig. 5. This calculation assumed that the γ ray source was 1 m apart from the scintillator front plane, and γ rays were emitted radiately from the point source.

Figures 6 and 7 indicate the calculation results by EGS4. When the γ ray energy is close to 20 MeV, the sharp peak appears 0.5 MeV below its energy. Above 40 MeV, the Compton edge is not seen. The response functions look like almost uniform above 60 MeV.

3.4 Determination of detection efficiency

In this work, the detection efficiencies for γ rays were determined by the response function with EGS4. Fig. 8 indicates the detection efficiency. Since the function is given in units of count/MeV/incidence, the integral values of each channel of the response function correspond to the detection efficiency.

4. Preliminary Analysis of Cross Section

To obtain the cross section of the γ ray emission, we used FERDO code [4]. γ rays above 10 MeV were ignored in the preliminary analysis. Fig. 9 shows the double differential cross section of the γ ray emission from the spallation reaction. The marks are the experimental data, and the lines are the calculation results by HETC-KFA2 [5] code. The experimental data are lower than the data of HETC-KFA2 in all angle. In the experiment, only the prompt γ rays (< 3 ns) were taken to ADC. However, HETC-KFA2 only considers that γ rays are emitted from nuclei after delay.

5. Conclusion

Gamma rays from the spallation reaction were measured by the use of NE213 scintillator. By the gate integration method, the neutron and the γ ray up to 70 MeV was discriminated. The response functions by EGS 4 were obtained and showed a uniform distribution above g ray energies of 60 MeV.

Acknowledgment

We express their gratitude to Prof. H. Hirayama, Dr. S. Ban and Dr. Y. Namito of National Laboratory for High Energy Physics for useful suggestion and discussion.

References

[1] W. R. Nelson, et al., *The EGS4 Code System* SLAC-Report-265 (1985).

[2] K. C. Chandler and T. W. Armstrong, *ORNL-Report* 4744 (1972).

[3] F. D. Brools, Nucl. Instrum. Meth., 4, 151 (1959).

[4] W. R. Burrus, ORNL-Report 3743 (1965).

[5] R. E. Prael and H. Lichtenstein, LA-UR 89-3014, 45 (1989) Cambridge University Press, 1990.

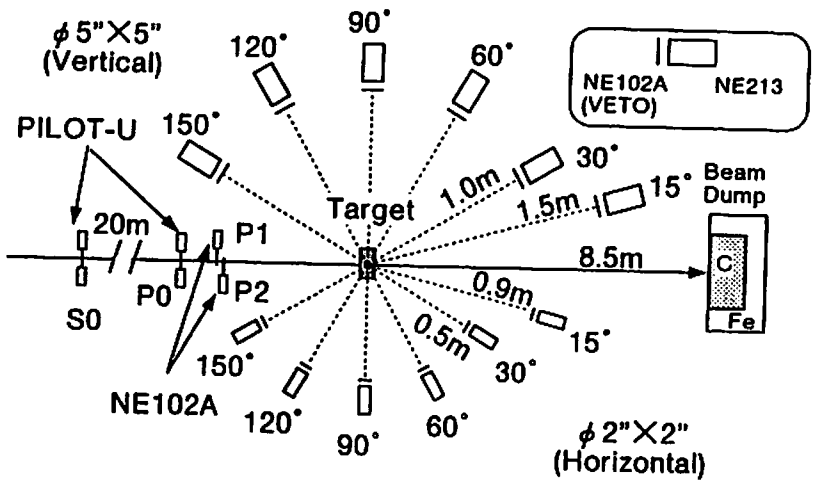

Fig. 1 Layout of detectors and target

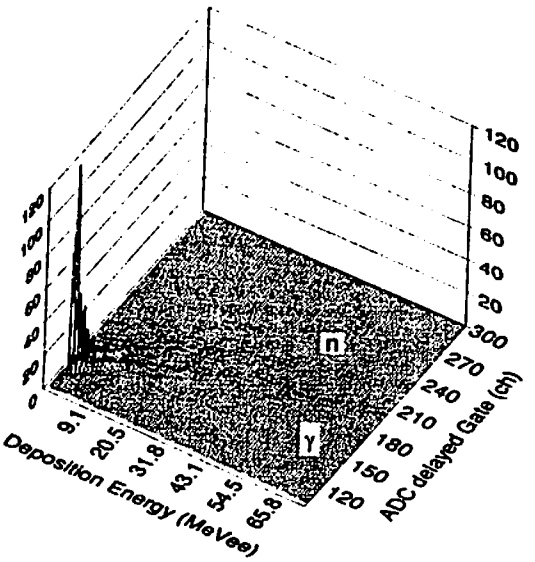

Fig. 2 neutron-gamma discrimination
by gate integration method
800 MeV p on In, Φ 5"×l 5" detector on 15°

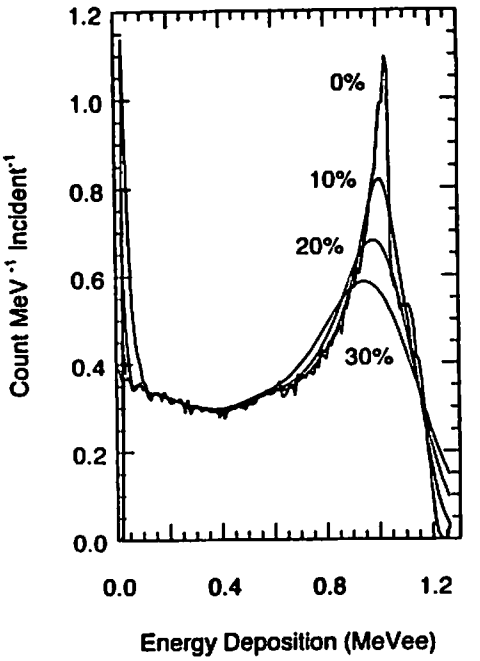

Fig. 3 Effect of energy resolution
for 1.25 MeV γ ray response function

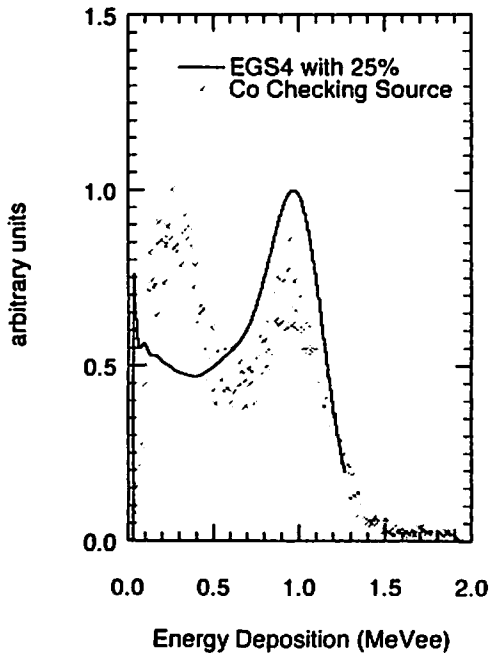

Fig. 4 Comparison of response function
by EGS 4 and ^{60}Co checking source

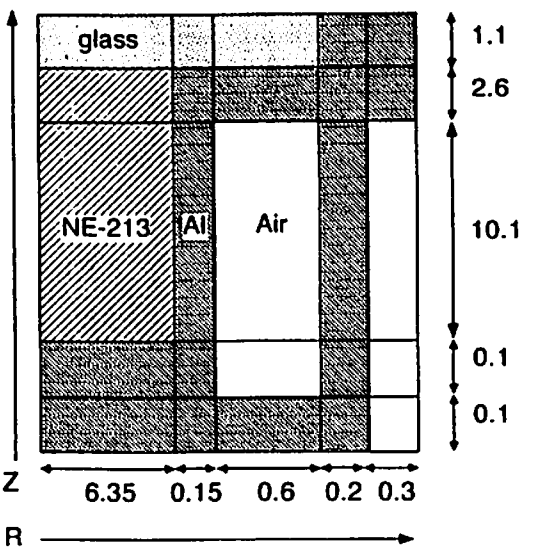

Fig. 5 Detector geometry

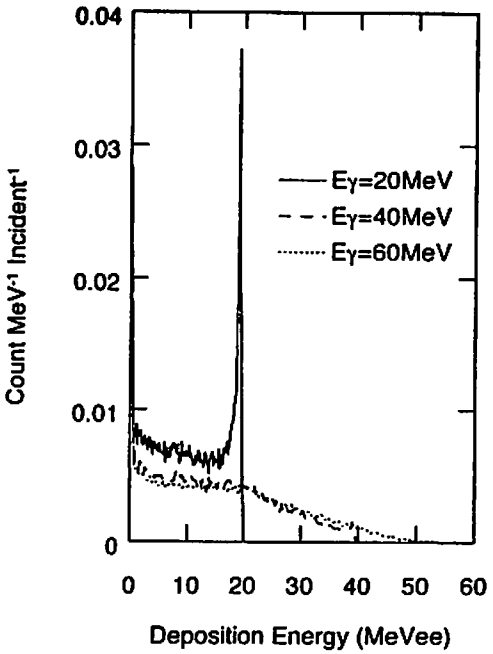

Fig. 6 Response function by EGS 4 for 20, 40, 60 MeV γ ray

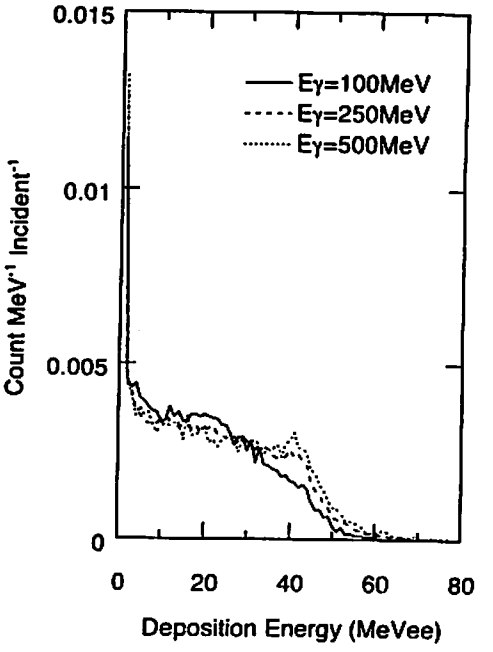

Fig. 7 Response function by EGS 4 for 100, 250, 500 MeV γ ray

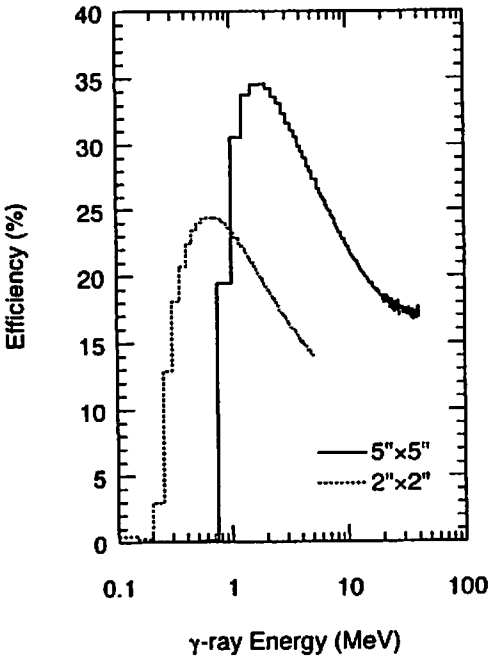

Fig. 8 Detection efficiency by EGS 4

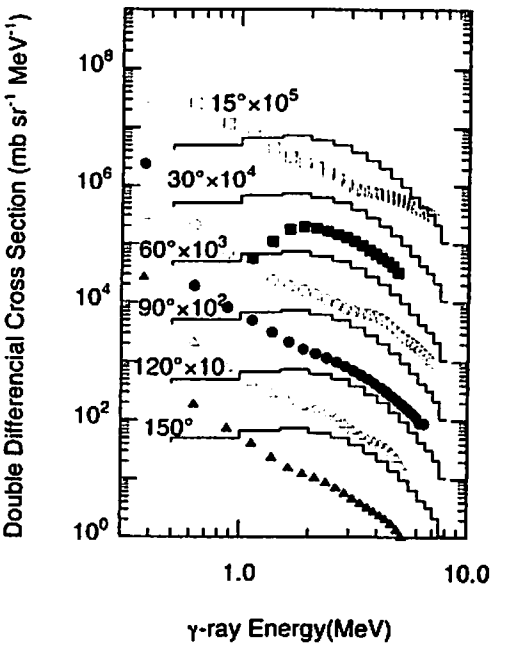

Fig. 9 γ ray creation double differencial cross section for 1.5 GeV p on In

MORE REALISTIC SIMULATION OF THE RESPONSE OF AN IONIZATION CHAMNBER

T. TORII, T. NOZAKI and H. ANDO

O-arai Engineering Center
Power Reactor and Nuclear Fuel Development Corporation
4002 Narita, O-arai-machi, Ibaraki-ken, 311-13, Japan

Abstract

In order to study the consequence of geometrical modeling of a finger tip ionization chamber and the difference of the calculated results using two Monte Carlo codes EGS4 and ITS3.0, the energy responses of an ionization chamber have been calculated. In the EGS4 calculation, it has been developed a versatile user code PRESTA-CG to calculate the response of radiation detectors with more complicated geometrical design by the combinatorial geometry (CG) method. This paper presents comparisons of the energy responses between these codes.

1. Introduction

The response of radiation detectors to gamma rays has been the subject of many Monte Carlo simulations, and consequently a large amount of work has been submitted [1-5]. In particular, the characteristics of ionization chambers by Monte Carlo calculation have been studied well [1-3], as well as those by experiments, because ionization chambers are widely used for the measurement of gamma dose-rate in various radiation fields of nuclear facilities. Since ionization chambers calibrated in terms of exposure rate are also employed usually for the calibration of various radiation detectors and dosimeters for measuring x-rays and gamma rays, ionization chambers play a central role in radiation measurements. However many of above Monte Carlo studies for radiation detectors had some restrictions on their applicability. Many studies were restricted for the detectors with simple shape, such as cylindrical and spherical detectors. Whereas some radiation detectors, ionization chambers in particular, have more complicated geometry, such as finger tip in shape, many calculations for such detectors have used simplified as cylindrical or spherical ones.

In order to study the consequence of geometrical modeling of a finger tip ionization chamber, this paper reports the response calculation of the ionization chamber modeled as a cylindrical chamber, and that modeled as a more real finger tip chamber using two

Monte Carlo codes, EGS4/PRESTA [6,7] and ITS3.0 [8]. We have written a versatile user code called CYLRESP, which uses the EGS4/PRESTA code system to calculate the response of cylindrical detectors. We have also developed a user code, named PRESTA-CG, to calculate the response of detectors with more complicated geometrical design by the combinatorial geometry (CG) method.

It is also described that the comparison with these calculation results and the experimental ones in this paper.

2. Ionization Chamber

In this simulation calculation, the ionization chamber (VICTOREEN Inc.: Radocon 550-3) selected is a popular standard ionization chamber that is using for calibration of survey meters and other radiation measurement equipment. The shape of the chamber is a finger tip that is combined with hemispheres and a cylinder.

A cross-sectional view of the ionization chamber is shown in Fig. 1. The ion-collecting electrode is made of polystyrene with 4.7 mm in diameter and 170 mm in height. Also, the chamber is made of polymethyl methacrylate (PMMA) with 56.2 mm in diameter and 176 mm in height, the thickness of the wall is 1.4 mm (166 mg/cm^{2}2) and its effective volume is about 330 cm^{3}3. Moreover, for irradiation of high energy gamma rays above about 500 keV, a buildup cap (BC) made of PMMA is usually covered over the chamber. For example, the BC with 3 mm thickness (368 mg/cm^2) is used for cesium-137 and cobalt-60 irradiation.

We have calculated the response of the above chamber modeled as a cavity-volume and diameter equivalent cylinder using the EGS4/CYLRESP and ITS/ACCEPT, and the chamber modeled as a more real finger tip shape using EGS4/PRESTA-CG and ITS/ACCEPT, as illustrated in Fig. 2. ITS3.0 series includes various codes, such as TIGER, CYLTRAN, and ACCEPT. We have, here, selected ACCEPT code, because ITS/ACCEPT can make finger tip and cylindrical shapes by the CG description.

In this response calculation, the broad parallel beam of monoenergetic photons was irradiated from the side on the chamber, and deposited energy in the cavity was calculated. To compare the experimental results, the atmospheric air in the cavity was employed at the pressure of 101.3 kPa and at the temperature of 22°C. The energy range of photons is from 30 keV to 800 keV for the chamber without any BC, and from 500 keV to 5 MeV for that with the 3 mm thick BC. To reduce statistical uncertainties below 3 %, the calculations were performed in an arbitrary number of batches (10), and a billion histories for above 800 keV photons and ten billion histories for other photons were used per batches. In the calculation using EGS4 code, we used the lagged Fibonacci pseudo random number generator developed by G. Marsaglia et al. [9].

Moreover, using following equation, we evaluate the conversion factor [A/mR-h^{-1}],

$$I = eE_{dep}/W, \tag{7}$$

where

I:ionization current per square centimeter [A/cm^2],
e:electronic charge [C],
E_{dep}: Deposited energy per unit photon fluence [eV/cm^2],
W: W-value for air [=33.97 eV [10]].

3. Results and Discussion

The results calculated with EGS4/PRESTA and ITS/ACCEPT for the cylindrical model are shown in Fig. 3. These data agreed well within 3region calculated, and there are not significant differences in the responses calculated by EGS4/PRESTA and ITS/ACCEPT. Experimental data are also good agreement with these calculational data. Moreover, responses calculated using EGS4/PRESTA-CG and ITS/ACCEPT for the finger tip model are good agreement within 5 %, and agreed well with experiment, as shown in Fig. 4.

From these results, it was not observed the difference of these geometrical models concerning the response of the ionization chamber.

Responses calculated above are for uniform parallel beam covered whole cross section of the ionization chamber. Next, we calculated the response of the finger tip chamber for collimated parallel beam perpendicular to the central axis of the chamber. The width of beam was 5 mm, and irradiating positions were moved 5 mm by 5 mm from the top of the chamber to cylindrical portion. The response calculated is illustrated in Fig. 5. Although the response in low energy region below 500 keV is lower than that in high energy region in the vicinity of the chamber top, that is not so low in the vicinity of cylindrical portion of the chamber. From this result, it seems that the response for multiform beam field and for narrow beam field must be evaluated carefully in low energy region.

Acknowledgment

We would like to thank to Mr. T. Sugita in VIC for his technical assistance.

References

[1] R. Nath and R. J. Schulz, Med. Phys., **8**, 85 (1981).

[2] A. F. Bielajew, D. W. O. Rogers and A. E. Nahum, Phys. Med. Biol., **30**, 419 (1885).

[3] D. W. O. Rogers, A. F. Bielajew and A. E. Nahum, Phys. Med. Biol., **30**, 429 (1885).

[4] D. W. O. Rogers, Nucl. Instrum. Meth., **199**, 531 (1982).

[5] M. Conti, et al., Nucl. Instrum. Meth., **A322**, 591 (1992).

[6] W. R. Nelson, H. Hirayama and D. W. O. Rogers, SLAC Report-265 (1985).

[7] A. F. Bielajew and D. W. O. Rogers, Nucl. Instrum. Meth., **B18**, 165 (1987).

[8] J. A. Halbleib, R. P. Kensek, T. A. Mehlhorn, G. D. Valdez, S. M. Seltzer, and M. J. Berger, SAND91-1634 (1992).

[9] G. Marsaglia, A. Zaman and W. W. Tsang, FSU-SCRI-50 (1987).

[10] M. Boutillon and A. M. Perroche-Roux, Phys. Med. Biol., **32**, 213 (1987).

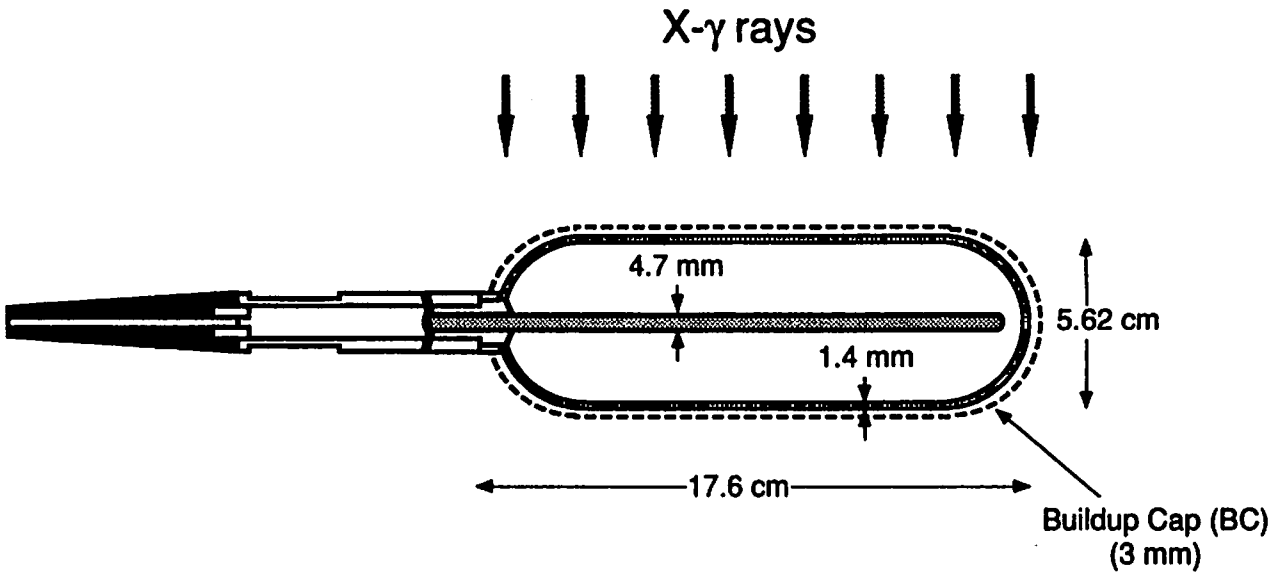

Fig. 1 Ionization Chamber
(Radocon 550-3)

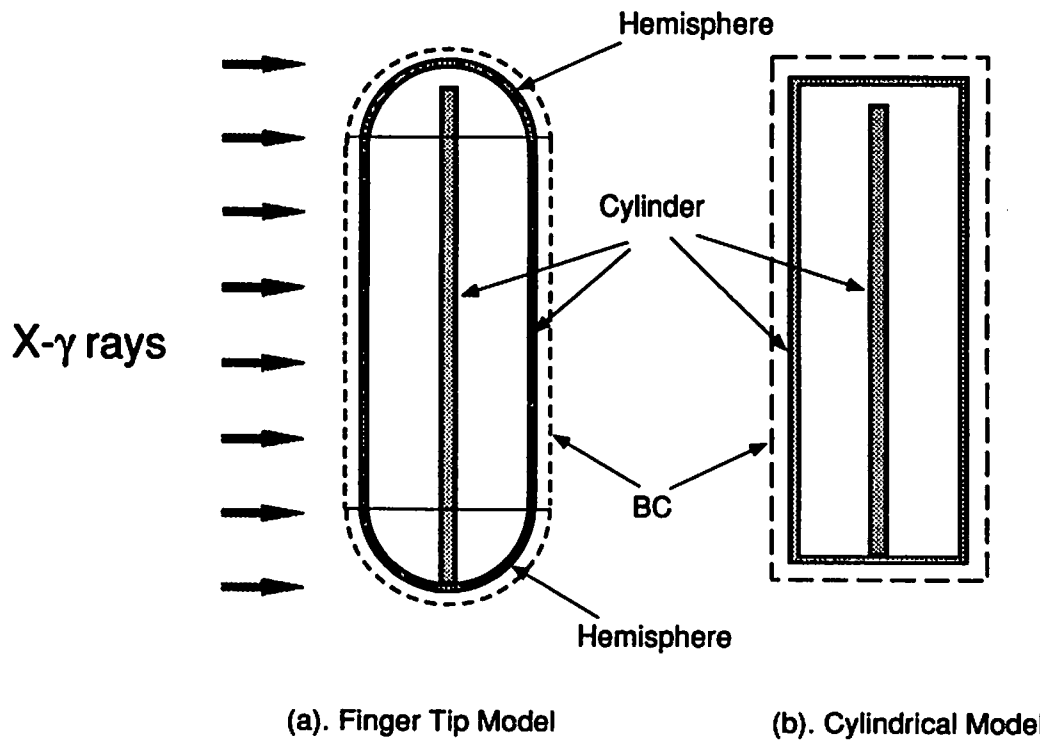

Fig. 2 Calculation Geometry

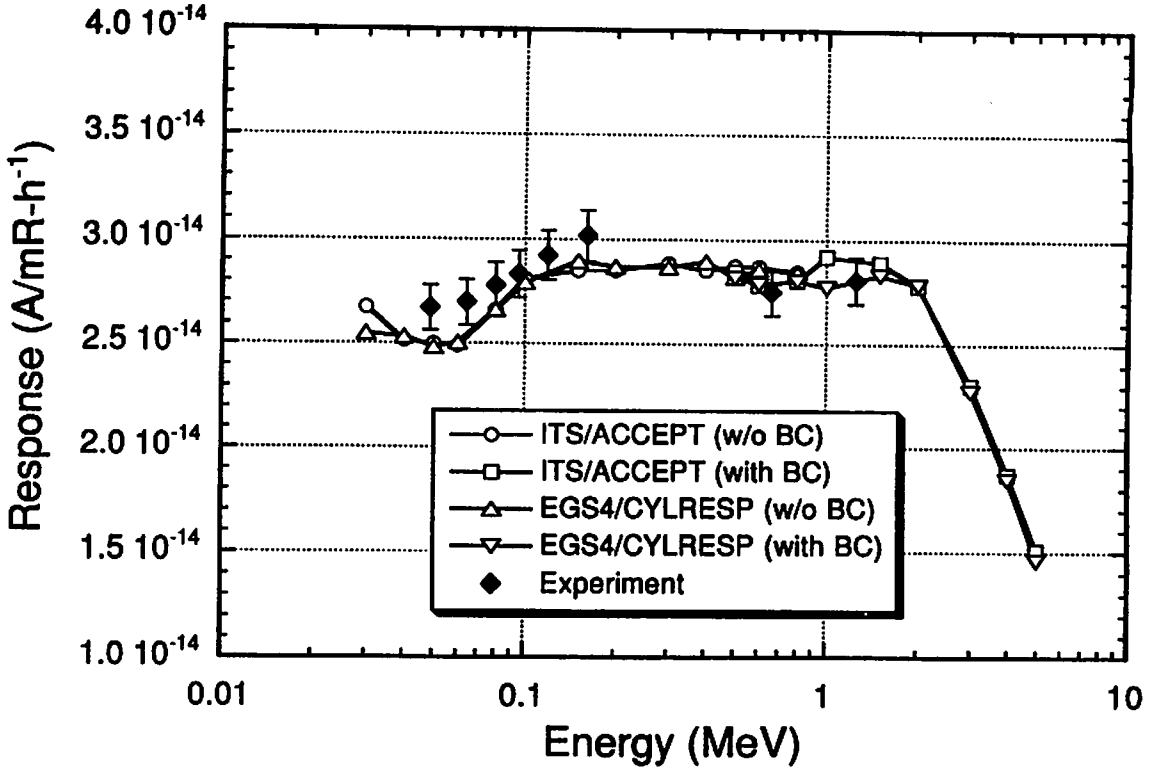

Fig. 3 Response of the ionization chamber modeled as a cavity volume equivalent cylinder

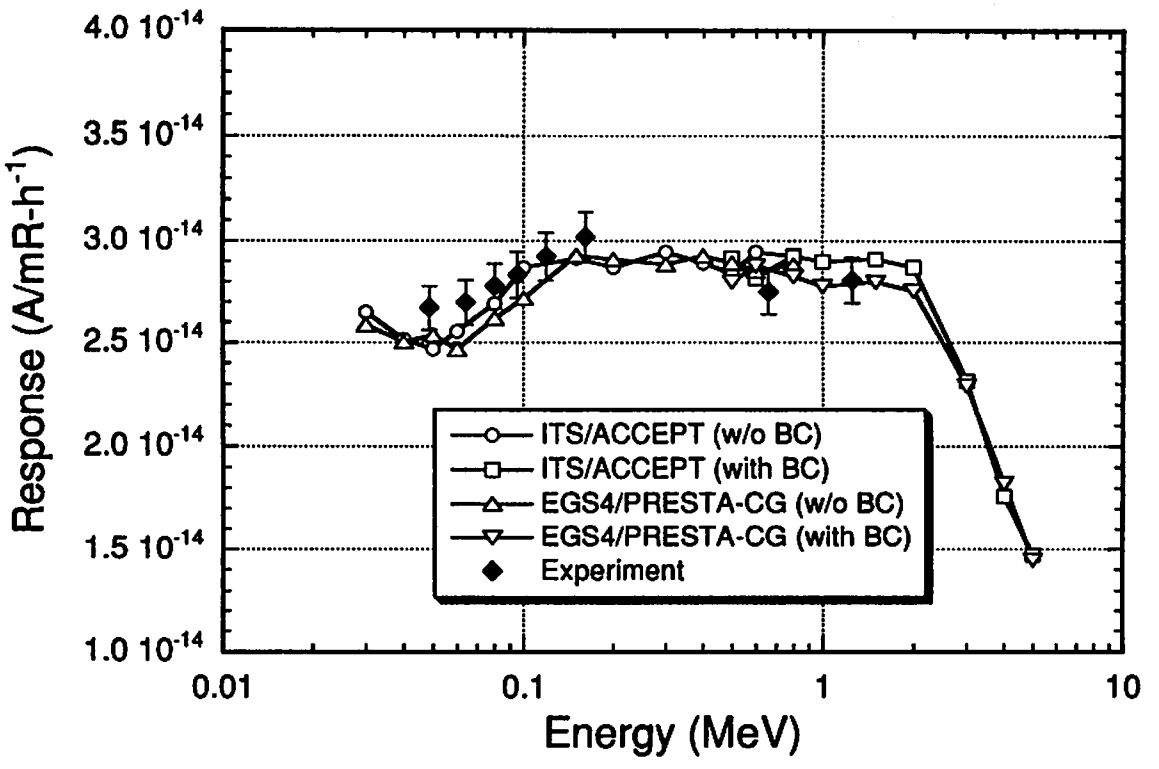

Fig. 4 Response of the ionization chamber modeled as a finger tip shape

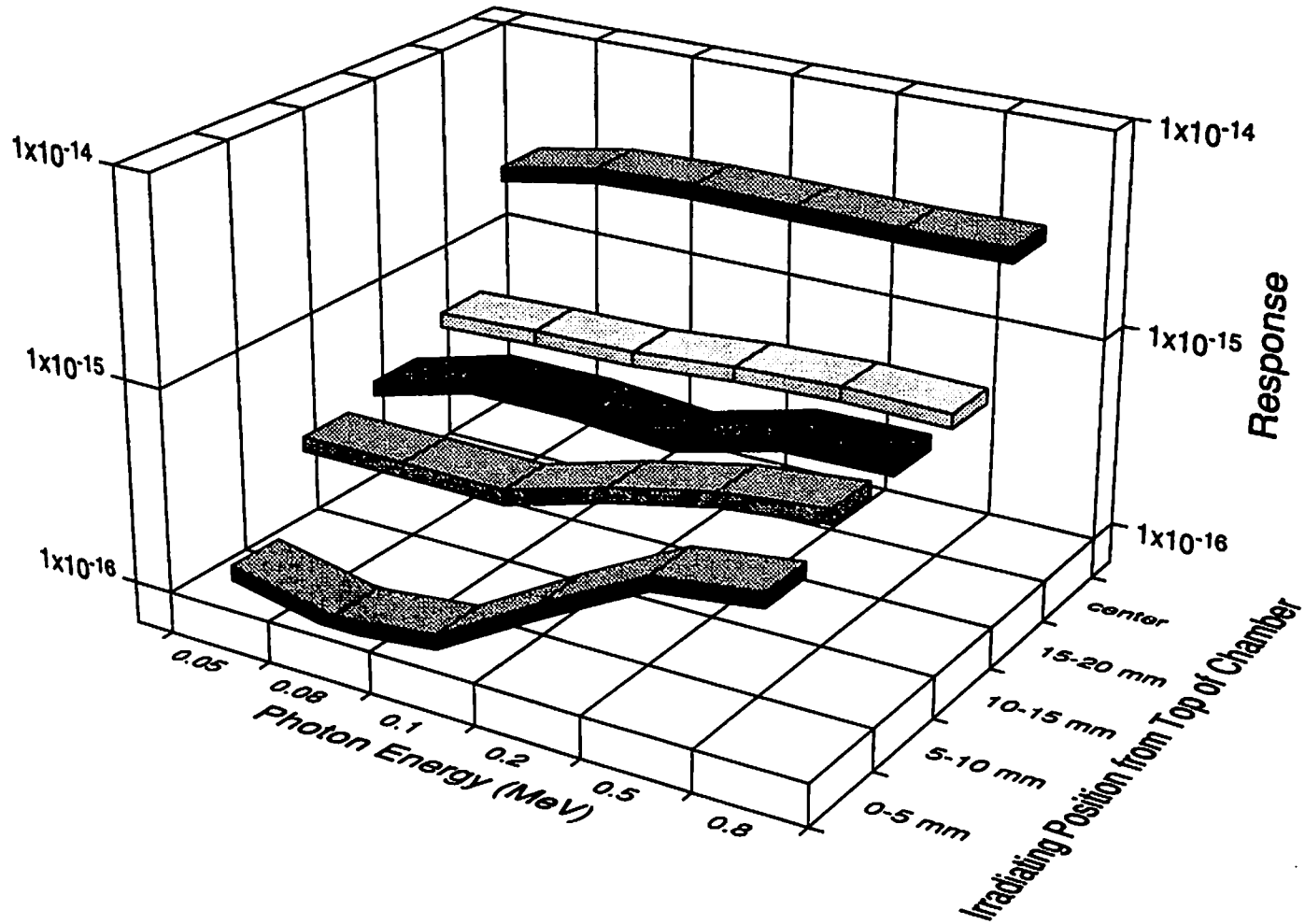

Fig. 5 Response of the finger tip chamber for narrow photon beam

ABSORBED DOSE IN POLYMERS DURING A POSITRON ANNIHILATION EXPERIMENT

T. SUZUKI, Y. NAMITO, Y. OKI, M. NUMAJIRI, T. MIURA,
H. HIRAYAMA, K. KONDO and Y. ITO*

Radiation Safety Control Center, National Laboratory for High Energy Physics, Tsukuba, 305 Japan

** Research Center for Nuclear Science and Technology, The University of Tokyo, Tokai-mura, Ibaraki, 319-11 Japan*

Abstract

A positron annihilation lifetime (PAL) technique has been recognized as being a useful method to study the characteristics of polymers. However, radiation effects due to positrons used as a probe have been raised as being a problem, since positrons emitted from ^{22}Na have sufficient energy to induce radiation damage in polymers. In this study, the radiation dose induced by positrons emitted from ^{22}Na was estimated for such polymers like polyethylenes and polypropylenes using the EGS4 code. The radiation damage during PAL measurements is also discussed. It has been shown that the calculated dose is consistent with that estimated from an empirical equation of the mass-attenuation coefficient.

1. Introduction

Positrons injected into polymers lose energy through interactions with atoms and molecules, which are thermalized with a short period of the order of ps, and finally annihilate with electrons, emitting annihilation γ-rays. A part of the positrons form positroniums (Ps) inside terminal spurs created by positrons with an energy less than 500 eV. A Ps is a hydrogen-like bound state having two spin states: one is para-Ps (p-Ps) with an anti-parallel spin orientation; the other is ortho-Ps (o-Ps) with a parallel spin orientation. These states have intrinsic self-annihilation lifetimes of 0.125 and 142 ns in a vacuum, respectively.

Once an o-Ps is trapped in free volumes or intermolecular-space holes, it is annihilated through interactions with electrons located on the surface of the holes. This is called a pick-off process. The typical PA spectra comprise three different lifetime components: the longest lifetime component has been assigned to the annihilation of an o-Ps (τ_3: 2 $\sim$ 3 ns), the shortest one to p-Ps (τ_1: $\sim$ 0.125 ns in vacuum) and the intermediate one

to the self-annihilation of free positrons (τ_2: 0.3 $\sim$ 0.5 ns). The lifetime of an o-Ps in polymers is far less than that in a vacuum, and is related to the size of the intermolecular-space holes. However, the intensity of an o-Ps is not simply explained by the number of holes in which the Ps are trapped. It has been understood that it is strongly dependent on the characteristics of the polymers: e.g., the chemical structures (electro-affinity); geometrical structures; crystallinity: and states like liquid, solid, glass and rubber. Hence, by investigating the intensities and lifetimes of the o-Ps, the characterization of materials can be analyzed. This technique has been understood as being a positron annihilation (PA) or positron annihilation lifetime method (PAL).

PA has been recognized as a non-destructive test (NDT), and has been successfully applied to the characterization of both metals and semi-conductors. It has also been applied to polymers, and has proven to be a useful method [1, 2, 3, 4]. Because of NDT, it is expected that no effect is induced into samples during a measurement by positron probes. However, it has been pointed out that the positron irradiation effect was quite significant in polyethylenes (PEs) and polypropylenes (PPs) [5, 6] during an experiment involving PAL. These polymers are considered to be weaker against radiation than such aromatic compounds as epoxy resins and polyimides. Hence, it has been suggested that any PAL experiment using PE and PP samples must be carefully conducted.

In order to investigate the radiation effect of positrons, the absorbed dose must be estimated. In this work a Monte-Carlo electron-positron-photon transport (EGS4) [7] code was utilized to calculate the total dose induced by positrons emitted from ^{22}Na in PEs and PPs; the result was compared with that estimated from an empirical equation of the mass-attenuation coefficient.

2. Experiment and Calculation

2.1 Experimental

The PA experiments were conducted with a conventional fast-fast coincidence system having a time resolution of 270ps full-width at half maximum (FWHM). The details concerning the experimental set-up have been given elsewhere [8, 9].

Positron sources were prepared by depositing 1.1 MBq (30 μCi) of aqueous ^{22}NaCl onto a thin Kapton foil of 7 μm thick and having 10$\times$10 mm^2 area, being covered by the same size of foil after drying. The diameter of the deposit was in the range between 1.0 to 1.5 mm.

PE (PP) samples of 2 mm thick, used for the PA experiment, were of almost the same size as the Kapton foil described above. During the experiment the source was sandwiched by two PE (PP) samples and data taking was continued for 70 h. The PAL spectra were

stored every hour in a disk and 1.5 million events were collected in one spectrum.

2.2. Calculation with the EGS4 code

Figure 1 shows a model of samples for the EGS4 calculation, in which the cylindrical coordinates R and θ in a plane and Z extending perpendicularly into the beam direction were employed.

There were two kinds of systems used for the calculation: one was for a point source to calculate one-dimensional stopped-positron distributions along the Z or R directions; the other was for the surface source to calculate the two dimensional (R, Z) radiation-dose distributions.

In order to study the positron distributions stopped in both the Z and R directions, a point beam with a monochromatic energy was injected perpendicularly onto the center of the surface of a cylinder. For the stopped-positron profiles along the Z directions, the thickness was assumed to be 5 mm, which was sufficient to stop all positrons with an energy of 550 keV, and was divided into 250 along the Z directions (i.e., ΔZ=20μm and n=250 in Fig.2). For this calculation, only one region (m=1) along the radial directions was assumed; the radius was also assumed to be R=5 mm in order to stop all positrons of 550keV. This geometry was selected because the system was simple enough to calculate the one-dimensional stopped-positron distributions.

Similarly, for the profiles along the R directions, only one region was assumed along the Z directions with a thickness of 5 mm; the radius was divided into 250 segments along the R directions (i.e. ΔR=20μm (m=250) and Z=5 mm (n=1) in Fig. 2).

The surface source was placed on the surface of the (R,θ)-plane and positrons were injected into the Z-direction from random points generated inside the source area. The diameter of the cylinder was 2.5 mm and was divided into 25 parts along the radial direction, ΔR=50μm and m=25. Although the diameter of the positron source was in the range of from 1 to 1.5 mm, the intense part was considered to be within 1 mm. Hence, the diameter of the source was assumed to be 1 mm, i.e. it covered the area up to m=10. The thickness of the sample was assumed to be 1 mm and divided into 50 parts along the Z-direction (ΔZ=20μm and n=50). Hence, the cylinder was divided into 25×50 space regions, resulting in 1253 regions, including the front, back and side regions. Figure 2 shows how the sample's regions are numbered. The media for each region were assigned as follows: region 1 is a front vacuum region, 2 $\sim$ 1251 PE or PP material regions , 1252 a vacuum region of the back side and 1253 the side vacuum region.

Positrons produced from ^{22}Na have an energy distribution as shown in Figure 3, which was constructed from a data book [10]; the maximum energy is around 545 keV. Since the trajectory of low-energy positrons below 10 keV must also be followed, the cut-off

energy for both positrons and γ-rays was set at 1 keV: ECUT=1 keV and PCUT=1 keV. An EGS4 calculation was conducted every 10 keV in the energy ranges from 10 to 550 keV, resulting in 55 kinds of tables. In these tables, the numbers of positrons stopped in each region, the energies deposited by positrons, the secondary electrons and γ-rays, and these total energies were recorded for all regions. In these calculations, for each energy 50k events were generated for the point source and 100k events for the surface source.

3. Results and Discussion

3.1. Positron annihilation results concerning o-Ps

In polymers, Ps formation is affected by its polymer structures, such as crystallinity and molecular weight, resulting in a variation of the o-Ps intensities (I_3). From these points of view, the radiation effects of positrons and γ-rays on PE and PP have been studied and reported elsewhere [3, 6, 11].

During measurements of PA, samples were constantly irradiated by positrons emitted from ^{22}Na. Figure 4 shows the results of τ_3 and I_3 for the PE and PP samples for the case of the source described in the Sec. 2.1. For both samples, although no change was observed in τ_3 for 70 h, I_3 decreased with time. The former suggests that the size of the intermolecular-space holes was not affected by the positron irradiation, but that the latter clearly indicates the effect on Ps formation. Furthermore, the irradiation effects are larger in air than in a vacuum, and PP has received a larger effect than PE.

3.2. Positron distribution stopped in a cylinder

Figures 5 and 6 show the stopped positron distributions along the Z and R directions for 5 different energies, respectively. These suggest that positrons with an energy of 500 keV (nearly equal to the maximum energy) can penetrate 2 mm into the Z direction and 1.8 mm into the R direction from the injection point. By folding the energy distribution of positrons (Fig. 3) with the 55 tables of stopped-positron distributions described in Sec. 2.2, the distribution of positrons emitted from ^{22}Na can be obtained, as shown in Figure 7.

Using the tables of the stopped-positron distributions, the penetration length, in which the number of positrons decreases to 1/e ($\sim$ 0.37), was calculated in the Z direction for 55 kinds of energies, and is shown in Figure 8 (○).

An empirical equation of the mass-absorption coefficient for positrons emitted from ^{22}Na was determined as follows [12]:

$$\frac{\alpha}{\rho} = 2.8 \times \frac{Z^{0.15}}{E^{1.19}} \qquad (\mathrm{cm}^2/\mathrm{g}), \tag{8}$$

where α is the positron linear-absorption coefficient (1/cm), ρ the density of samples (g/cm^3), E the mean energy expressed in MeV, and Z the average atomic-number.

Assuming ρ=0.96 g/cm^3 for PEs and PPs, $1/\alpha$ is considered to be the penetration length corresponding to 1/e, which is also shown in Figure 8 ($\diamond$). The penetration length obtained from Eq. (1) is greater than the length obtained by the EGS4 code.

Although several empirical equations used to estimate the penetration length have been presented [13, 14], these are not discussed in this paper because the estimates of these equations were one order smaller than Eq. (1), the origin was not clearly specified in the references and Eq. (1) is in good agreement with the results of the EGS4 calculation, as shown below.

3.3 Absorbed dose calculated by the EGS4 code

Positrons injected from ^{22}Na lose energy through two basic processes: collision and radiation. The EGS4 code takes care of these energy losses; the details are given in the Ref. 7.

The dose induced by the positrons can be obtained from total energies deposited in each region (Fig. 2) divided by the weight of the materials of the region. Typical dose distributions in the Z and R directions are shown in Figures 9 and 10, respectively.

Figure 9 shows two dose distributions near to the central axis (from n=1 to 50 for m=1 ($\bigcirc$) and for m=5 ($\times$)). The distributions for m=2 $\sim$ 4 are also similar to these distributions, suggesting the following; (1) near to the central axis each of the regions is similarly irradiated by positrons, and (2) the maximum dose of around 0.94 Rad (or 0.0094 Gy) for 100k events appeared at around Z=40 $\sim$ 80 μm. Figure 10 presents the distributions along the R-direction for n=1, 2, 5, 25, and 40. These indicate the following findings: (1) the boundary of ^{22}Na sources with a radius of 0.05 cm is clearly seen at lower n; (2) at large n the dose becomes lower and spread beyond the radius of the source, consistant with the spread of the stopped-positron distribution, as shown in Figure 6; (3) the first layer along the source (n=1) was less irradiated than the neighboring layers (n=2 $\sim$ 5); and (4) the maximum dose appeared in the region between Z=40 and 100 μm (Fig. 9) within R=400 μm.

3.4. Comparison of the dose determined by the empirical equation and the EGS4 code

A simple estimate of the dose absorbed in samples can be made using Paulin's empirical equation of the linear absorption coefficient (Eq. (1)). The diameter of the positron source was about 1 mm. It may be assumed that all of the positrons emitted from ^{22}Na stop uniformly in a cylinder with a volume V_L= 1 mm$\phi\times$L.

There are large ambiguities in determining L. Although the average energy of positrons (Fig. 3) is 215 keV, it is expected that the average energy is reduced due to self-absorption inside the source and the effect of the source-supporting materials. Also, up to 10% of the low energy positrons may be absorbed within the source materials described in Sec. 2.1. To simplify the estimate, these effects are assumed to be small. Then, $E = 0.215$ MeV. For PEs $(\text{-CH}_2\text{-})_n$, $Z = (Z_C + 2Z_H)/3 = 2.7$. Hence, from Eq. (1), $\alpha = 19$ cm^{-1}, resulting in a 1/e penetration length (L=) of 510 μm (this result is also the same for PP). Assuming that half of the positrons (because of geometrical efficiency) emitted from 1.1 MBq-^{22}Na stop uniformly in V_L, the average dose in the volume becomes 130 Gy/h.

The EGS4 calculation produced a maximum dose of 0.0094Gy for 100k events, suggesting that the maximum dose for the source mentioned above becomes as high as 190 Gy/h. Also, using the results of the EGS4 calculation for the cylinder assumed above (n: 1~25, m: 1~10 in Fig. 2), the average dose in the volume became 115 Gy/h. Consequently, considering the crude approximation in the estimate of the dose using Eq. (1), these two average doses agree well.

3.5. Effect of the dose on Ps formation

As discussed in Sec. 3.1, I_3 was affected by the positron irradiation effect; the decrease in I_3 was about 5% after 12h for PP. From a study of the ^{60}Co γ-ray radiation effect on these polymers, the decrease in I_3 for PP was 5% for 1MGy irradiation [11]. Using the results of EGS4, the maximum dose can be estimated to be as high as 2.3 kGy for the 12h PA experiments, due to positron irradiation, which is about 500-times lower than the dose of the γ-ray irradiation to achieve a 5% decrease. If the decrease is due to radiation damage of the polymer structures and radiation-induced free radicals, the decrease is considered to be of the same order for both positron and γ-ray irradiation. However, there is a large difference in the dose necessary to achieve the same effect on I_3, suggesting that the radiation effect is not the main effect. The difference is now under investigation.

4. Conclusion

During PA experiments the decrease in I_3 was observed for PP and PE samples. The cause was considered to be due to the radiation effect of positrons emitted from the ^{22}Na source. In order to estimate the radiation dose, the penetration length of positrons was calculated using empirical equations. Comparing the result with an EGS4 calculation, it was clarified that the average dose obtained by Paulin's equation (Eq. (1)) was consistent with the calculation. A maximum dose as high as 2.3 kGy for 12h PA experiments was obtained by a calculation. In this experiment, Ps formation was affected and the decrease in I_3 was observed to be about 5%. From the ^{60}Co γ-ray irradiation experiments, a

decrease of 5 % was achieved by 1 MGy irradiation. The large difference in these doses suggests that the radiation effect can not be the main cause of the decrease.

Acknowledgment

For ^{60}Co γ-ray irradiation, the Inter-University Laboratory for the Common Use of JAERI facilities is acknowledged. This work was supported in part by a Grant-in-Aid of the Japanese Ministry of Education, Culture and Science.

References

[1] F. J. Balta Calleja, J. Serna, J. Vicente and M. A. Segovia M.A., *Structural implications on positron lifetimes in lamellar polyethylene with chain defects*, J. Appl. Phys., **58**, 253 (1985).

[2] Y.C. Jean, *Positron annihilation spectroscopy for chemical analysis: a novel probe for micro-structural analysis of polymers*, Microchemical Journal, **42**, 72 (1990).

[3] T. Suzuki, Y. Oki, M. Numajiri, T. Miura, K. Kondo and Y. Ito Y., *Positron annihilation in irradiated and unirradiated polyethylenes*, J. Poly. Sci., **B30**, 517 (1992).

[4] Z. Zhang and Y. Ito, *Micro-structures of gamma-ray irradiated polyethylenes studied by positron annihilation*, Radiat. Phys. Chem., **38**, 221 (1991).

[5] M. Walender and F.H.J. Maurer, *Decrease in o-Ps formation in polymers during positron lifetime measurements*, Mat. Sci. Forum, **105-110**, 1811 (1976).

[6] T. Suzuki, Y. Oki, M. Numajiri, T. Miura, K. Kondo, and Y. Ito, *Positron irradiation effects on polypropylene and polyethylene studied by positron annihilation*, Radiat. Phys. Chem. to be published.

[7] W. R. Nelson, H. Hirayama, and D.W.O. Rogers, *The EGS4 Code System*, SLAC-Report-265 (1985).

[8] T. Suzuki, Y. Oki, M. NUmajiri, T. Miura, K. Kondo, Y. Ito and Y. Shiomi, *Novolach epoxy resins and positron annihilation*, J. Appl. Poly. Sci., **49**, 1921 (1993).

[9] T. Suzuki, Y. Oki, M. Numajiri, T. Miura, K. Kondo, Y. Shiomi, and Y. Ito, *Effects of aging and oxidation on positronium formation in polyethylenes*, Radiat. Phys. Chem., **43**, 557 (1993).

[10] Y. Murakami, H. Senno and M. Kobayashi, *Radiation Data Book*, Tijin Shokan, Tokyo (1982) (Japanese).

[11] T. Suzuki, Y. Oki, M. Numajiri, T. Miura, K. Kondo, and Y. Ito, *Structure dependence of gamma-ray irradiation effects on polyethylenes studied by positron annihilation*, Radiat. Phys. Chem. to be published (1994).

[12] R. Paulin *Implantation of fast positrons in solids*, Positron Solid-State Physics edited by P.Papali, North-Holland Pub. Co., New York pp.565-580 (1983).

[13] A. Uedono, *Measurements of positron annihilation and its information*, The Science of positron annihilation edited by Y.Ujihira, Japan Isotope Association Y. Ujihira, Maruzen, Tokyo, pp.44-52 (1993) (Japanese).

[14] Y. Ito, H. Kaji, Y. Tabata, and K. Yoshihara, *Soryusi no kagaku* or *Chemistry of elementary particles*, Gakkai shuppann center, Tokyo(1985) (Japanese).

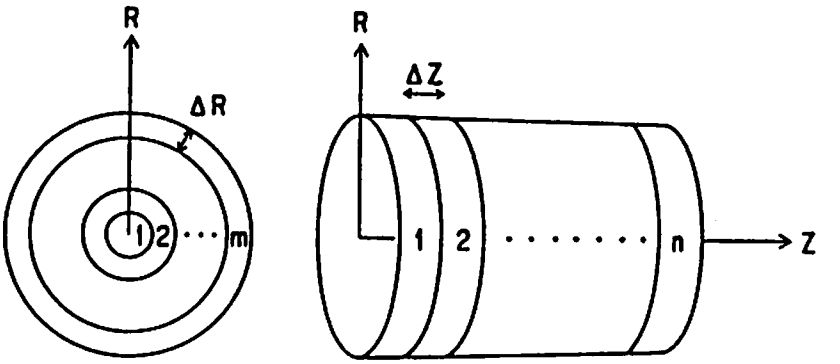

Figure 1 Cylindrical coordinates for the EGS4 calculation.
R is divided into m with the separation ΔR and Z into n with ΔZ.

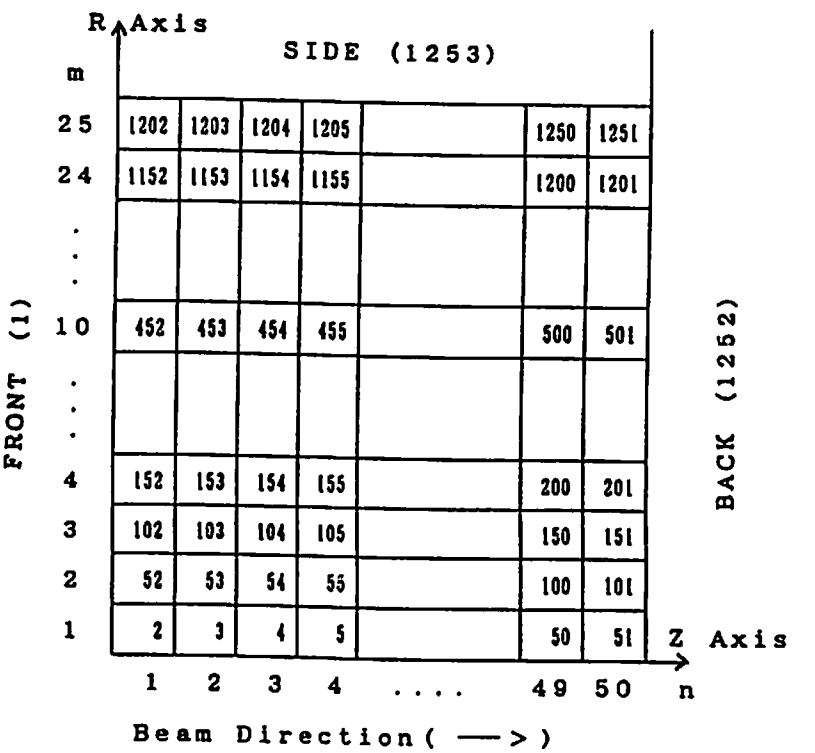

Figure 2 Assignment of numbers for each region. The front, back, and side regions are of the vacuum region and the cylinder of the material region is divided into 50×25 =1250 regions. In Fig.1, n=50 and m=25

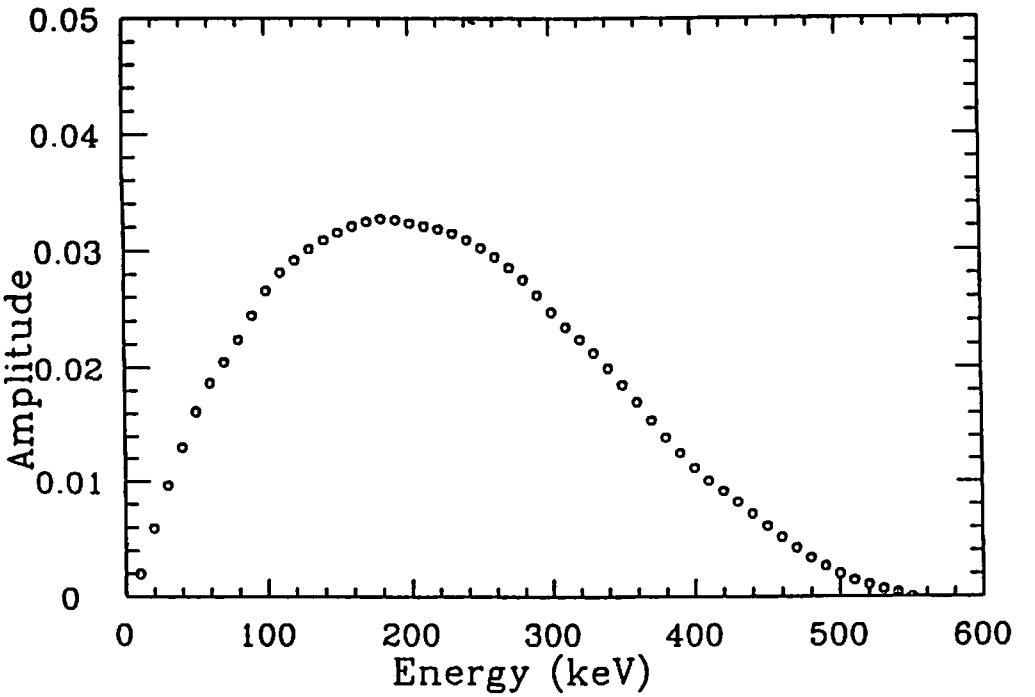

Figure 3 Normalized energy spectrum of positrons emitted from ^{22}Na.
The average energy is 215 keV and the maximum energy is 545 keV.[10]

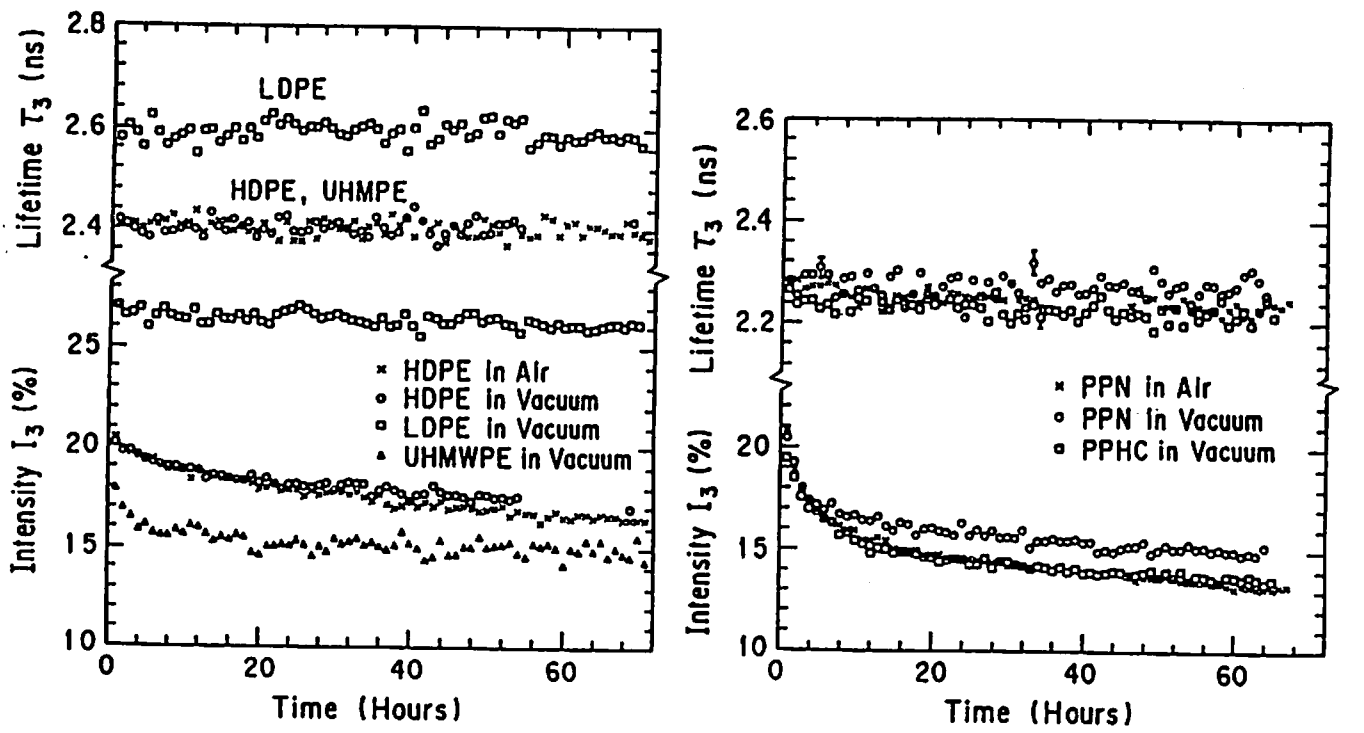

Figure 4(a) Figure 4(b)

Positron irradiation effects on τ_3 and I_3 for (a) polyethylenes and (b) polypropylenes. Positrons were emitted from ^{22}Na. The abbreviations in these figures are as follows: HDPE is a high-density PE, LDPE a low-density PE, UHMWPE a ultra-high molecular weight PE, PPN a normal PP with a 55% crystallinity and PPHC a high-crystallinity PP with a 65% crystallinity. The details are given in the Ref. 6.

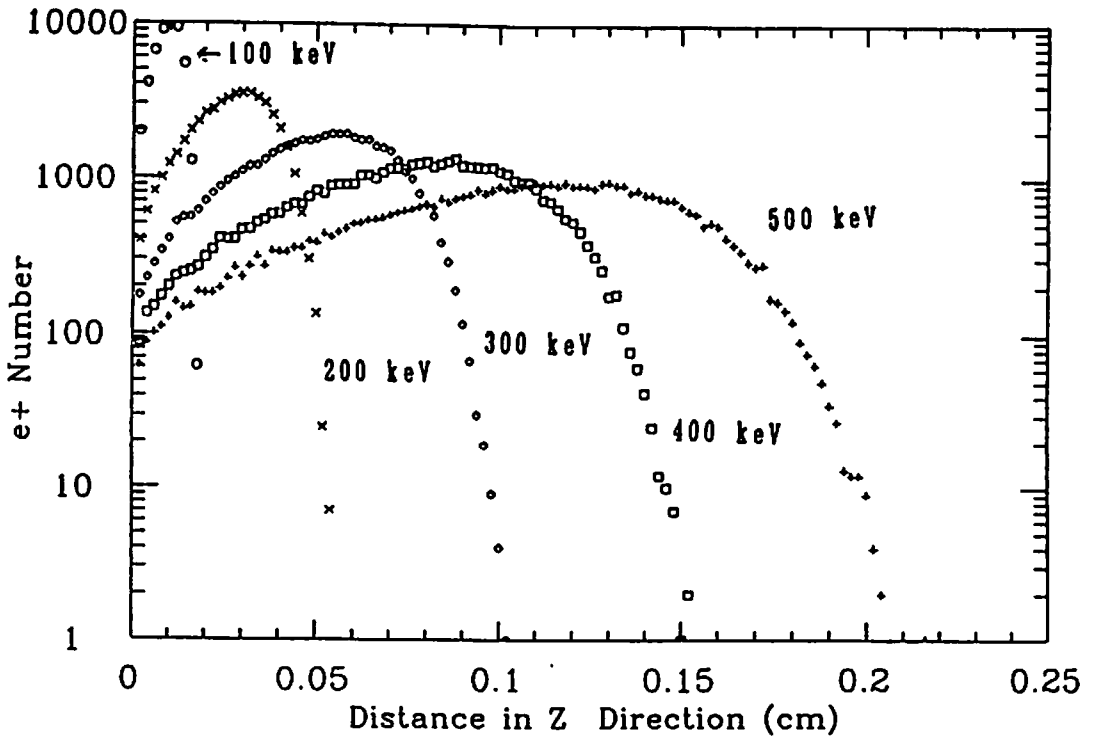

Figure 5 Stopped-positron distributions along the Z-direction for five kinds of mono-energetic point beams of positrons.

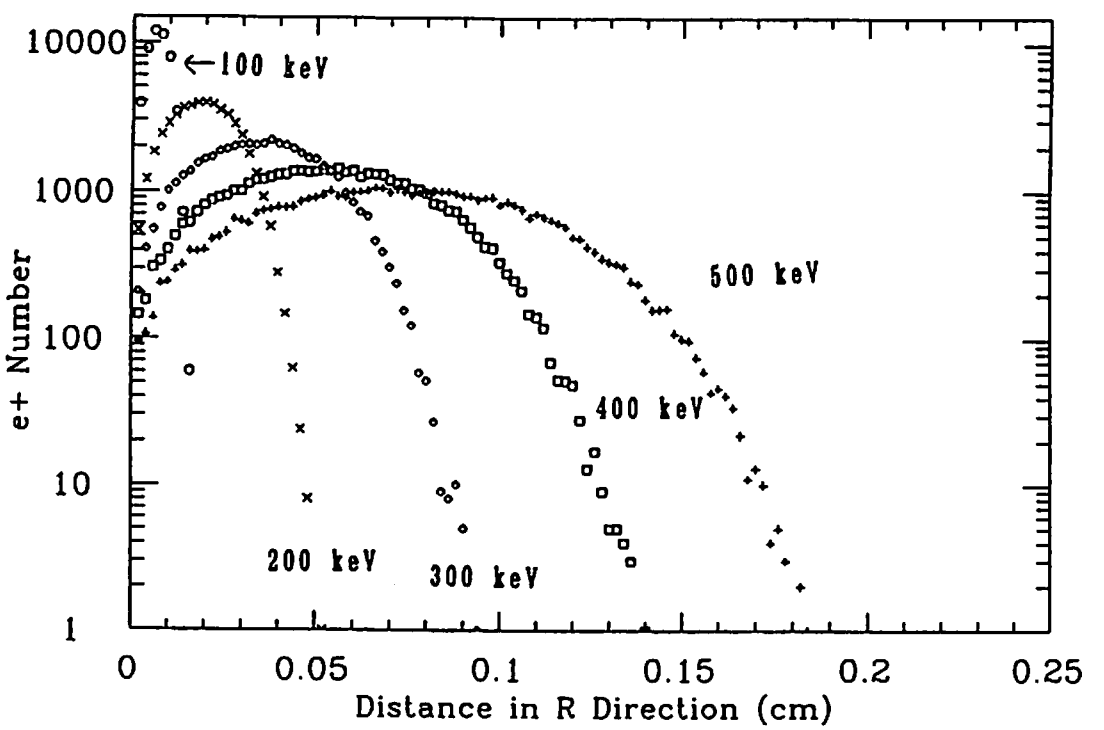

Figure 6 Stopped-positron distributions along the R direction for five kinds of mono-energetic point beams of positrons.

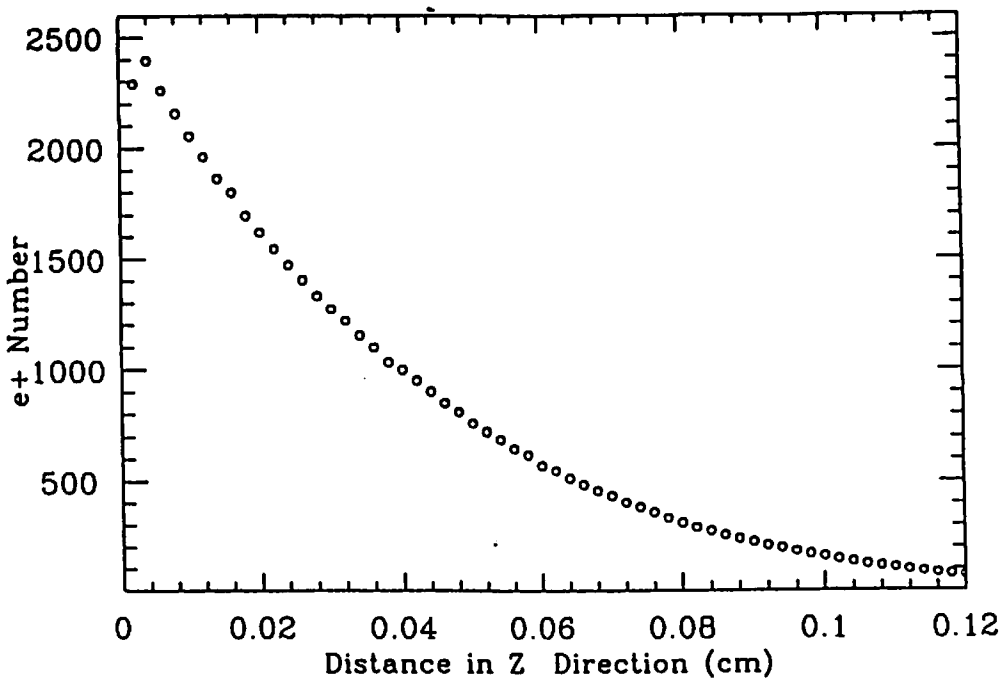

Figure 7 Stopped-positron distributions along the Z-direction for positrons emitted from ^{22}Na. The calculation was performed with point beams.

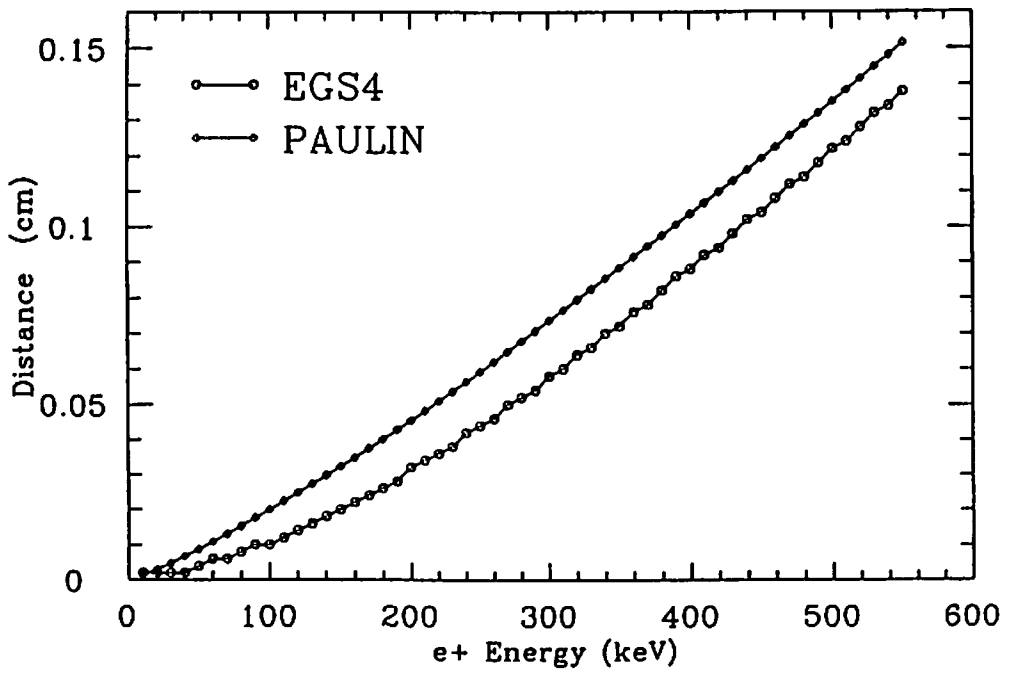

Figure 8 Penetration length vs. energy: EGS4 calculation (○) and Paulin's empirical equation of mass-attenuation coefficient (◇). The calculation was performed with point beams.

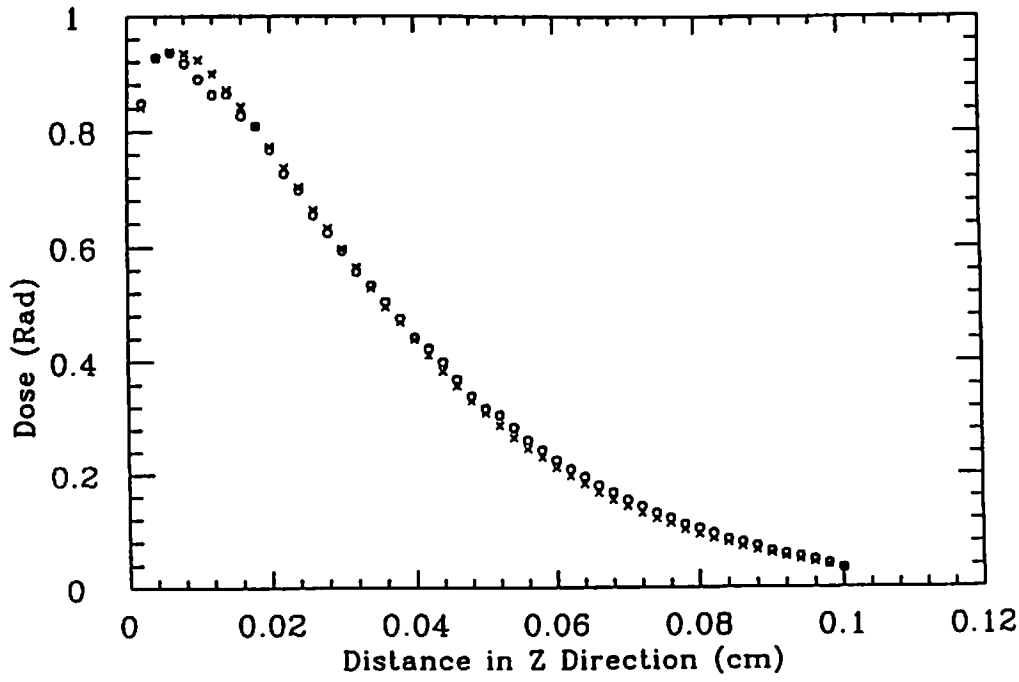

Figure 9 Dose distributions along the Z-direction from n=1 to 50 for m=1 (○) and for m=5 (×). The calculation was performed with a surface source of 1 mmϕ.

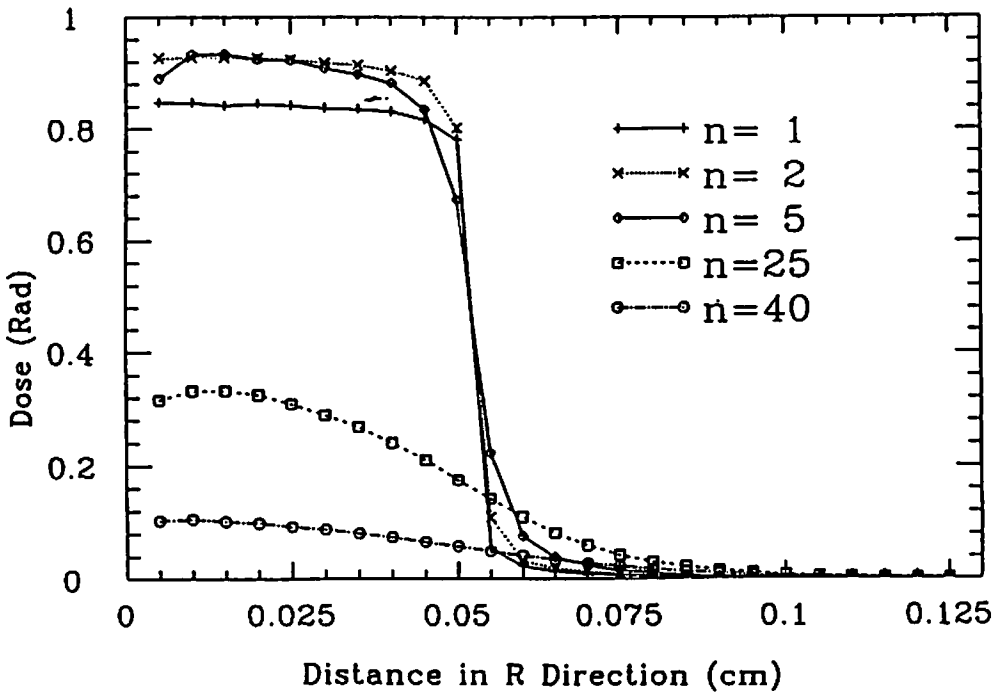

Figure 10 Dose distributions along the R-direction from m=1 to 25 for n=1 (+), n=2 (×), n=5 (◇), n=25 (□), and n=40 (○). The calculation was performed with a surface source of 1 mmϕ.